HIGH TEMPERATURE ALTERATION CONDITIONS WITHIN LAVA TUBES: AN ANALOGUE FOR VENUS SURFACE GEOLOGY

by

Dylan Alexander Childs

A Thesis Submitted in

Partial Fulfillment of the

Requirements for the Degree of

Master of Science

in Geosciences

at

The University of Wisconsin-Milwaukee

August 2024

ABSTRACT

HIGH TEMPERATURE ALTERATION CONDITIONS WITHIN LAVA TUBES: AN ANALOGUE FOR VENUS SURFACE GEOLOGY

by

Dylan Alexander Childs

The University of Wisconsin-Milwaukee, 2024
Under the Supervision of Professor Lindsay J McHenry

Scientific exploration of other planetary bodies comes with many limitations, and Venus is no exception. Average surface temperatures of ~460°C and an atmospheric pressure of ~96 bars has severely limited the longevity of any instruments sent to the surface of Venus. Furthermore, with an atmosphere composed of ~96.5% CO_2, there are only three wavelength windows in the near infrared region that can be used to measure the mineralogical composition of the surface. Due to these constraints, our understanding of Venus' surface mineralogy is severely limited and to date direct measurements of its geologic composition are limited to a handful of XRF measurements from short-lived Soviet-era landers. A better understanding of the surface mineralogy helps us to better constrain the primary composition, the climate history, and the geochemical reactions between the surface and atmosphere. Laboratory experiments and modeling have helped interpret spectroscopic readings of the planet's surface. Experiments and models indicate that surface-atmosphere interactions under Venus conditions alter basaltic rock surfaces to produce secondary minerals, predominantly anhydrous sulfates and iron oxides, which may affect spectroscopic readings. This study demonstrates that using lava tubes as an analogue for the surface geology of Venus may also prove informative. Lava tubes are geologic landforms that provide high-temperature, insulated environments as they cool, and are observed to contain minerals predicted to form on the surface of Venus. Tholeiitic basalt samples were collected from the interiors of lava tubes on the Big Island of Hawai'i. X-ray diffraction (XRD) patterns reveal the mineral assemblages of the substrates and lava tube interiors. Primary minerals present in the substrate samples include augite, anorthite, ilmenite, and titanomagnetite. SEM imagery and VNIR spectroscopy of surface veneers indicate that magnesioferrite, hematite, diopside, cristobalite, and tridymite are secondary minerals produced through cation migration in a dry, high-temperature environment. While there are significant differences in temperature and atmospheric composition between lava tubes and Venus, these results are still similar to weathering experiments conducted in Venus simulated environments. Further investigation of lava tubes can better constrain the differences in weathering intensity, as well as teach us more about how lava behaves in a slow-cooling environment.

TABLE OF CONTENTS

LIST OF FIGURES

LIST OF TABLES

LIST OF ABBREVIATIONS

XRF	X-Ray fluorescence
USSR	Union of Soviet Socialist Republics
NIR	Near Infrared
Ma	Million years ago
SEM	Scanning Electron Microscopy
VNIR	Visible-Near Infrared
KK	Kipuka Kanohina
ML	Upper Mauna Loa
PU	Puʻuʻōʻō
ESRI	Environmental Systems Research Institute
CGIAR	Consultative Group for International Agricultural Research
USGS	United States Geological Survey
DOFAW	Division of Forestry and Wildlife
NARS	National Area Reserves System
XRD	X-Ray Diffraction
BSE	Back Scatter Electron
PDBSE	Photodiode Backscatter Electron Detector
EDS	Energy Dispersive X-ray Spectrometer
SE	Secondary Electrons
An	Anorthite
Au	Augite
Il	Ilmenite
Ti	Titanomagnetite
Hm	Hematite
Mg	Magnesioferrite
Cr	Cristobalite
Tr	Tridymite
UV	Ultraviolet
SWIR	Shortwave Infrared
TIR	Thermal Infrared
PDS	Planetary Data System
JPL	Jet Propulsion Laboratory

ACKNOWLEDGEMENTS

I'd like to start off by noting that this is a non-exhaustive list, and there are many people to which I owe a token of gratitude to including the many friends, family, and colleagues that supported me throughout graduate school. I'd like to first acknowledge my advisor, Dr. Lindsay J McHenry. Without Lindsay, the conception, design, and support for this project would have never been founded. I would like to thank all the amazing, hospitable people that provided us with support sampling lava tubes on the Big Island of Hawai'i including Rick Hazlett, Peter Bosted, Ann Bosted, Cheryl Gansecki. Thank you to Jorge Acosta and Adam Chumley for their assistance with sample collection. Thank you to the Professors at UW- Milwaukee that helped with laboratory work, including Dr. Heather Owen and Dr. William Musinski. A special thank you to Dr. Gayantha Kodikara for his extensive help with the measurement and interpretation of the spectroscopic data. Finally, I would like to thank the Wisconsin Space Grant Consortium for providing the funding to pursue this research project.

Introduction

Research of the surface geology of Venus through remote sensing and in-situ analysis is limited by obstructing atmospheric conditions and temperature. Venus' atmosphere is composed of ~96.5% CO_2 (carbon dioxide) with trace amounts of SO_2 (sulfur dioxide) and other gas species (Zolotov, 2018). The average atmospheric pressure and temperature is ~95.6 bars and 467°C (Seiff et al., 1985; Zolotov, 2018). In addition to inhospitable conditions for scientific instruments, a general lack of exploration means that much is still unknown about the planet. Compositional knowledge of Venus' surface geology is largely limited to three XRF (X-Ray fluorescence) analyses and several gamma-ray spectroscopy measurements taken in the 1970s and 80s by USSR landers (e.g.- Barsukov et al., 1982, 1986; Surkov et al., 1976, 1986; Dyar et al., 2021). The dense CO_2 atmosphere limits orbital remote spectroscopy to observations in only a few NIR (Near infrared) windows (1.02, 1.10, and 1.18 μm) (Gilmore et al., 2017). Venus Express (2006-2014) measured Venus' surface emissivity at 1.02 μm, which is a characteristic wavelength for assessing ferrous iron content. High emissivity measured at 1.02 μm indicates higher ferrous iron content, and a lower emissivity indicates a lower abundance of ferrous (or more oxidized) iron (Gilmore et al., 2017).

Both in-situ data and orbital spectroscopy suggest that the surface geology is composed of sub-alkaline basalts. Regions of Venus with higher emissivity are interpreted to be younger, unweathered basaltic flows (Smrekar et al., 2010), whereas regions of lower emissivity could indicate two options: a weathered and therefore more oxidized basalt surface, or a more silicic composition (Gilmore et al., 2017). However, more recent studies suggest emissivity is not strongly affected by the alteration and formation of secondary minerals (Gilmore et al., 2023;

Dyar et al., 2021). Gamma ray spectroscopy of some regions with lower emissivity, like some of the tesserae, suggests that compositions like rhyolite or granite are present on the surface (Vinogradov et al., 1973; Dyar et al., 2021). Verifying these results could have large implications for our understanding of past water and tectonic activity of the planet, two important factors for past habitability (Foley, 2015).

In addition to identifying bulk rock composition, mineral characterization through spectroscopy may also provide necessary information to determine relative ages of rock units. For many other planetary bodies, scientists use the density of impact craters to study relative and absolute surface ages. For two main reasons, this method is not applicable or at least very limited for Venus. First, the thick atmosphere "filters" most impactors that enter it, hypothetically eliminating as much as 98% of craters 35km in diameter or smaller (Schaber et al., 1992). Secondly, a putative global resurfacing event that occurred ~500 Ma means that much of the current surface of Venus might only contains impact craters that have been produced since then. In effect this means that there are fewer than a thousand impact craters across the entire surface of Venus (Kreslasky et al., 2015). Studying mineral alteration and weathering rates may provide better insight to relative ages and current geologic processes. Laboratory experiments weathering basalts under Venus-like conditions reveal that secondary minerals such as iron oxides and sulfates form over the surface on a timescale of weeks to months (e.g. Filiberto et al., 2020; Cutler et al., 2020; Santos et al., 2023). Therefore, the presence of unweathered basalt would indicate recent or even currently active volcanism on Venus. Indeed, Magellan radar images provide evidence of ongoing volcanic activity on the surface of Venus that resembles hot-spot volcanism (Herrick and Hensley, 2023).

This research project aims to better constrain how surface weathering under Venus-like conditions can alter a rock's composition and its reflectance. Terrestrial basaltic lavas cool more quickly and in contact with cooler atmospheric conditions than lavas on Venus, and these differences in hot lava-air interactions lead to different patterns in surface alteration. Basaltic lava tubes on Earth provide a potential analogue for Venus surface weathering, since their interiors provide an insulated, hot environment for months to years following their formation. Basaltic rock samples were collected from the interior of Hawaiian lava tube systems as a potential analogue for Venus surface geology. These volcanically formed caves hosted a high-temperature alteration environment that may have been similar to that on the surface of Venus. Prior research by Ruffini (2011) reveals that surfaces of some lava tubes exhibit a metallic veneer, and further SEM (Scanning Electron Microscopy) analysis shows evidence for cation migration, which is indicative of a high temperature oxidation environment (Minitti et al., 2005). This research further examines the origin of these features.

The objective of this project is to investigate the alteration conditions of lava tubes by studying the secondary minerals on the surfaces of lava tube interiors and reconstructing the mechanisms that formed them. These alteration mechanisms and the resulting mineralogy are compared to those inferred for the surface of Venus based on past experimental and remote sensing studies. This is accomplished by characterizing the mineralogy and bulk elemental distribution of sample exteriors and interiors, analyzing spectral signatures using VNIR (Visible-Near Infrared) spectroscopy, and SEM analysis of sample cross-sections and surfaces.

Background

Lava Tubes

Lava tubes, also referred to as volcanic caves or pyroducts, are of particular interest because of their distinct minerogenic environment. These landforms are commonly formed through effusive lava flows. There are two main modes of lava tube formation, termed "inflationary" and "crusting-over" (Sawlowicz, 2020, and references therein). Both mechanisms involve the upper layer of lava solidifying due to exposure to the cooler air, which insulates the still flowing interior. Thermal erosion and changing pulses in lava flows permit superheated gas to fill the upper voids of the tubes (figure 1). These conditions provide for a well-insulated environment. Research has shown that flows through lava tubes only decrease in temperature by ~0.5-1°C/km (Helz et al., 2003; Thornber, 2001). During the active stage, the surfaces of walls and ceilings have fluctuating temperatures near and above the basalt solidus (~900-1080°C; Helz et al., 2003; Witter and Harris, 2007). Temperatures within lava tubes also remain elevated for extended periods, ranging from months to years after the last flow event (e.g. Porter, 2000).

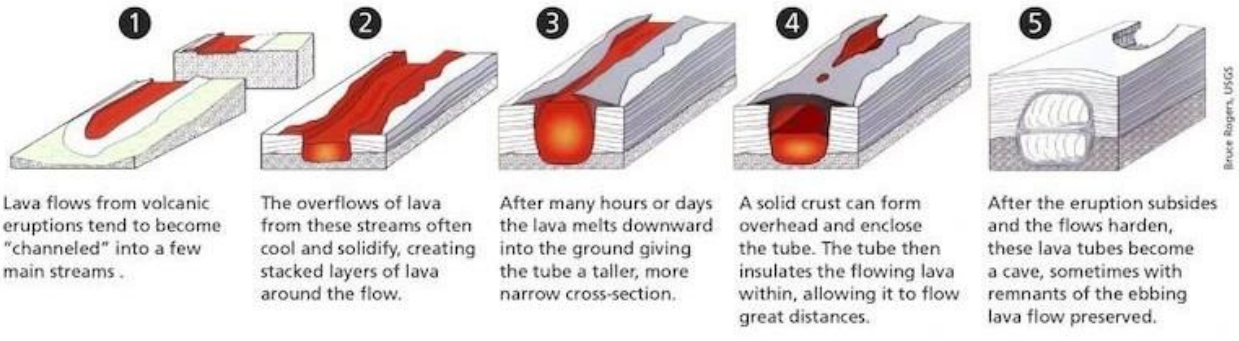

Figure 1 Graphic and description of the five principal steps for typical lava tube formation. Image is a part of the public domain and was designed by Bruce Rogers of the USGS.

The dynamic environment of lava tubes creates varying mineral forming conditions as the lava tube transitions from peak temperatures during its active stage to a transitional cooling stage and then finally reaching ambient temperatures at equilibrium with the environment. While lava tubes are active or in their cooling stages and temperatures exceed 100°C, the dominant mineral forming mechanisms include sublimation and precipitation (Sawlowicz, 2020). Observations of secondary minerals forming in this environment include native sulfur, sulfates, oxides, and hydroxides (Sawlowicz, 2020; Forti, 2005). These include minerals that are predicted to form on the surface of Venus, including magnetite, hematite, and anhydrite (Santos et al., 2023). After temperatures cool below 100°C, meteoric water begins to infiltrate. Cooler temperatures and the addition of liquid water create new mechanisms for mineral formation, including more typical karst processes and biogenic activities. This would form hydrous sulfates, oxides, hydroxides, phosphates, nitrates, and halides (Forti, 2005). The introduction of meteoric water also removes the more soluble sulfates that formed at higher temperatures. The speed of this process depends on climate. Areas with more rainfall will remove the soluble sulfates at a dramatic rate, with a complete removal within a span of weeks to months (Porter, 2000; Guimbretière et al., 2014). The more soluble sulfates survive longer in drier and more elevated regions (White, 2010).

Hawai'i

In November 2022, we traveled to the Big Island of Hawai'i. The Big Island is comprised of five major volcanoes. We sampled from Mauna Loa and Kilauea, which are the

two southeasternmost volcanoes of the Big Island. These shield volcanoes are the most active of the island, as they are the youngest and still in their shield building stage (Eaton and Murata, 1960). Hawaiian volcanoes are produced through hot spot volcanism, and during the shield building stage these volcanoes erupt tholeiitic basalts (Eaton and Murata, 1960; Yang et al., 2023). The activity and style of eruption of these volcanoes make lava tubes a common landform along their slopes.

From these volcanoes, we sampled from several lava tube systems (Figure 2). The three main systems studied (Figure 3) are Kipuka Kanohina (KK), Upper Mauna Loa (ML), and Pu‘u‘ō‘ō (PU). The Kipuka Kanohina and Upper Mauna Loa lava tube systems are sourced from the Mauna Loa Volcano. Kipuka Kanohina formed ~800 years ago off the southwest rift zone and the part of the upper Mauna Loa system sampled formed ~180 years ago during the lava flow

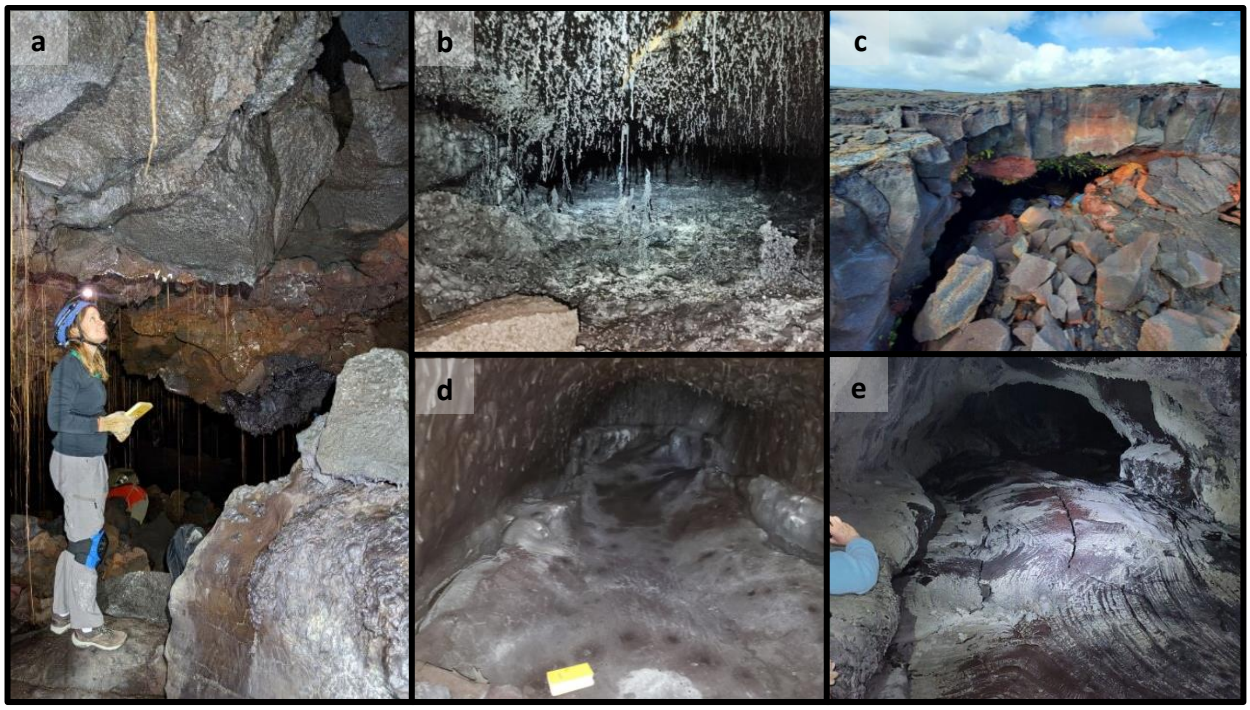

Figure 2 photographs of different lava tubes. **(a)** image taken in Black Ball Cave, KK flow, **(b)** image of an interior section of Ana Polu Cave, PU flow, **(c)** entrance of Ana Polu Cave, **(d)** image within the KK flow, **(e)** and an image within Crystal Cave, ML flow

of 1843 (Lockwood and Lipman, 1987; personal communications). The sampled Pu‘u‘ō‘ō lava tube system formed towards the end of the thirty-year eruption of the Pu‘u‘ō‘ō crater cinder-and-spatter cone in 2016-2018 and is sourced from Kilauea Volcano (Heliker and Mattox, 2003; Neal et al., 2019).

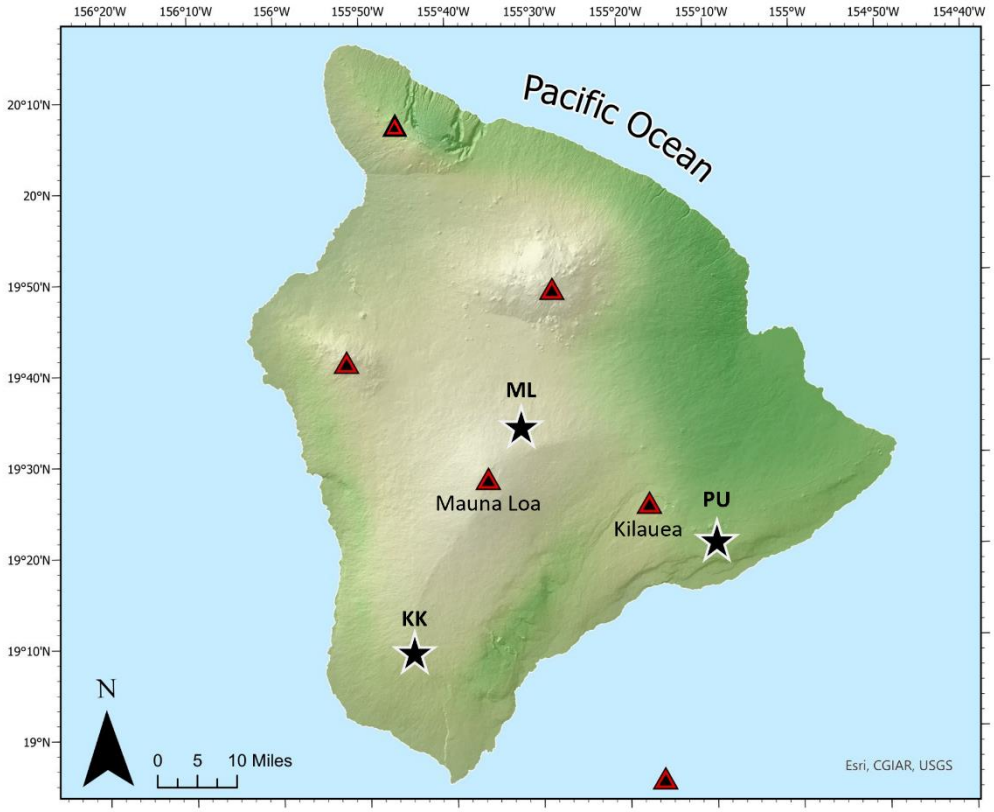

Figure 3 Map of the Big Island of Hawai’i. Red triangles represent the approximate locations of each respective volcano. The black stars indicate the general area where samples were collected. KK stands for the Kipuka Kanohina cave system, ML stands for the Upper Mauna Loa cave system, and PU stands for the Pu‘u‘ō‘ō cave system. Map data and features collected from ESRI, CGIAR, USGS.

Methods

When collecting samples in the lava tubes, great care was used to minimize any damage. Samples collected were chosen from fallen ceiling and wall fragments. Targeted samples exhibited a smooth, metallic luster veneer coating the outer surface. Several samples

additionally contained yellow and white secondary deposits. Two “substrate” samples were collected from outside the Kipuka Kanohina and Puʻuʻōʻō lava tube systems. These samples are assumed to be from the same flow that formed each respective tube, but cooled more quickly at the surface compared to in an insulated cave environment. Table 1 provides physical descriptions for each of the samples collected and measured.

Sample ID	Basalt Sample Description
KK-21-08	Gray, metallic lustered veneer
KK-21-10	Substrate sample
KK-22-01	Dark gray, metallic lustered veneer
KK-22-02	Brown-grey veneer coated with white and yellow powder
KK-22-04	Metallic lustered vesicles, no surface veneer
KK-22-05	Dull red veneer and interior
KK-22-06	Dull red-brown veneer and interior
KK-22-07	Dark gray, metallic lustered veneer
KK-22-08	Brown-grey metallic veneer
KK-22-09	Brown-grey metallic veneer
KK-22-10	Dull red-brown surface
KK-22-11	Gray, metallic lustered veneer
ML-13-01	Gray veneer, white powder on surface
ML-13-02	Gray, metallic lustered veneer
ML-13-03	Dull red-brown veneer, gray interior
ML-13-04	Dull red veneer and interior
PU-22-02	Gray, metallic lustered veneer
PU-22-04	lavacicle with gray metallic veneer
PU-22-05	Gray, metallic lustered veneer
PU-22-06	Substrate sample
PU-22-07	Gray, metallic lustered veneer with white powder coating
PU-23-01	Gray, metallic lustered veneer

Table 1 A list of each sample that was studied for further analysis. Substrate samples are described as such in the sample description, all other samples are altered basalt samples collected from the lava tube interiors. KK= Kipuka Kanohina; ML= Mauna Loa; and PU= Puʻuʻōʻō.

The Kipuka Kanohina lava tube system consists of a variety of separate cave bodies that comprise the original flow. In total we sampled from five caves, including Black Ball Cave and the Topa entrance of the main Kipuka Kanohina Flow. Permission for sampling from these caves was granted by the Cave Conservancy of Hawai'i. Samples were also collected from three unnamed caves on private land, after permission was granted by the landowners. Sampling from Crystal and Sparkle Cave in the 1843 Mauna Loa flow was granted by the DOFAW (Division of Forestry and Wildlife), however the permits did not allow exporting the samples to the mainland. Scanning Electron Microscopy (SEM) data was therefore collected for four samples from the 1843 Mauna Loa flow at the University of Hawai'i- Hilo. For this project, these samples and analyses will be supplemented by new analyses of samples collected from the same caves in 2013 (and exported at that time with full DOFAW permission). The Pu'u'ō'ō samples were collected from Ana Polu Cave, located in a remote patch of lava flows (the 61g flow, active 2016-2018) on the eastern flank of Kilauea. To sample from Ana Polu Cave, we acquired permission from the NARS (National Area Reserves System). This permit allowed us to access the site via helicopter and collect samples. All samples collected from Kipuka Kanohina and Pu'u'ō'ō were bagged and brought back to the University of Wisconsin- Milwaukee for further laboratory analysis.

Three different types of samples were prepared for analysis (figure 4). The first is the substrate samples. The second includes the surface veneers of each lava tube sample. Surface samples were collected by skimming the veneer off using a rotary tool with a tungsten carbide bur attachment. The third type of sample includes the "interior" of the lava tube samples, which are subsamples of the same sample from the lava tube beneath the veneer. Interior samples were separated and collected using a rock saw. The surface veneer and interior samples of the lava tubes were prepared in the department's mineralogy laboratory.

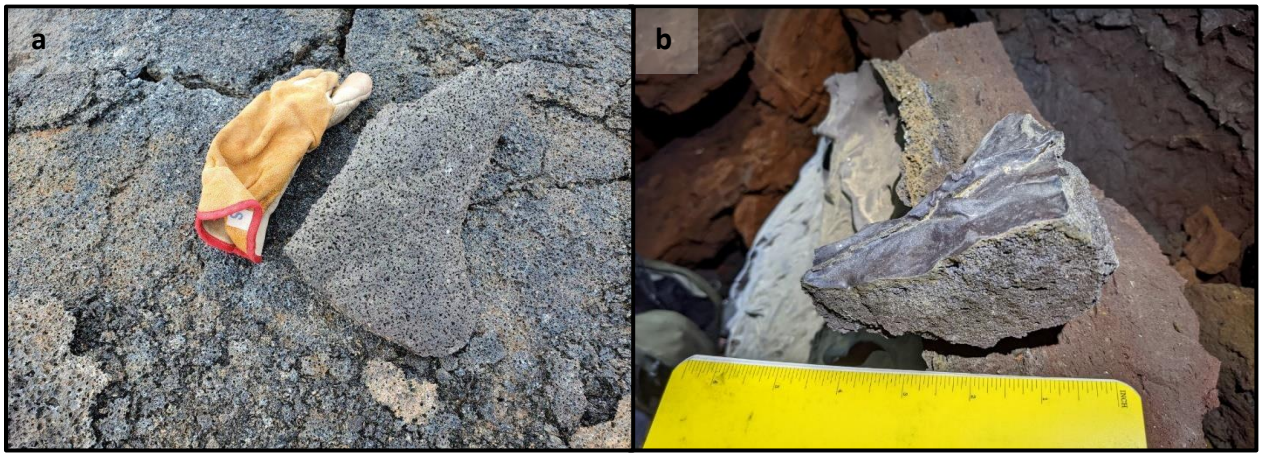

Figure 4 Field photos of representative samples collected. **(a)** photograph of the Puʻuʻōʻō substrate sample (PU_22_06), glove for scale. **(b)** photograph of lava tube sample KK_22_01. Note the smooth metallic veneer on the surface of the rock versus the vesicular interior.

XRD (X-Ray Diffraction) analysis was conducted to determine the mineral assemblages of sample surfaces and interiors. Surface, interior, and substrate samples were powdered using a mortar and pestle to achieve a fine enough grain size for the X-ray diffractometer. Each powdered sample was mounted as a random powder and analyzed using a Bruker D2 Phaser X-Ray Diffractometer (3-60° 2-Theta, .01s/step, Cu tube (1.54184 Å) with 30kV, 10mA, LYNXEYE_XE_T (1D) detector). The patterns were interpreted using Bruker's EVA software and minerals were identified by comparison against the ICDD PDF-2 database. In addition, 1-2cm

cuts of sample surfaces were sent to University of Colorado- Boulder for VNIR (Visible-Near Infrared) spectroscopy. Spectral signatures of samples were evaluated for absorption features characteristic of ferric iron and water content.

SEM was used to analyze elemental distributions and mineralogical patterns on cross-sections of sample surfaces. In total seventeen samples were prepared, but two broke during the polishing step. Four samples were prepared and analyzed at the University of Hawai'i- Hilo, with assistance from Professor Cheryl Gansecki. Four of the Mauna Loa samples for which we had permits to collect but not remove from the island were selected for sample analysis (ML_22_01, 02, 03 and 04). Samples were prepared by cutting small, 1-2cm, cross-sections containing the surface veneer and interior of the rock. Each cross-section was placed in a sample holder and filled with Buehler Epoxicure 2 resin and hardener solution. Samples were placed in an oven overnight at 80°C to cure. Once dry, the epoxy coated samples were removed from their holders for polishing. Samples were hand polished with 240, 320, and then 600 grit paper. After hand polishing, samples were ready to be mounted onto an Autopolishing head which continued to polish the samples with a 15 µm, 6 µm, and 3 µm polishing pad. Once polished, samples were carbon coated and placed in the SEM. The Aztec software program was used for element mapping.

Eleven samples were prepared and analyzed using SEM at the University of Wisconsin-Milwaukee; six samples from the Kipuka Kanohina flow and five samples from the Pu'u'ō'ō flow. Samples were prepared for SEM analysis by cutting ~2.54x1.27 cm cross-sections of samples that feature both the veneer and interior of the rock. Cuts were placed in a LECO PR-25 Mounting Press with one-half scoop of mounting press powder and one-half scoop of

conductive powder. The sample and powder were set to 3700 PSI and high heat for 5 minutes to form a hot epoxy mold. Each sample was polished using five different grit sizes. Polishing started at a coarse grit and then sequentially progressed to a finer grit size. The starting grit was 120 and then progressed to 240, 320, 400, and finally a 600-grit size. Sample KK_22_11 was carbon coated for reduced charging and further analysis.

Polished samples were set in a 1-1/4" metallographic mount holder and analyzed with a Hitachi S-4800 SEM. Images were taken in BSE (back scatter electron) mode using the PDBSE (photodiode backscatter electron detector). A Bruker EDS (Energy Dispersive X-ray spectrometer) was used to measure elemental distributions across the sample cross sections and generate element maps. The carbon coated sample was also imaged in SE (secondary electron) mode for enhanced topographic images.

VNIR spectroscopy data were collected at University of Colorado- Boulder. Small chips of twelve sample veneers (four from Pu‘u‘ō‘ō and eight from Kipuka Kanohina) featuring relatively flat surfaces were removed via rock saw and sent to the lab. Spectral signatures were collected with a TerracSpec Halo from Analytical Spectral Devices. The TerraSpec Halo was placed directly over sample surfaces to minimize interference on spectra measurements. For each sample, three spectra were measured across wavelengths between 350-2500nm and the averages were recorded.

Results

X-ray Diffraction

The complete mineral assemblage of each sample is listed in the tables below (2a and 2b). The tables provide a qualitative analysis of the data collected from the XRD plots. Figure 5 (a, b, and c) show representative patterns of the mineral assemblages for the substrate, lava tube exterior, and lava tube interior samples respectively. Additional XRD patterns are provided in Appendix A. The XRD patterns of the substrate samples are dominated by two primary minerals: anorthite and augite. The substrates also contain some ilmenite. The concentration of ilmenite varies between flows, with ilmenite being relatively abundant in the Puʻuʻōʻō flow but nearly absent in the Kipuka Kanohina flow. In addition, the Puʻuʻōʻō substrate also contains titanomagnetite and trace amounts of hematite. Secondary minerals found in the lava tube samples include hematite, magnesioferrite, cristobalite, tridymite, and gypsum.

Secondary minerals are present in both the sample veneers and their interiors, apart from gypsum, which is only found on the surfaces of some lava tube samples. Differences in peak intensities suggest the concentrations of minerals differ between the surface and interior. In general, the concentrations of magnesioferrite and hematite are highest at the surface and lower within the interior. The primary minerals (anorthite, augite, and ilmenite) and the silica minerals (cristobalite and tridymite) appear in lower concentrations at the surface and in higher concentrations within the interior.

	Anorthite	Augite	Ilmenite	Hematite	Magnesioferrite	Cristobalite	Tridymite	Gypsum
Kipuka Kanohina								
Substrate	XX	XX	+	-	-	-	-	-
Sample Veneer								
KK_21_08	XX	XX	-	X	XX	X	-	-
KK_22_01	XX	X	-	+	X	X	-	-
KK_22_02	XX	XX	+	X	XX	+	+	-
KK_22_05	XX	XX	-	XX	XX	XX	-	-
KK_22_06	XX	XX	-	X	XX	XX	-	+
KK_22_07	XX	XX	-	X	XX	XX	-	-
KK_22_08	XX	XX	-	X	XX	X	-	-
KK_22_09	XX	XX	-	+	X	+	-	-
KK_22_10	XX	XX	-	X	XX	X	-	-
KK_22_11	XX	XX	-	X	XX	X	-	-
Sample Interior								
KK_21_08	XX	XX	+	-	-	-	-	-
KK_22_01	XX	XX	-	X	X	+	-	-
KK_22_02	XX	XX	X	-	X	-	+	-
KK_22_05	XX	XX	-	XX	XX	XX	-	-
KK_22_06	XX	XX	-	X	XX	X	-	-
KK_22_07	XX	XX	-	XX	XX	XX	-	-
KK_22_08	XX	X	-	+	X	XX	-	-
KK_22_09	XX	X	-	+	X	XX	-	-
KK_22_10	XX	XX	-	+	XX	X	-	-
KK_22_11	XX	XX	-	XX	XX	XX	-	-
Mauna Loa								
Sample Veneer								
ML_13_01	XX	XX	-	XX	XX	+	-	-
ML_13_02	XX	XX	-	XX	XX	X	-	+
ML_13_03	XX	XX	-	+	X	-	-	-
ML_13_04	XX	XX	+	XX	XX	X	-	+
Sample Interior								
ML_13_01	XX	XX	-	XX	XX	X	-	-
ML_13_02	XX	XX	-	XX	XX	XX	-	-
ML_13_03	XX	XX	-	+	X	-	-	-

Table 1a Mineral assemblages of the substrate, veneers, and interiors of samples from the Kipuka Kanohina and Mauna Loa lava tube systems. In orange are the primary minerals; blue are secondary. Frequency symbols: XX = greatest abundance; X = present, but in lower amounts; + = rare; - = absent.

	Anorthite	Augite	Ilmenite	Titanomagnetite	Hematite	Magnesioferrite	Cristobalite	Tridymite	Gypsum
				Puʻuʻōʻō					
Substrate	XX	XX	X	X	+	-	-	-	-
Sample Veneer									
PU_22_02	XX	XX	X	X	X	XX	X	+	-
PU_22_05	XX	XX	X	X	X	XX	X	+	-
PU_22_07	XX	XX	-	-	XX	XX	X	-	XX
PU_23_01	XX	XX	X	+	X	XX	X	+	-
Sample Interior									
PU_22_02	XX	XX	X	X	+	XX	XX	+	-
PU_22_04	XX	XX	X	X	+	XX	X	+	-
PU_22_05	XX	XX	X	+	-	X	+	+	-
PU_22_07	XX	XX	X	-	-	X	XX	+	-
PU_23_01	XX	XX	X	X	+	X	XX	+	-

Table 1b Mineral assemblages of the substrate, veneers, and interiors of samples from the Puʻuʻōʻō lava tube systems. In orange are the primary minerals; blue is secondary. Frequency symbols: XX = greatest abundance; X = present, but in lower amounts; + = rare; - = absent.

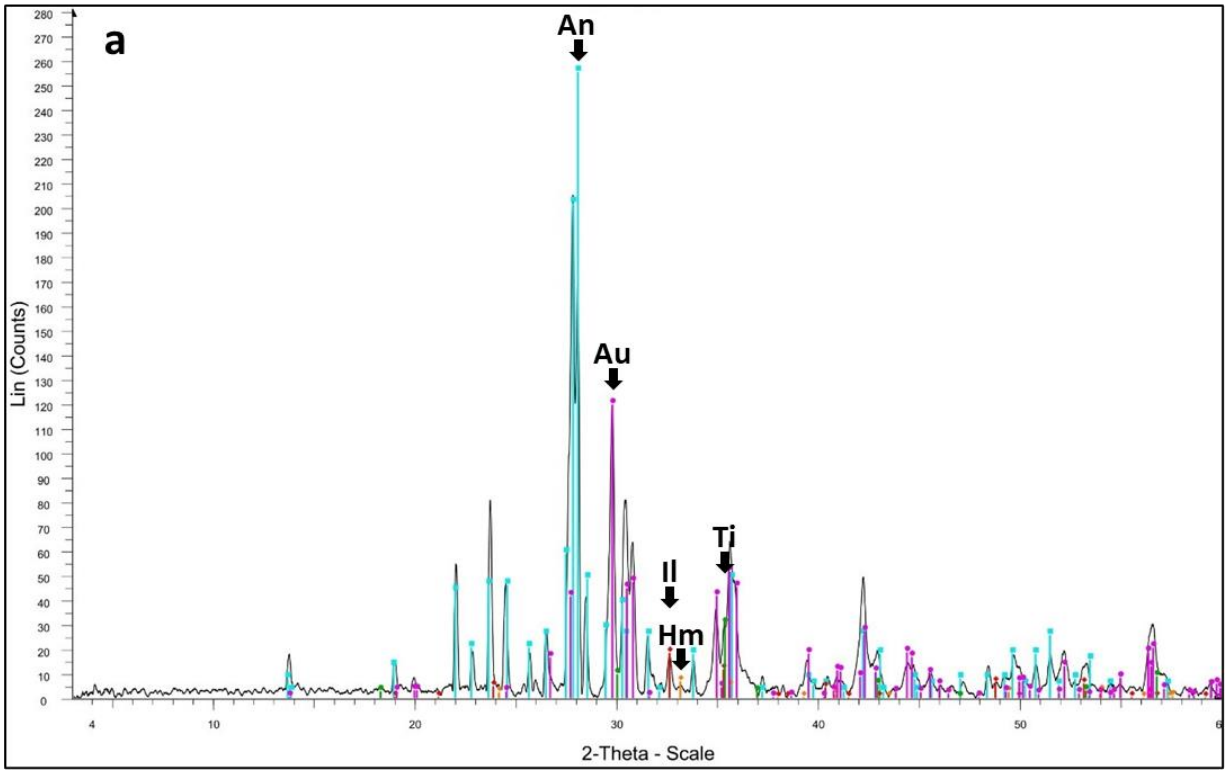

Figure 5 (a) XRD pattern for the substrate sample of Puʻuʻōʻō (PU_22_06). Cyan peaks represent anorthite (An), magenta peaks represent augite (Au), red peaks represent ilmenite (Il), dark green represents titanomagnetite, and orange peaks are hematite.

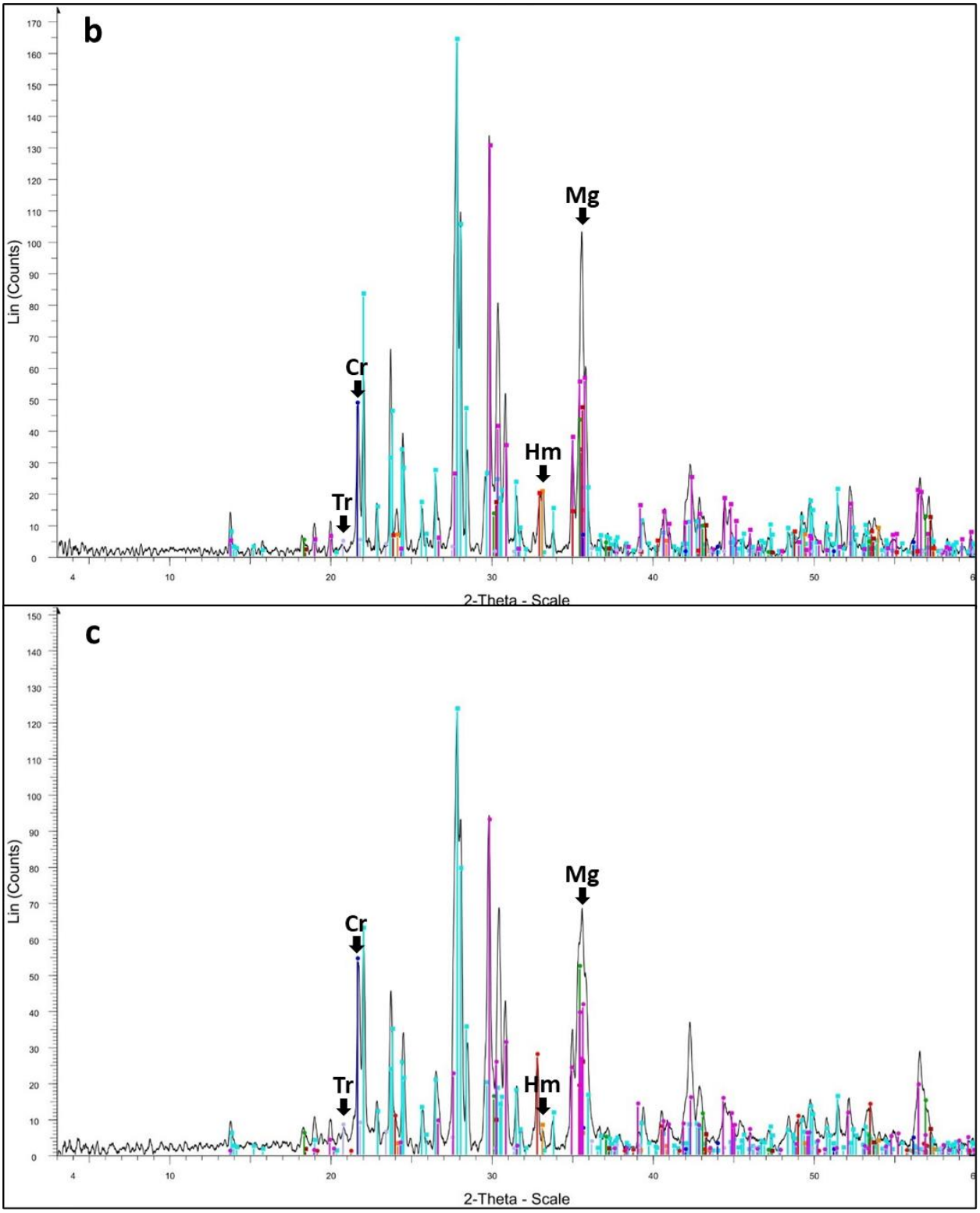

Figure 5 (b) XRD pattern for the veneer of sample PU_23_01. **(c)** XRD pattern for the interior of sample PU_23_01. Cyan peaks = anorthite, magenta = augite, red peaks = ilmenite, dark green = titanomagnetite, orange peaks = hematite (Hm), brown-red peaks = magnesioferrite (Mg), blue peaks = cristobalite (Cr), and violet peaks = tridymite (Tr).

Visible-Near Infrared Spectroscopy

Twelve sample surfaces were analyzed using VNIR spectroscopy from 400-2500 nm wavelength, and their spectral signatures were obtained. Four of the samples are from Puʻuʻōʻō (PU_22_02, 05, 07, and 11; Figure 6) and eight are from Kipuka Kanohina (KK_21_08, KK_22_01, 02, 06, 07, 08, 09, and 11; Figure 7). These samples all feature a drop-off in reflectance starting around 1200 nm and continuing towards the Ultraviolet (UV) - blue wavelength region, indicative of the presence of Fe-O bonds (Gupta, 2017). Also observed for each sample are absorption features near 900 nm, which indicate the presence of ferric ions. Above the 1200 nm wavelength, patterns vary more widely. Samples KK_22_01, 02, 09, and 11 feature a slight decrease in reflectance towards the SWIR (Shortwave Infrared) region, with a decrease in reflectance of less than 0.01. Sample Pu_22_11 exhibits a larger decrease in reflectance, dropping by about 0.1. Samples KK_21_08, KK_22_06, 07, 08, PU_22_02, 05, and 07 all feature an increase in reflectance after 1200 nm towards the SWIR region.

Sample PU_22_07 exhibits the most spectral features of any sample. It has absorption features around the 1440, 1900, 2200, and 2450 nm wavelengths. Features near the 1400 nm wavelength indicate the presence of water (-OH) bonds. The 2200 nm absorption band can form for different reasons. A wide-shallow absorption is caused by Si-OH bonds, and narrow-deep absorptions are caused by Al-OH bonds (Aines and Rossman, 1984). A large absorption near 2450nm forms from S-O bonds (Cloutis et al., 2008). Samples KK_21_08, KK_22_06, 07, 08, and PU_22_11 contain broad water peaks at 1900 nm. Sample PU_22_11 also contains a broad absorption peak at 2200 nm.

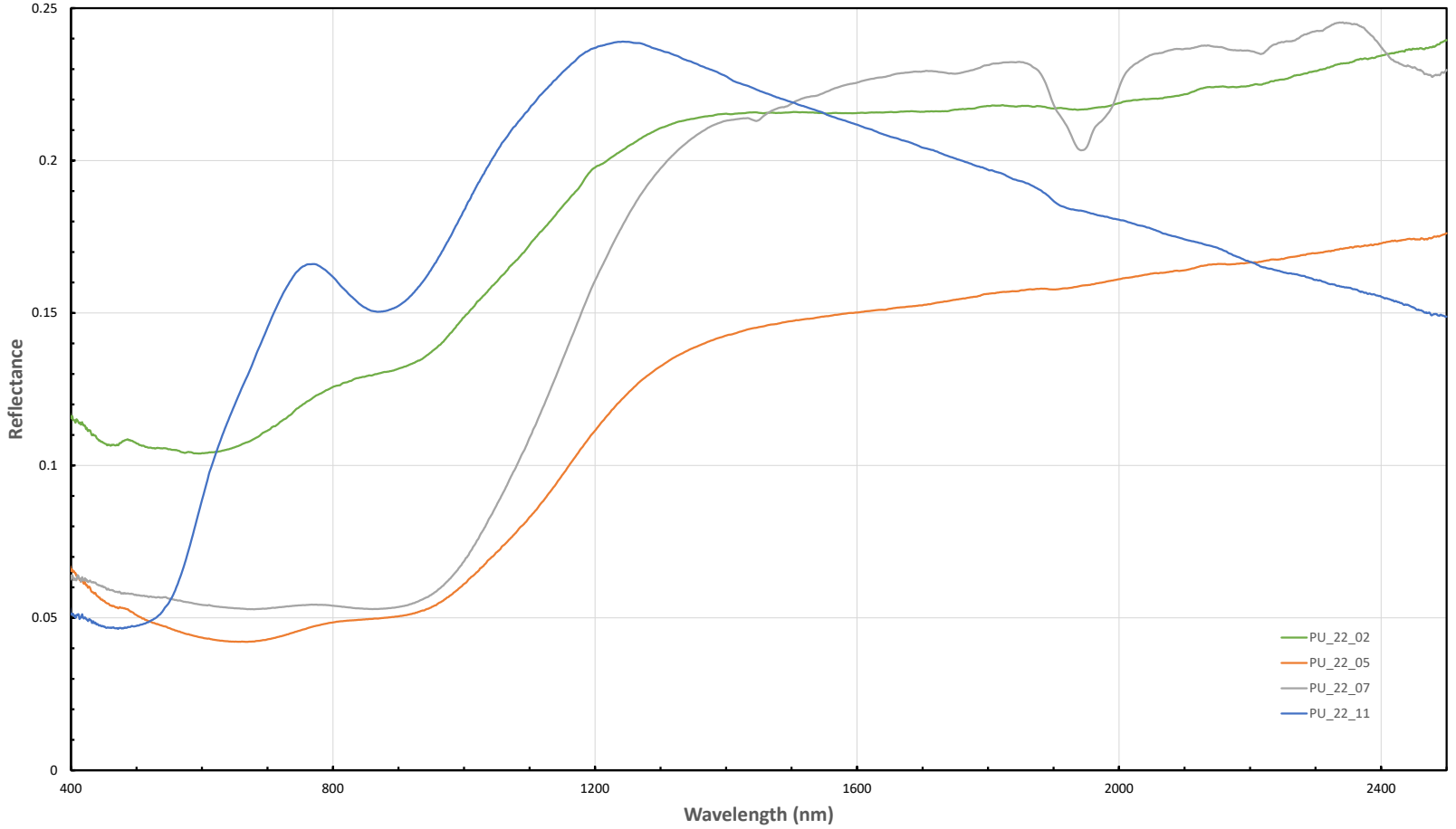

Figure 6 VNIR spectroscopy signatures of the surfaces of samples collected from Puʻuʻōʻō.

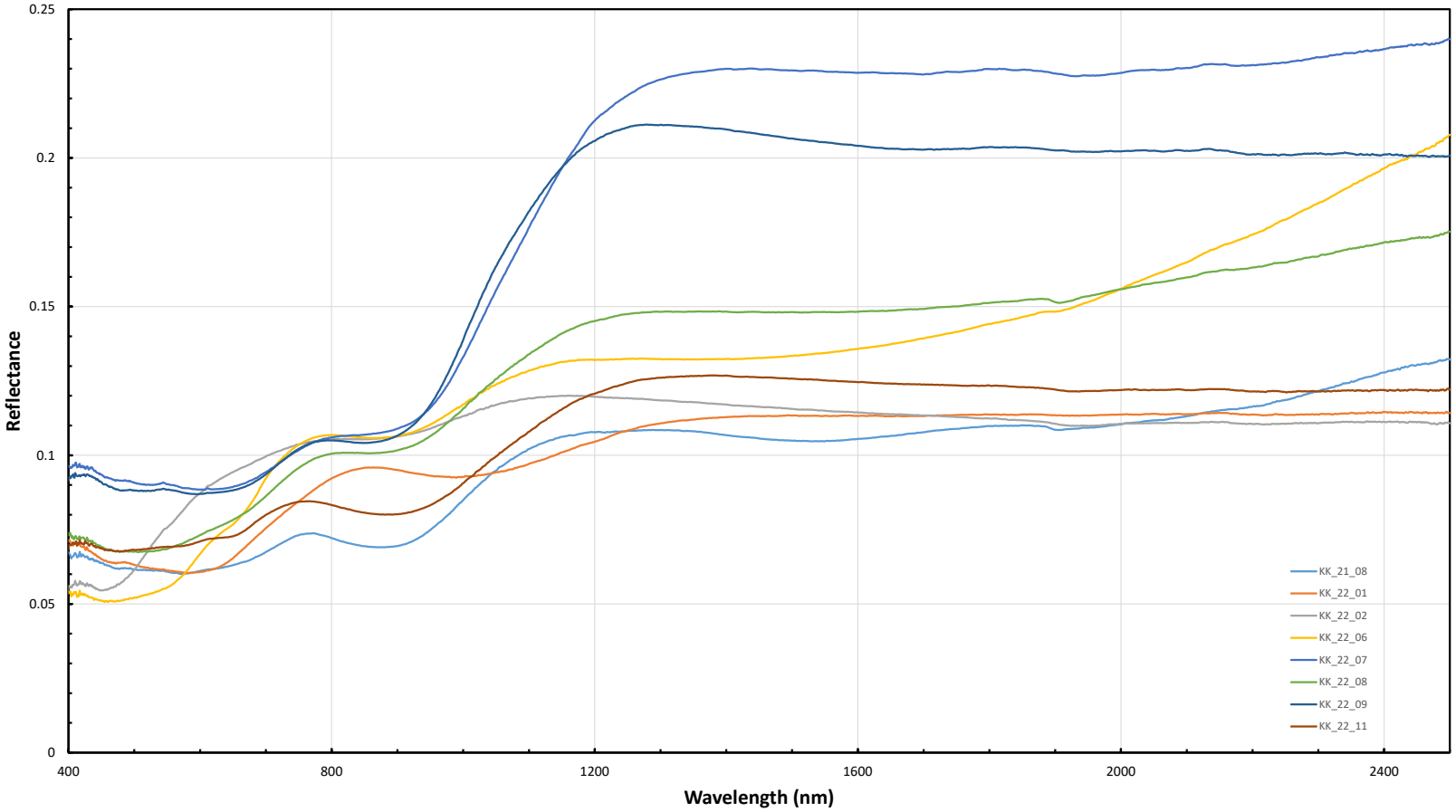

Figure 7 VNIR spectroscopy signatures of the surfaces of samples collected from Kipuka Kanohina.

Scanning Electron Microscopy

Kipuka Kanohina and Pu‘u‘ō‘ō

SEM images reveal geochemical patterns in the surfaces and sub-surfaces of the samples. EDS elemental maps show compositional differences in these areas, revealing the presence of three distinct layers (Figure 8b). This pattern is consistently found in each sample, and more examples are shown in the supplementary images in Appendix B. Layer one, representing the surface veneer, is crystalline and consists of Mg+Fe+O. Notably, not every veneer had a homogenous composition. In some samples, the magnesium is concentrated at the outermost surface of the veneer, so the top portion of the veneer is Mg+Fe+O and the bottom portion is just Fe+O. The second layer is composed of Ca+Mg+Si+O, with a more homogenous element distribution. The third layer is composed of a mixture of different crystals within a basalt glass matrix. Compositions of the crystals in this layer vary, but the most common ones are depicted in figure 5. Layer three is often composed of tabular crystals composed of Ca+Al+Na+Si+O (consistent with plagioclase), subhedral Ti+Fe+O crystals (consistent with an oxide, e.g. ilmenite or titanomagnetite), and subhedral Ca+Mg+Si+O (consistent with diopside). Two unique crystals were also observed, including a Cu+Fe+O crystal within the surface veneer of KK_22_02 and a Ca+P+O (consistent with apatite) crystal in the subsurface of sample PU_22_02 (Appendix B). The amorphous matrix in the subsurface is largely composed of Na+Al+Si+O.

BSE imagery also revealed trends in the interior of samples. A pattern found only in the Pu‘u‘ō‘ō samples is long, linear arrangements of Ti+Fe+O crystals (likely ilmenite or

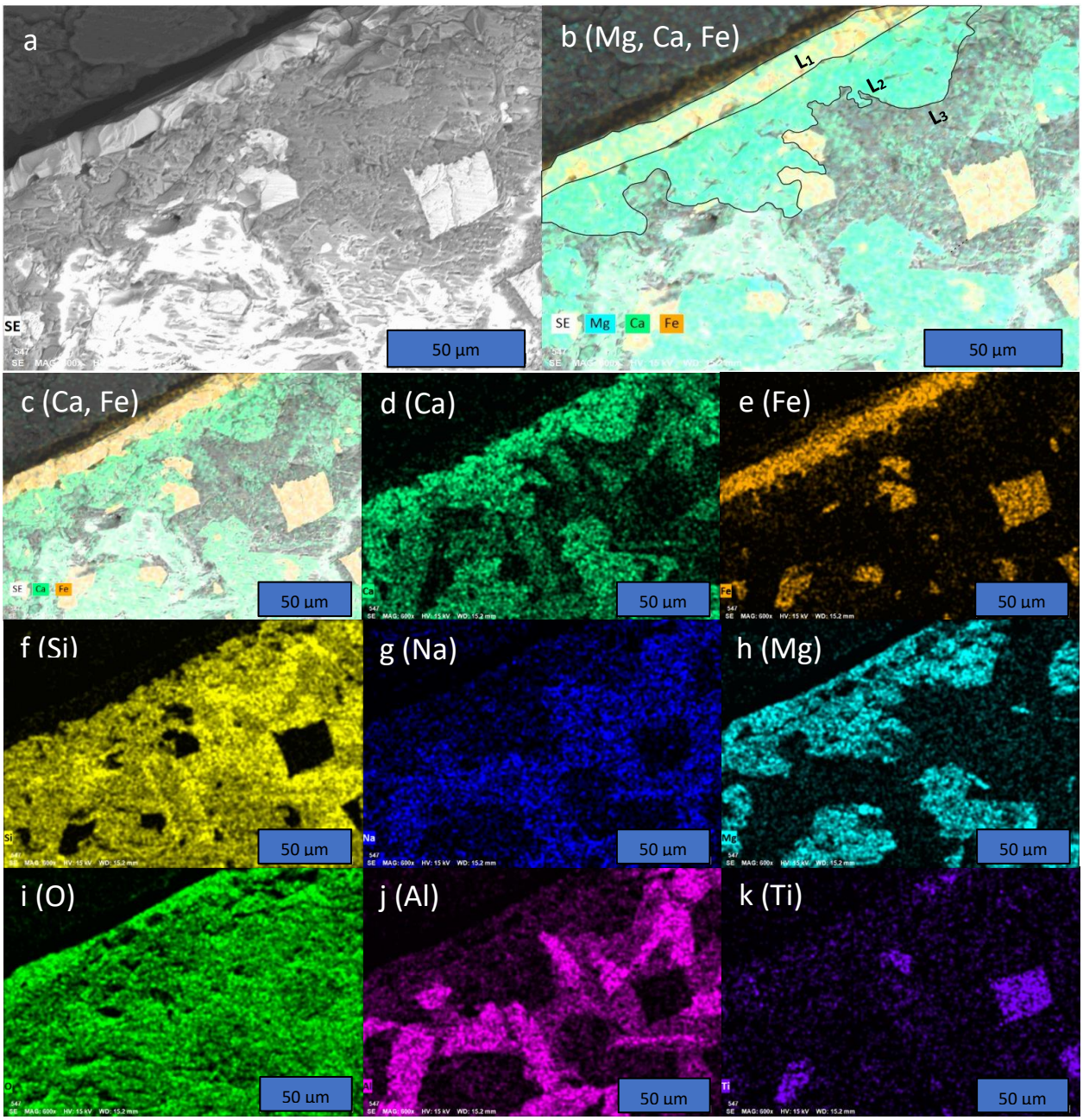

Figure 8 (a) BSE image of the cross-section of sample KK_22_01. **(b)** EDS map of magnesium, calcium, and iron. Layer one (L1), layer two (L2), and layer three (L3) are labelled and marked with black borders. **(c)** map of calcium and iron distribution, **(d)** calcium distribution, **(e)** iron distribution, **(f)** silica distribution, **(g)** sodium distribution, **(h)** magnesium distribution, **(i)** oxygen distribution, **(j)** aluminum distribution, **(k)** and titanium distribution.

titanomagnetite), often extending thousands of microns in length (figure 9a). The linear crystal groups don't have an obvious orientation, appearing in multiple directions. Additional Fe+Ti+O

crystals also appear in these samples, but with different shapes (Figure 9c). These features often resemble a hexagonal shape with a cross in the center, giving the impression of an octahedral shaped crystal. Alternatively, the hexagonal crystals and the linear crystal groups are the same crystals but viewed at different orientations. Samples from each lava tube system include Mg+Fe oxide crystals on the walls of vesicles (Figure 10). These crystals typically have a diameter of less than 100 microns and almost completely coat the interior. These crystal formations can also be seen on some surface veneers.

Mauna Loa

The Mauna Loa samples prepared at UH-Hilo weren't as extensively mapped due to time constraints, however their results reveal similar patterns to those found in Kipuka Kanohina and Puʻuʻōʻō. Of the four samples imaged, sample ML_22_03 was discovered to have a surface most consistent with those of the other two cave systems (Figure 11). The outer surface was composed of an Fe+O veneer, inferred to be hematite. Below the hematite veneer is a subsurface layer of Ca+Mg+Si+O (consistent with diopside). The third layer has an amorphous matrix with K, Al, Na, Si, and O.

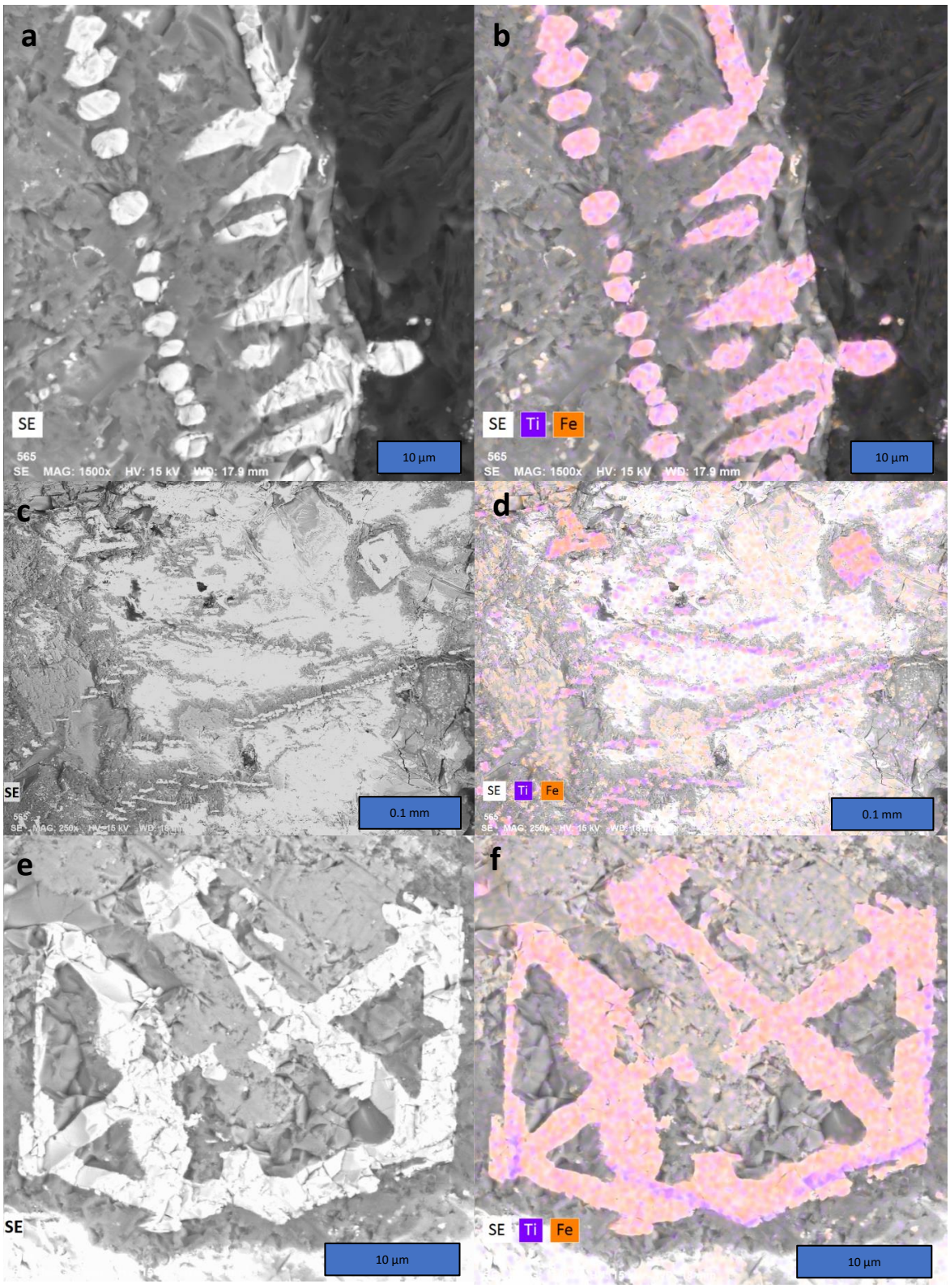

Figure 9 Cross section of PU_22_02 **(a)** 1500x BSE image of the linear markings **(b)** EDS map of titanium and iron distribution **(c)** 250x BSE image of linear markings with **(d)** titanium and iron distribution. **(e)** Hexagonal shape with cross **(f)** titanium and iron distribution.

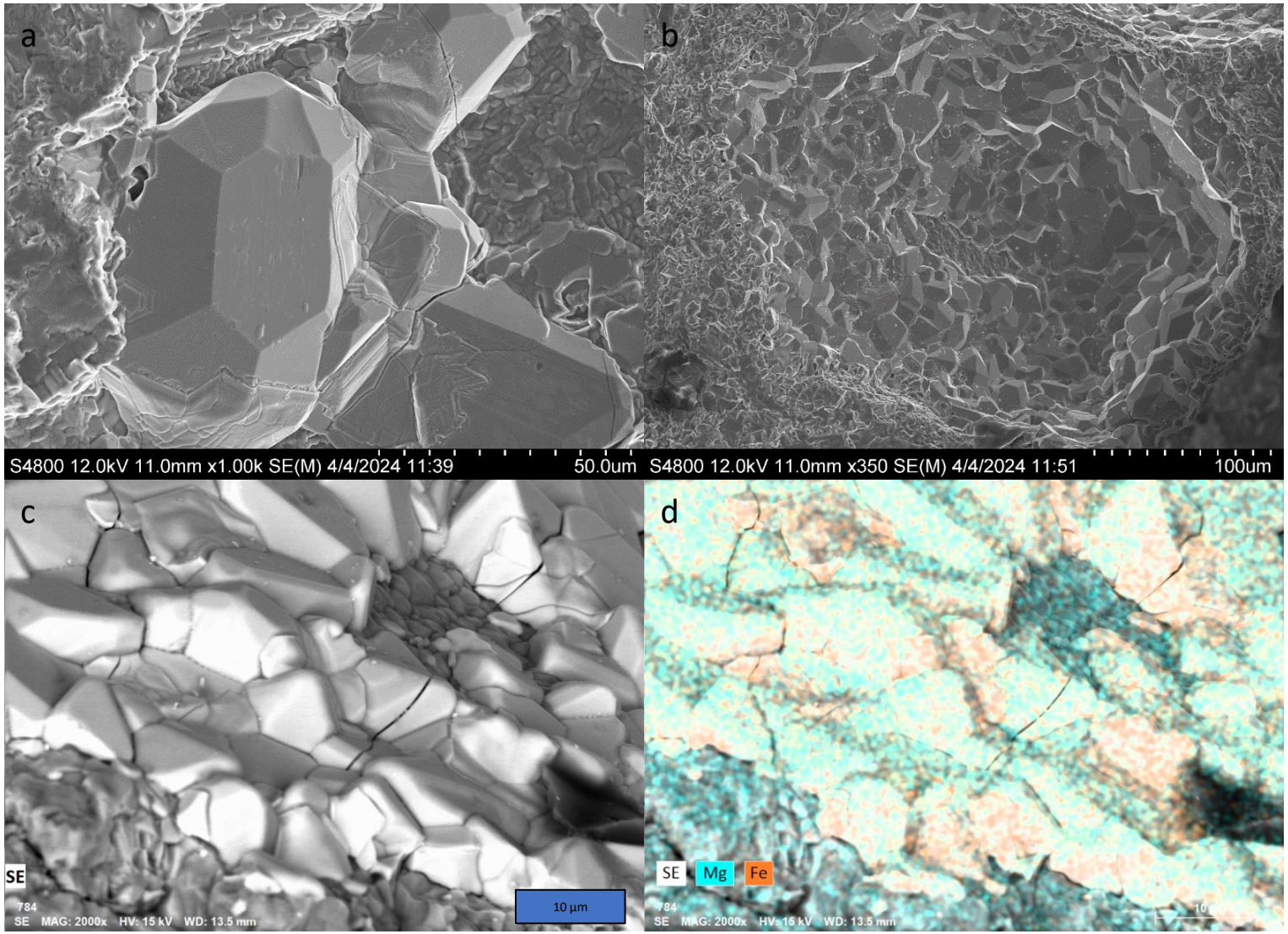

Figure 10 SEM images from sample KK_22_11. **(a)** 1000x SE close-up of a single Mg+Fe oxide crystal. **(b)** 350x SE image of a vesicle coated in oxide crystals. **(c)** BSE image of vesicle wall and **(d)** EDS map of magnesium and iron distribution.

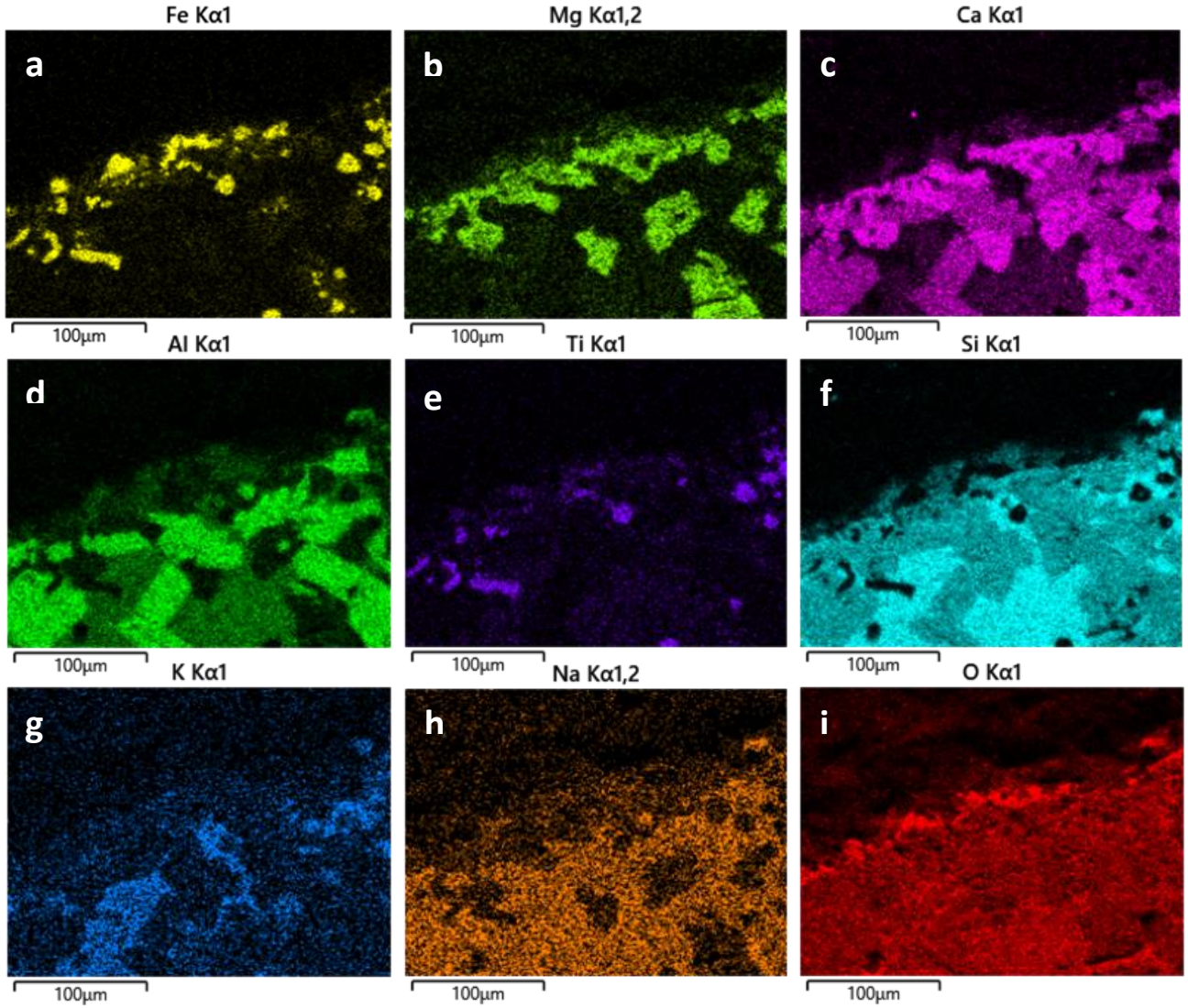

Figure 11 EDS images from sample ML_22_03 **(a)** map of the iron distribution **(b)** magnesium distribution, **(c)** calcium distribution, **(d)** aluminum distribution, **(e)** titanium distribution, **(f)** silica distribution, **(g)** potassium distribution, **(h)** sodium distribution, and **(i)** oxygen distribution. Each image is set to a 100-micron scale.

Discussion

XRD/Mineral Assemblage Discussion

One limitation in the experiment design for the XRD study is the accuracy of the surface veneer composition. SEM images reveal that the thicknesses of veneers are typically on the scale of tens of microns. The technique used to acquire ~1 gram of powdered veneer for XRD, using a rotary drill, yields material from both the veneer and to a variable degree from the interior of the sample. Therefore, the XRD patterns of the sample "surfaces" are likely a combination of both surface and interior mineralogy. BSE images and EDS element maps indicate the veneers are typically made up of magnesium, iron, and oxygen. This elemental distribution is interpreted to mean that the thin surface veneer is composed of magnesioferrite ($MgFe_2O_4$) and hematite (Fe_2O_3), both of which are also identified in many surface veneer XRD patterns.

Experimental studies reveal that magnesioferrite forms through the high-temperature oxidation of basaltic glass and olivine (e.g.- Wu and Kohlstedt et al., 1988; Cook et al., 1990; Khisina et al., 1995; Cooper et al., 1996). These experiments were conducted in open air environments and found that coatings of magnesioferrite formed on sample surfaces within 100h of exposure to temperatures between 600-770°C. Additional experiments have found that hematite can be produced under similar conditions (Minitti et al., 2005; Filiberto et al., 2020). Hematite can also be produced in low-temperature environments, however these results corroborated with SEM data indicate the magnesioferrite + hematite veneer formed by cation migration induced through high-temperature oxidation.

Cation migration is a process well documented by Cooper et al. (1996), and Minitti et al. (2005) provide a great summary of the process. Cation migration is a diffusion process that initiates with the reaction between atmospheric oxygen and Fe^{2+} at the surface. The atmospheric oxygen removes electrons from the ferrous iron, producing anionic oxygen that will bond to Fe or other cations (e.g.- Ca, Mg) at the surface to form oxides. This reaction, and subsequent formation of oxides on the surface, also creates two parallel reactions within the interior of the compound which includes the production of Fe^{3+} and a cation vacancy created by the removal of the cation to form the new oxide. The inward flux of a positive charge (or an electron "hole") and cation vacancy towards the interior is compensated by an outward flux of cations (e.g.- $Fe^{2+,}$ Mg^{2+}, Ca^{2+}) towards the surface. The cations that reach the surface can then become involved in oxide-producing reactions. Which oxides are produced during this process depends upon the temperature, oxygen fugacity, cation concentration, and the relative kinetics of the process involved (Khisina, 1995).

Tridymite and cristobalite are high-temperature polymorphs of quartz that typically crystallize at temperature ranges of 867°C-1470°C and 1150°C-1730°C respectively (Lakshtanov et al., 2007). However, cristobalite and tridymite can also form through the devitrification of glass at much lower temperatures (Heaney, 1994). Regardless of the mechanism, because they are associated with magnesioferrite and aren't present in the substrate samples, it is unlikely they formed at low temperatures. It is possible the silica polymorphs are a secondary product of the cation migration reaction. The dissolution and migration of $Fe^{2+,}$ Ca^{2+}, or Mg^{2+} cations from the interior towards the surface depletes the interior of these cations and enriches the interior with less mobile ions. This process creates an internal oxidation zone, typically enriched

in Si and O, which can lead to the formation of amorphous silica (Wu and Kohlstedt, 1988). However, at high temperatures, amorphous silica is prone to devitrification. The increased temperature relaxes the structure of the amorphous silica, allowing for the nucleation and the subsequent growth of crystalline silica phases (Cooper et al., 1996). This high-temperature environment coupled with the slow cooling of the lava tubes may have been a conducive environment for the formation of cristobalite and tridymite.

Gypsum is a common mineral found coating the interiors of lava tubes and coats the surfaces of several of the analyzed samples. While gypsum can form over these surfaces directly, it has also been observed to replace more soluble sulfates as a lava tube begins to cool (Sawlowics, 2020). When a lava tube isn't active and temperatures begin to lower, sulfate minerals begin to coat the walls. This includes the formation of anhydrous sulfates ($CaSO_4$, Na_2SO_4, $KNaSO_4$) and acid hydrated Mg-Fe-Al-Na sulfates (Hon et al., 2009; Sawlowics, 2020). As temperatures cool below 100 °C, liquid meteoric water is introduced to the lava tube and the more soluble sulfates are removed and replaced by gypsum. The gypsum found coating the analyzed samples may have formed initially or may have replaced sulfate minerals only stable under drier or hotter conditions.

Augite, anorthite, ilmenite, and titanomagnetite are assumed to be primary minerals that crystalized from the melt as they are common primary minerals and are found in the substrates of the sampled lava flows. Titanomagnetite was identified exclusively in the Pu‘u‘ō‘ō flow, and ilmenite also appeared in greater concentrations in this flow. These findings indicate a difference in magmatic composition/evolution between the Kilauea and Mauna Loa volcanoes (e.g. fractional crystallization or magma mixing; Wright, 1971). Pyroxene and iron spinels can

also form as secondary minerals through high-temperature oxidation, and experimental evidence suggests that these mineral products are likely to form under Venus like conditions (Gilmore et al., 2017). SEM analysis may show the formation of pyroxene as a secondary product and will be discussed further in the SEM section.

Magnetite is a secondary product expected to form through high-temperature oxidation (Cook et al., 1990). In Cook et al.'s experiment, magnetite and silica formed within the internal oxidation zone of basaltic glass while other oxides formed at the surface under high-temperature oxidation conditions. The presence of cristobalite and tridymite in the XRD results show that silica phases were formed. However, XRD results of the lava tube samples do not necessarily reveal the presence of magnetite within their interiors which is to be expected based on previous experiments. The XRD peaks of magnetite, magnesioferrite, and titanomagnetite have similar patterns, making it difficult to differentiate between these minerals. The similar XRD patterns can be explained by similarities between the compositions and crystal structures of these minerals. Each of the three minerals are a ferric iron bearing spinel. Magnetite is pure iron, magnesioferrite substitutes some Fe with Mg, and titanomagnetite substitutes some Fe with Ti. Subtle differences in their XRD patterns were used to distinguish between the three minerals. The substrate sample of Puʻuʻōʻō and lava tube sample PU_23_01 exhibit an additional peak at 2theta angle 35.4° that best aligns with the major peak of titanomagnetite, while a peak at 35.6° better aligns with magnesioferrite patterns available in the ICDD-2 database. Other samples display variations of broad and sharp peaks at 35.6 where both magnesioferrite and magnetite patterns fit, however SEM data is most consistent with magnesioferrite in the surface veneers and within vesicles (since Mg is

observed and Ti is not). The variations and shifts of this major peak around 2theta angle 35.6 may be caused by variations of cation substitutions within the iron spinels. Thus, when the basalt samples oxidized under high-temperatures, pure iron spinel (magnetite) was a less common product than iron spinels with partial substitutions of other cations. SEM imagery indicates that magnesium substitution (forming magnesioferrite) is the most common product in the surface veneers, but images also reveal iron oxides with copper and titanium enrichment too. These are interpreted to be iron spinels with copper and titanium substitutions.

VNIR

Analysis of the VNIR spectroscopic data reveals that each spectrum is largely dominated by ferric iron oxides, and based on the XRD results these can confidently be identified as hematite and magnesioferrite. While not ubiquitous, water also has a large presence in the sample spectra. Two samples (PU_22_07 and 11) contained hydroxyl bonds, which indicates the presence of hydrous minerals. For PU_22_07, each hydrous peak matches the pattern for gypsum, which was also detected in this sample using XRD. Sample PU_22_07 also has a small, broad absorption peak near the 2200 nm wavelength. A broad peak at this range suggests the presence of Si-OH bonds within the sample (Aines and Rossman, 1984). This could be explained by -OH impurities within the crystal lattice of silica, which based on XRD could be in the form of cristobalite, tridymite, or glass. Diagnostic spectral features for these phases are not found in the Near Infrared Region (NIR); samples would need to be analyzed in the Thermal Infrared Region (TIR) to better characterize the dominant silica mineral present. The high presence of

hydrous peaks in PU_22_07 suggests that it was subject to wetter conditions than any other sample.

The presence of Si-OH bonds is evidence of chemical interactions between water and silica minerals of PU_22_11. The absorption peak is very small, which indicates that these bonds are in low abundance. Samples PU_22_07 and 11 are outliers from the rest of the samples collected as they are the only samples featuring -OH bonds, specifically they both feature Si-OH bonds. This is interpreted to be due to the locations from which these two samples were collected within the cave system. Sample PU_22_07 was collected near a fumarolic vent in the interior of the cave, while PU_22_11 was collected at the mouth of the cave entrance. Both locations would be subject to wetter conditions.

Six of the samples showed an absorption feature at 1900 nm, indicative of the presence of molecular water. This water could be in the sample, in the mineral structure, or on the sample's surface. The spectrum of sample PU_22_07 has a sharp peak at this wavelength, meaning the water molecules occur in a well-defined site, whereas the rest of the samples show smaller broad peaks, meaning the water occurs in unordered sites (Gupta, 2017). This is likely because sample PU_22_07 has gypsum, where water occurs within the molecular structure. For the other samples with a random distribution of water (and no hydroxyl bonds), this suggests the water may be a "contaminant" and is independent from the mineral forming process.

At wavelengths greater than 1200 nm, the reflectance properties of each sample vary more widely. Six of the samples increase in reflectance towards the thermal infrared region and five of the samples decrease in reflectance. There are many variables that could change a

sample's spectral signature, so it's uncertain what causes this variance in reflectance. Potential factors include differences in mineral abundance on the surface, differences in surface texture, or differences in formation environment. When looking at data available for each of the minerals present in the basalt samples in spectral libraries (e.g.- PDS Geosciences Node Spectral Library, USGS Digital Spectral Library, JPL ASTER Spectral Library, etc.), it appears that to date there is no VNIR reflectance spectroscopy data for magnesioferrite. XRD and SEM data both confirm its presence on the surface, but it is unknown how it might influence the spectra.

SEM

Using the elemental maps in conjunction with XRD data, we can make inferences on the mineralogical composition of each layer. The first layer is interpreted to consist of magnesioferrite and hematite. The second layer is interpreted to be diopside. The third layer or the subsurface is not homogenous and is interpreted to be composed of multiple minerals within an amorphous matrix. Based on the elemental distributions, the minerals in the subsurface include augite, anorthite, and ilmenite. There were two minerals found in SEM that were not detected by XRD, suggesting that they are present in very minor concentrations. The calcium phosphate mineral found in PU_22_02 is likely apatite. The copper and iron oxide mineral found on the surface of KK_22_02 may be a copper spinel (cuprospinel). This would be consistent with the dominant presence of ferric iron-bearing spinel on the surface.

The distribution of elements throughout the surface and subsurface of the samples are like those produced in high-temperature oxidation experiments, like Cook et al. (1990). As mentioned in the XRD discussion section, the secondary minerals are likely a product of this

process. In the EDS imagery we see an enrichment of Fe, Mg, and Ca near the surface, along with Ti in some samples. Copper was identified in the surficial oxide layer in one sample.

SEM element maps of the veneer reveal that their compositions aren't always homogenous (figure 12). In some images, there is a clear separation of a Mg+Fe oxide layer and an Fe oxide layer within the veneer. This finding is consistent with XRD patterns that indicate that hematite and magnesioferrite are both present on the surface. However, it's uncertain why magnesium is only present in the outer portion of the veneer. Since the oxide phases produced depend on variables like temperature and oxygen fugacity, one idea is that the

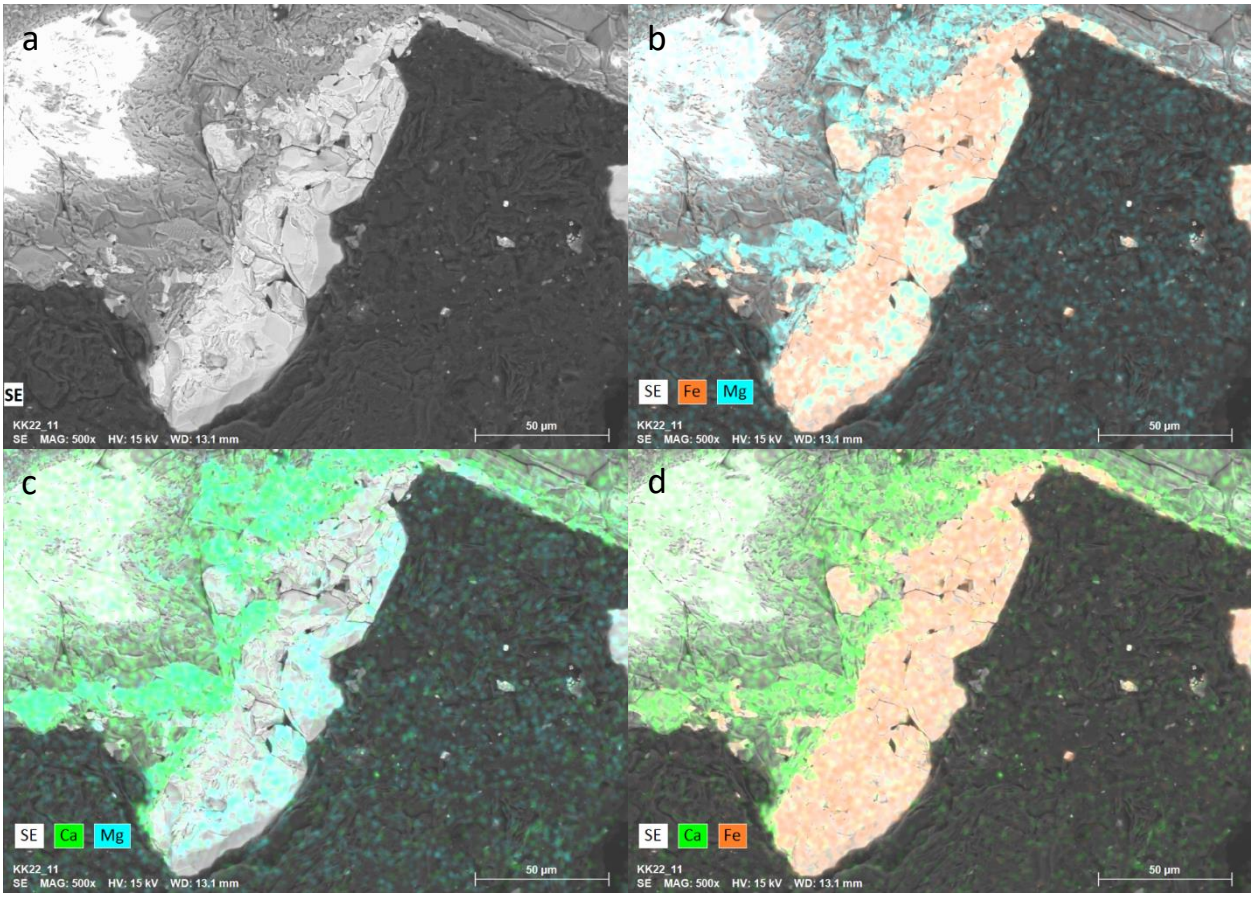

Figure 12 Cross section of PU_22_02 **(a)** BSE image of surface veneer. **(b)** EDS map of magnesium and iron distribution, **(c)** calcium and magnesium distribution, **(d)** calcium and iron distribution.

hematite to magnesioferrite transition may be a product of temperature changes in the lava tube.

Directly under the magnesioferrite and hematite veneer is a layer of diopside. This layer is formed through the transportation and subsequent enrichment of calcium and magnesium. Silicon and oxygen are also found in this layer; however, these ions are considered largely immobile and therefore this second layer likely represents the basalt's original surface upon which the oxide minerals grew (Cooper et al., 1996). This ordering of cations may indicate that calcium was the least mobile of the three cations consistently found near the surface (Ca, Mg, Fe). This layer may also be a product of changes in fugacity conditions. In this instance pyroxene crystals may have formed first under the hottest temperatures and then oxide crystals began coating them as temperatures cooled (Figure 13).

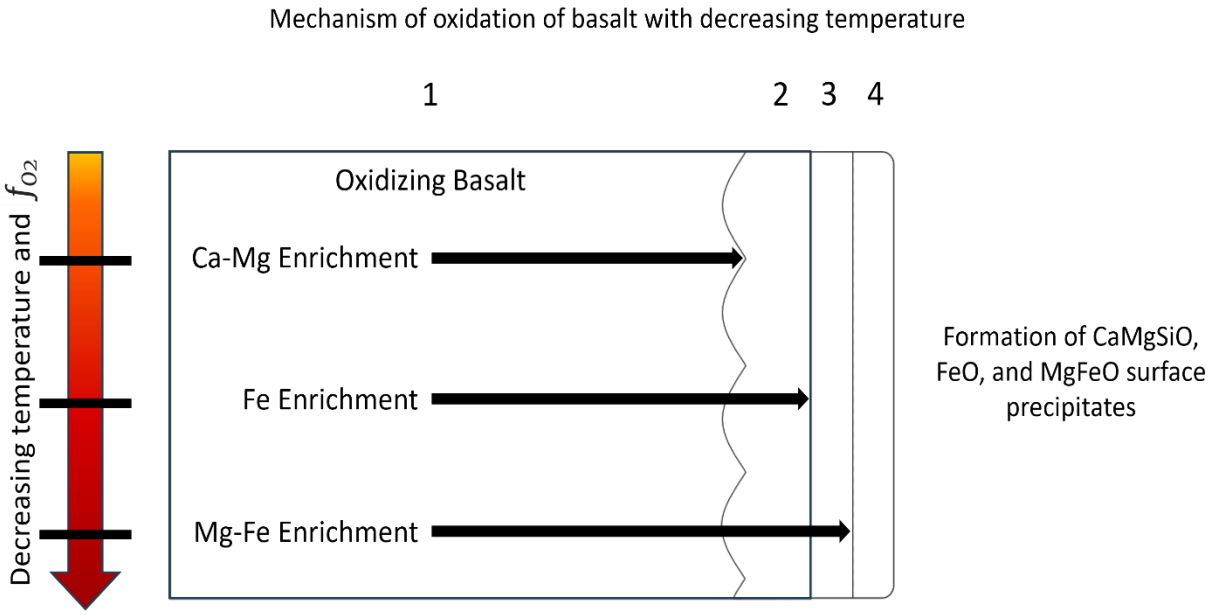

Figure 13 Predicted mechanism for the formation of surface precipitates of basalt at high temperatures. **(1)** Initial oxidation of basalt and diffusion of cations towards the surface, **(2)** at the highest temperatures, Ca and Mg ions diffuse and form diopside in the subsurface, **(3)** after the formation of diopside initiates, Fe ions diffuse and form iron oxides (hematite) at the surface. **(4)** As temperatures lower, Mg and Fe ions diffuse to form oxides (magnesioferrite) over the surface of the layer of hematite.

As the cations migrate towards the surface, the area they leave becomes depleted in the more mobile ions and enriched in the less mobile ions (Wu and Kohlstedt, 1988). In layer three, the amorphous portions are likely a product of this internal oxidation process. This area has little to no iron, magnesium, and calcium compared to layer two. Instead, less mobile cations in these conditions like Na, Al, and Si are dominant. This zone is where the amorphous silica and subsequent silica phases (cristobalite and tridymite) would be produced, however no distinct silica phase crystals were observed in SEM (despite their presence in the XRD patterns of some of these samples).

Most vesicles in the samples contained magnesium+iron oxide crystals coating the surface. These crystals are interpreted to be magnesioferrite. The presence of magnesioferrite on the surfaces of vesicles within the basalt implies the gases within these vesicles induced high-temperature oxidation too. As noted by Cook et al. (1990), this internal oxidation reaction is often utilized by manufacturing companies to remove air bubbles in their molten glass. If this process applies to basaltic glass, then molten basalt (lava) oxidized at high temperatures may also result in a less vesicular rock. Evidence of this can be seen in a cross-section of hand sample KK_22_01 (Figure 14).

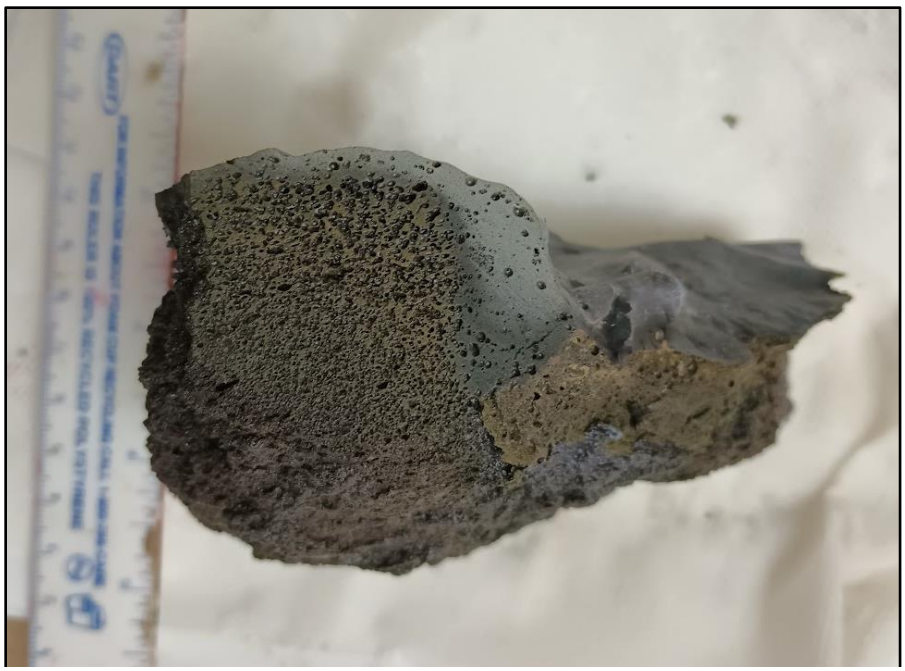

Figure 14 Photograph taken of sample KK_22_01 cross-section. Note the change in vesicularity between the outer surface and interior.

The features composed of Fe+Ti+O found on the interior of the Puʻuʻōʻō samples are ilmenite or titanomagnetite. The polyhedral shapes appear to be crystalline, however the linear trends are more puzzling. As ilmenite and titanomagnetite are both primary igneous minerals, it's unlikely these features are a product of later oxidation processes, however the process that led to their linear trend is uncertain.

Comparing Results Between Lava Tubes

The results from the three lava tube system examined in this study are relatively consistent. The variations found in VNIR spectra of sample surfaces appear to be more dependent on the individual sample rather than the cave system from which it was collected. SEM results show that high-temperature oxidation occurred in each of the lava tube systems, which caused cation migration and formed the magnesioferrite/hematite veneers. XRD

patterns reveal that differences in the assemblage of primary igneous minerals appear to explain the overall mineralogical/compositional differences between samples. The ~800-year-old Kipuka Kanohina and ~180 year old Mauna Loa flow both have lower concentrations of ilmenite than Pu‘u‘ō‘ō. This could indicate differences between the magmatic sources (Mauna Loa vs. Kilauea), or it could also be caused by more conventional weathering. Since the Mauna Loa flows are older and have been exposed to Earth’s environment for longer, their primary minerals have had more time to break down into more stable secondary minerals like hematite through low-temperature aqueous processes.

Secondary minerals, particularly the oxides and silicates, are consistent among all the samples from each of the lava tube systems. Both the 2016-2018 Pu‘u‘ō‘ō flow and the ~1200 Kipuka Kanohina flow still contain a hematite and magnesioferrite veneer, with a diopside and silica enriched subsurface. This suggests that once a lava tube cools and is exposed to ambient Earth conditions, these veneers and silicate subsurfaces remain stable for at least hundreds of years.

Significance to Venus

The biggest caveats to this study regarding its relevance to Venus are the differences in temperature, pressure, and atmospheric composition of lava tubes compared to the surface of Venus (Table 3). The exact atmospheric composition of a lava tube during cooling is uncertain, but it will be composed of a combination of volatiles degassed from the lava itself and some portion of normal Earth air. This indicates that the similarity of a lava tube’s atmospheric composition to Venus’ will depend on how volatile-rich the flow is, and the climate surrounding

it. After the eruption of a volcano ends, and a lava tube is no longer actively supplied with lava, temperatures will begin to lower, lava will solidify, and degassing will cease. As temperatures cool, the humidity of a lava tube will typically increase due to an influx in atmospheric air and evaporated water (although how long this takes can depend on the climate; Forti, 2005; Sawlowics, 2020). During the cooling stage is also when sulfate mineral formation is most dominant. This suggests that the sulfur fugacity of lava tubes is most Venus-like during the cooling stage. As temperatures drop below 100°C, meteoric water can enter the system and aqueous alteration will begin. This means that at some point during the cooling phase, the lava tube will become too wet to represent current Venus weathering conditions.

The walls of active lava tubes on the Big Island of Hawai'i have consistently been recorded at temperatures above 900°C (Helz et al., 2003; Witter and Harris, 2007). These temperatures far exceed Venus' average surface temperature of 467°C. This means that weathering reactions during the active stages of tholeiitic lava tubes occur at a higher temperature and oxygen fugacity than that in ambient Venus conditions. However, as demonstrated by this study, it's worth considering that 1: the temperatures that lava flows are exposed to can vary based on the eruptive environment, and 2: lava flows on Venus would cool at a much slower rate, which means that they'd be exposed to these intermediate

temperatures (between the initial molten temperature and ambient surface temperatures) for an extended period compared to surface lava flow on Earth.

	Venus	Earth	Lava Tube Interior*
Temperature	~467°C	~15°C	>900°C
Pressure	~96 bars	1 bar	1 bar
CO_2	96.5 ± 0.8%	$3.45x10^{-4}$ %	?
N_2	3.5 ± 0.8%	78.08%	?
SO_2	150 ± 30 ppm	$3x10^{-10}$ %	?
H_2O	30 ± 15 ppm	$2x10^{-6}$ - $3x10^{-2}$ %	?
O_2	-	20.95%	?

Table 3 Environmental conditions and the compositions of five major gases in the atmospheres of Venus and Earth compared to the interior of tholeiitic lava tubes. Atmospheric compositions are measure by volume percent. ppm = parts per million by volume. Venus data from Zolotov, 2018. Earth data from Allen and Cox, 2000.
*Listed temperature is based on recordings of ceiling and wall measurements of an active lava tube by Witter and Harris (2007). Both temperature and atmospheric composition of a lava tube will vary between the active, cooling, and inactive stages.

The atmospheric pressure on Earth is far less than that of Venus (96 bars vs. 1). The reactions and mineral formations within lava tubes thus occur at much lower pressures than that of the surface of Venus. However recent high-temperature, high-pressure basalt-weathering experiments reveal that the differences in pressure produce negligible differences in mineralogical compositions (Merchak et al., 2024). In terms of comparing lava-tube weathering conditions to those on the surface of Venus, it appears that the dynamic environment of lava tubes make them more Venus-like or less Venus-like depending on the type of lava flowing through it, the climate surrounding it, and whether the lava tube is active,

cooling, or inactive. Based on evidence available so far, lava tubes are most Venus-like when they are produced by tholeiitic flows, in a dry climate, during their cooling stage.

XRD, SEM, and VNIR analyses all indicate that the surface veneers present on the ceilings and walls of lava tubes formed in a dry, high-temperature environment. This process not only forms the oxide coating on the surface but forms amorphous silica as a byproduct of cation migration. This amorphous silica, unstable at high temperatures, is more likely to devitrify and produce crystalline silica like the cristobalite and tridymite present in our samples. The high-temperature oxidation likely begins producing these veneers during the active stage of a lava tube and ends when temperatures become sufficiently low during the cooling stage.

While this process likely occurs at a higher oxygen fugacity than that on Venus, these data still shows similar results compared to those produced by Berger et al. (2019) in a laboratory setting simulating Venus conditions. In the current lava tube study, SEM results show three distinct layers in the cross-sections of basalts. The outer veneer is enriched in Fe, Mg and sometimes Ti, and is composed of both hematite and magnesioferrite. The subsurface is enriched in Ca and Mg and is composed of diopside. The inner layer is composed of various minerals surrounded by an amorphous matrix. The amorphous matrix is depleted in Fe, Mg, and Ti. Moreover, it is enriched in Na, Al, and Si. In the experiment conducted by Berger et al. (2019), a basaltic glass sample was set in conditions simulating the temperature, pressure, and atmospheric composition of current Venus for eight days. The glass formed magnesioferrite dendrites in the subsurface, enriched in Fe, Mg, and Ti crystals. The glass around the dendrites was depleted in Fe, Mg, Ti, Na, and Ca. The same area was enriched in Si and Al. The surface above the magnesioferrite contained a Ca, Na SO_4 precipitate.

Both the lava tube samples and the basaltic glass experiment show similar patterns of ion enrichment and depletion between the surface and the inner oxidized layer. However, a key difference between the two is that the basalt formed a pyroxene subsurface with a magnesioferrite veneer, whereas the experimental glass formed a magnesioferrite subsurface with a sulfate veneer. Thermochemical models of Venus' surface better align with Berger et al.'s (2019) results; diopside is not expected to be stable exposed to Venus surface atmospheric conditions (Gilmore et al., 2017). Instead, the diopside would react with atmospheric sulfur to form anhydrite, enstatite, and quartz. Santos et al. (2023) describe another study that placed basaltic glass and rock samples in simulated Venus conditions. In this study the experiments lasted for either 11 or 30 days. The basaltic glass oxidized and formed secondary phases consisting of Ca,S,O crystals, Fe,S crystals, and Fe,O bearing crystals. The basaltic rock samples did not display any obvious signs of alteration following the 11- or 30-day experiments.

As demonstrated by Wu and Kohlstedt (1998), the thickness of the external layer not only increases with temperature at a fixed oxidation time, but also with increasing oxidation time at a fixed temperature. An advantage to taking samples from lava tubes is that the basalt is exposed to high-temperature oxidizing conditions for many months, whereas laboratory experiments are often limited in how long they can conduct an experiment. As demonstrated by Santos et al. (2023), sometimes the experiment durations aren't long enough to initiate any alteration reactions. The lava tube samples display a continuous veneer across the entire surface of the rock, which reveals what the results of a more complete oxidation process looks like. If the laboratory experiments were conducted for more extensive time periods, the results may look more like the surfaces of lava tubes.

In addition to forming high-temperature oxidized basalts, lava tubes may also help us to better understand how lava behaves in a hot, slow-cooling surface environment. Images of lava flows on Venus indicate that hot surface temperatures may account for the great distances they travel across the surface (Schaber et al., 1992). This is in large part what allows lava within lava tubes to travel such great distances as well (Helz et al., 2003). Aside from creating longer lava flows, these processes have implications for the texture and crystallinity of basaltic rocks on Venus. At higher temperatures, glass is more prone to devitrification and may lead to the production of silica phases, as seen in these samples. Additionally, oxides within a glass melt can help remove air from within the glass. The various high-temperature processes that occur in lava tubes warrant further studies to better understand the geologic processes occurring on the surface of Venus. Not just limited to Venus, these processes can teach us more about geologic processes on other hot planets or on early Earth.

Conclusion

This study demonstrates that the surface veneers present on the walls and ceilings of lava tubes formed at high temperatures and are mineralogically similar to those expected to form for tholeiitic lava flows exposed to Venusian weathering conditions. The surface veneers of lava tubes are composed of hematite and magnesioferrite and are a product of high-temperature oxidation. The upper surface is enriched in Mg, Fe, and Ca. The amorphous subsurface is depleted in Mg, Fe, and Ca but enriched in less mobile ions like Na and Al. This amorphous layer in the subsurface represents the internal oxidized zone. This amorphous layer may have produced cristobalite and tridymite through high-temperature devitrification. The

secondary minerals produced at high temperatures likely form at a higher oxygen fugacity than that of current surface conditions of Venus. However, the formation of oxide and sulfate layers over the surfaces of these samples are consistent with samples oxidized under Venus-like conditions in laboratory experiments. These results indicate that the walls and ceilings of lava tubes warrant further investigation to help us understand weathering processes on hot planets, like Venus. Additionally, lava tubes may teach us more about how slow cooling environments alter the solidification and texture of a lava flow.

References

Aines, Roger D.; Rossman, George R. (1984). Water in minerals? A peak in the infrared. Journal of Geophysical Research, 89(B6), 4059–4071.

Allen, C. W., & Cox, A. N. (2000). *Allen's astrophysical quantities (Fourth ed.)*. Springer Science & Business Media, 258.

Barsukov, V. L., Volkov, V. P., & Khodakovsky, I. L. (1982). The crust of Venus: Theoretical models of chemical and mineral composition. Journal of Geophysical Research, 87(S01), A3. doi:10.1029/jb087is01p000a3

Barsukov, V. L., Basilevsky, A. T., Burba, G. A., Bobinna, N. N., Kryuchkov, V. P., Kuzmin, R. O., Nikolaeva, O. V., Pronin, A. A., Ronca, L. B., Chernaya, I. M., Shashkina, V. P., Garanin, A. V., Kushky, E. R., Markov, M. S., Sukhanov, A. L., Kotelnikov, V. A., Rzhiga, O. N., Petrov, G. M., Alexandrov,, Yu. N., Sidorenko, A. I., Bogomolov, A. F., Skrypnik, G. I., Bergman, M. Yu., Kudrin, L. V., Bokshtein, I. M., Kronrod, M. A., Chochia, P. A., Tyuflin, Yu. S., Kadnichansky, S. A., and Akim, E. L. (1986). The geology and geomorphology of the Venus surface as revealed by the radar images obtained by Veneras 15 and 16. Journal of Geophysical Research: Solid Earth, 91(B4), 378-398.

Berger, G., Cathala, A., Fabre, S., Borisova, A. Y., Pages, A., Aigouy, T., Esvan, J., and Pinet, P. (2019). Experimental exploration of volcanic rocks-atmosphere interaction under Venus surface conditions. Icarus, 329, pp. 8-23.

Byers, H.L., McHenry, L.J. and Grundl, T.J., 2016. Forty-Nine Major and Trace Element Concentrations Measured in Soil Reference Materials NIST SRM 2586, 2587, 2709a, 2710a and 2711a Using ICP-MS and Wavelength Dispersive-XRF. Geostandards and Geoanalytical Research, 40(3), pp.433-445.

Cloutis, E. A., Craig, M. A., Kruzelecky, R. V., Jamroz, W. R., Scott, A., Hawthorne, F. C., and Mertzman, S. A. (2008). Spectral reflectance properties of minerals exposed to simulated Mars surface conditions. Icarus, 195(1), 140–168. doi:10.1016/j.icarus.2007.10.02

Cook, G. B., Cooper, R. F., and Wu, T. (1990). Chemical diffusion and crystalline nucleation during oxidation of ferrous iron-bearing magnesium aluminosilicate glass. Journal of Non-Crystalline Solids, 120(1-3), 207–222. doi:10.1016/0022-3093(90)90205-z

Cooper, R. F., Fanselow, J. B., and Poker, D. B. (1996). The mechanism of oxidation of a basaltic glass: Chemical diffusion of network-modifying cations. Geochimica et Cosmochimica Acta, 60(17), 3253–3265. doi:10.1016/0016-7037(96)00160-3

Cutler, K. S., Filiberto, J., Treiman, A. H., and Trang, D. (2020). Experimental investigation of oxidation of pyroxene and basalt: Implications for spectroscopic analyses of the surface of Venus and the ages of lava flows. The Planetary Science Journal, 1(1), 21.

Dyar, M. D., Helbert, J., Cooper, R. F., Sklute, E. C., Maturilli, A., Mueller, N. T., Kappel, D., and Smrekar, S. E. (2021). Surface weathering on Venus: Constraints from kinetic, spectroscopic, and geochemical data. Icarus, 358, 114139.

Eaton, J. P., and Murata, K. J. (1960). How Volcanoes Grow: Geology, geochemistry, and geophysics disclose the constitution and eruption mechanism of Hawaiian volcanoes. Science, 132(3432), 925-938.

Filiberto, J., Trang, D., Treiman, A. H., and Gilmore, M. S. (2020). Present-day volcanism on Venus as evidenced from weathering rates of olivine. Science Advances, 6(1), eaax7445.

Foley, B. J. (2015). The role of plate tectonic–climate coupling and exposed land area in the development of habitable climates on rocky planets. The Astrophysical Journal, 812(1), 36.

Garvin, J. B., Getty, S. A., Arney, G. N., Johnson, N. M., Kohler, E., Schwer, K. O., Sekerak, M., Bartels, A., Saylor, R. S., Elliott, V. E., Goodloe, C. S., Garrison, M. B., Cottini, V., Izenberg, N., Lorenz, R., Malespin, C. A., Ravine, M., Webster, C. R., Atkinson, D. H., Aslam, S., Atreya, S., Bos, B. J., Brinckerhoff, W. B., Campbell, B., Crisp, D., Filiberto, J. R., Forget, F., Gilmore, M., Gorius, N., Grinspoon, D., Hofmann, A. E., Kane, S. R., Kiefer, W., Lebonnois, S., Mahaffy, P. R., Pavlov, A., Trainer, M., Zahnle, K. J., and Zolotov, M. (2022). Revealing the mysteries of Venus: The DAVINCI mission. The Planetary Science Journal, 3(5), 117.

Ghail, R. C., Hall, D., Mason, P. J., Herrick, R. R., Carter, L. M., and Williams, E. (2018). VenSAR on EnVision: Taking earth observation radar to Venus. International journal of applied earth observation and geoinformation, 64, 365-376.

Gilmore, M., Treiman, A., Helbert, J., and Smrekar, S. (2017). Venus Surface Composition Constrained by Observation and Experiment. Space Science Reviews, 212(3-4), 1511–1540.

Gilmore, M. S., Darby Dyar, M., Mueller, N., Brossier, J., Santos, A. R., Ivanov, M., Ghail, R., Filiberto, J., and Helbert, J. (2023). Mineralogy of the Venus surface. Space Science Reviews, 219(7), 52.

Guimbretière, G., Canizarès, A., Finizola, A., Delcher, E., Raimboux, N., Veron, E., Simon, P., Devouard, B. & Bertil, A., 2014. Raman study of secondary minerals in a recent lava tube. In: 11th GeoRaman International Conference, June 15–19, 2014, St. Louis, Missouri, USA. https:// www.hou.usra.edu/meetings/georaman2014/pdf/5057.pdf [10.02.2021; 2 pp.].

Gupta, R. P. (2017). Remote sensing geology. Springer, 25-31.

Heaney, P. J. (1994). Chapter 1. Structure and Chemistry of the Low-Pressure Silica Polymorphs. Silica, 1–40.

Heliker, C., and Mattox, T. N. (2003). The First Two Decades of the Pu'u ʻŌ'ō-Kūpaianaha. The Puʻu ʻŌʻō-Kūpaianaha Eruption of Kīlauea Volcano, Hawaiʻi: The First 20 Years, 1676(1676), 1.

Helz, R.T., Heliker, C., Hon, K., and Mangan, M. (2003). Thermal Efficiency of Lava Tubes in the Puʻu ʻŌʻō-Kūpaianaha Eruption. The Pu ʻu ʻÖ ʻö-Küpaianaha Eruption of Kïlauea Volcano, Hawai ʻi: The First 20 Years, 1676, 105.

Hon, K., Bove, D. J., Lee, L. and Thornber, C., 2009, The origin and zonation of sublimates and precipitates in active Hawaiian lava tubes. Geological Society of America Abstracts with Programs, 41 (7): 193.

Herrick, R. R., & Hensley, S. (2023). Surface changes observed on a Venusian volcano during the Magellan mission. Science, 379(6638), 1205-1208.

Khisina, N. R., Khramov, D. A., Kolosov, M. V., Kleschev, A. A., and Taylor, L. (1995). Formation of ferriolivine and magnesioferrite from Mg ? Fe-olivine: Reactions and kinetics of oxidation. Physics and Chemistry of Minerals, 22(4). doi:10.1007/bf00202257

Krissansen-Totton, J., Fortney, J. J., and Nimmo, F. (2021). Was Venus ever habitable? Constraints from a coupled interior–atmosphere–redox evolution model. The Planetary Science Journal, 2(5), 216.

Kreslavsky, M. A., Ivanov, M. A., and Head, J. W. (2015). The resurfacing history of Venus: Constraints from buffered crater densities. Icarus, 250, 438–450.

Lockwood, J. P., and Lipman, P. W. (1987). Holocene eruptive history of Mauna Loa volcano. US Geol. Surv. Prof. Pap, 1350(1), 509-535.

Lakshtanov, D. L., Sinogeikin, S. V., and Bass, J. D. (2007). High-temperature phase transitions and elasticity of silica polymorphs. Physics and Chemistry of Minerals, 34, 11-22.

McHenry, L. J. (2009). Element mobility during zeolitic and argillic alteration of volcanic ash in a closed-basin lacustrine environment: Case study Olduvai Gorge, Tanzania. Chemical Geology, 265(3-4), 540-552.

Merchak, E. J., Port, S. T., and Chevrier, V. F. (2024). Experimental Alteration of Primary Basaltic Minerals Under Simulated Venus' Surface Environment. *LPI Contributions* 3040: 1693.

Minitti, M. E., Lane, M. D., and Bishop, J. L. (2005). A new hematite formation mechanism for Mars. Meteoritics & Planetary Science, 40(1), 55-69.

Neal, C. A., Brantley, S. R., Antolik, L., Babb, J. L., Burgess, M., Calles, K., Cappos, M., Chang, J. C., Conway, S., Desmither, L., Dotray, P., Elias, T., Fukunaga, P., Fuke, S., Johanson, I. A., Kamibayashi, K., Kauahikaua, J., Lee, R. L., Pekalib, S., Miklius, A., Million, W., Moniz, C. J., Nadeau, P. A., Okubo, P., Parcheta, C., Patrick, M. R., Shiro, B., Swanson, D. A., Tollett, W., Trusdell, F., Younger, E. F., Zoeller, M. H., Montgomery-Brown, E. K., Anderson, K. R., Poland, M. P., Ball, J. L., Bard, J., Coombs, M., Dietterich, H. R., Kern, C., Thelen, W. A., Cervelli, P. F., Orr, T., Houghton, B. F., Gansecki, C., Hazlett, R., Lundgren, P., Diefenbach, A. K., Lerner, A. H., Waite, G., Kelly, P., Clor, L., Werner, C., Mulliken, K., Fisher, G., and Damby, D. (2019). The 2018 rift eruption and summit collapse of Kīlauea Volcano. Science, 363(6425), 367-374.

Porter, A. (2000). The initial exploration of lower Lae'apuki cave system, Hawai'I volcanoes national park. NSS News, 58(1), 10-17.

Santos, A. R., Gilmore, M. S., Greenwood, J. P., Nakley, L. M., Phillips, K., Kremic, T., and Lopez, X. (2023). Experimental weathering of rocks and minerals at Venus conditions in the Glenn Extreme Environments Rig (GEER). Journal of Geophysical Research: Planets, 128(3), e2022JE007423.

Sawłowicz, Z. (2020). A short review of pyroducts (lava tubes). In Annales Societatis Geologorum Poloniae. Vol. 90, No. 4, 513-534.

Schaber, G. G., Strom, R. G., Moore, H. J., Soderblom, L. A., Kirk, R. L., Chadwick, D. J., Dawson, D. D., Gaddis, L. R., Boyce, J. M., and Russell, J. (1992). Geology and distribution of impact craters on Venus: What are they telling us? Journal of Geophysical Research, 97(E8), 13257. doi:10.1029/92je01246

Smrekar, S., Hensley, S., Nybakken, R., Wallace, M. S., Perkovic-Martin, D., You, T. H., Nunes, D., Brophy, J., Ely, T., Burt, E., Darby, D. M., Helbert, J., Miller, B., Hartley, J., Kallemeyn, P., Whitten, J., Less, L., Mastrogiuseppe, M., Younis, M., Prats, P., Rodriguez, M., and Mazarico, E. (2022, March). VERITAS (Venus emissivity, radio science, InSAR, topography, and spectroscopy): a discovery mission. In 2022 IEEE Aerospace Conference (AERO) (pp. 1-20).

Smrekar, S. E., Stofan, E. R., Mueller, N., Treiman, A., Elkins-Tanton, L., Helbert, J., Piccioni, G., and Drossart, P. (2010). Recent hotspot volcanism on Venus from VIRTIS emissivity data. Science, 328(5978), 605-608

Surkov, I. A., Kirnozov, F. F., Glazov, V. N., and Fedoseev, G. A. (1976). Investigations of Venusian gamma-radiation by Venera 9 and Venera 10. COSPAR Meeting.

Surkov, Y. A., Moskalyova, L. P., Kharyukova, V. P., Dudin, A. D., Smirnov, G. G., and Zaitseva, S. Y. (1986). Venus rock composition at the Vega 2 landing site. Journal of Geophysical Research: Solid Earth, 91(B13), 215-218.

Thornber, C. R. (2001). Olivine Liquid Relation of Lava Erupted by Kilauea Volcano From 1994 to 1998: Implication for Shallow Magmatic Processes Associated with the Ongoing East-Rift-Zone Eruption. The Canadian Mineralogist, 39(2), 239–266.

Vinogradov, A. P., Surkov, Y. A., and Kirnozov, F. F. (1973). The content of uranium, thorium, and potassium in the rocks of Venus as measured by Venera 8. Icarus, 20(3), 253-259.

White, W. B. (2010). Secondary minerals in volcanic caves: data from Hawai'i. Journal of Cave and Karst Studies, 72(2), 75-85.

Witter, J. B., and Harris, A. J. L. (2007). Field measurements of heat loss from skylights and lava tube systems. Journal of Geophysical Research, 112(B1). doi:10.1029/2005jb003800

Wright, T. L. (1971). Chemistry of Kilauea and Mauna Loa lava in space and time (No. 735). US Govt. Print. Off.

Wu, T., and Kohlstedt, D. L. (1988). Rutherford Backscattering Spectroscopy Study of the Kinetics of Oxidation of (Mg, Fe)2SiO4. Journal of the American Ceramic Society, 71(7), 540–545. doi:10.1111/j.1151-2916.1988.tb05917.x

Yang, J., Wang, C., Zhang, J. and Jin, Z. (2023). Genesis of Hawaiian lavas by crystallization of picritic magma in the deep mantle. Nature Communications 14, 1382.

Zolotov, M. Y. (2018). Gas–solid interactions on Venus and other solar system bodies. High Temperature Gas-Solid Reactions in Earth and Planetary Processes, 351-392.

Appendix A: XRD Plots

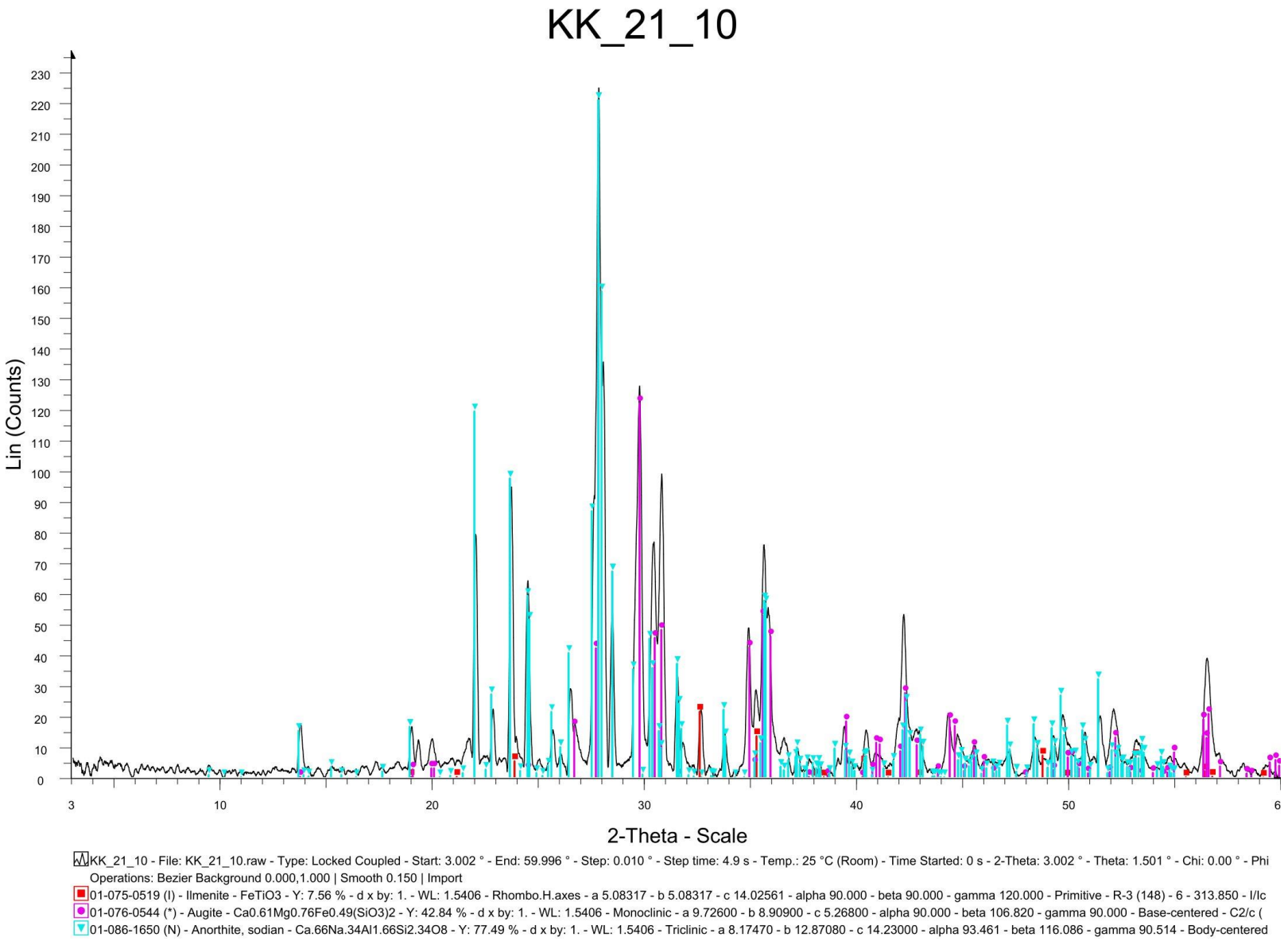

Figure 15 XRD Plot for KK_21_10, the Kipuka Kanohina substrate.

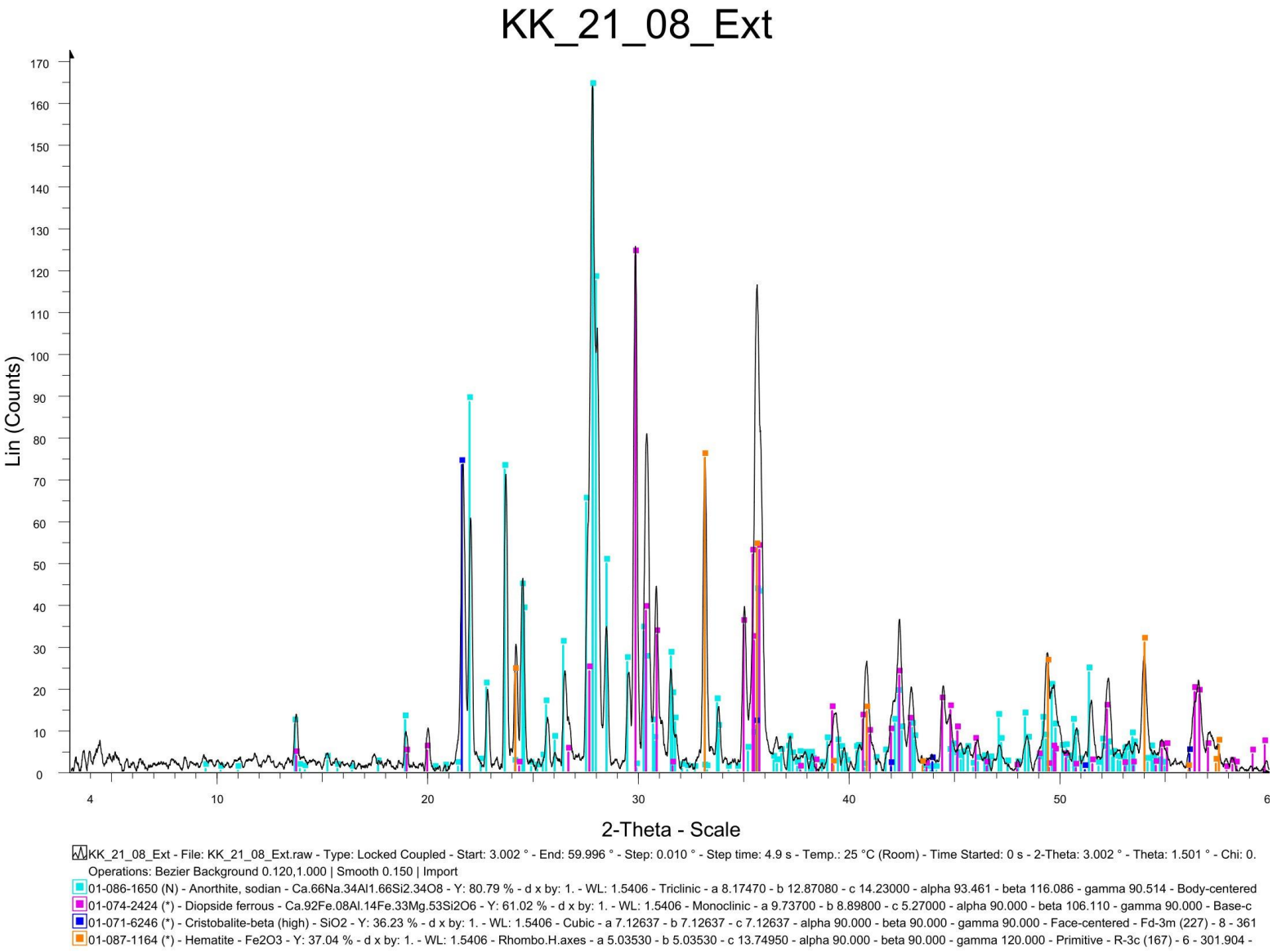

Figure 16 XRD plot for the exterior surface of KK_21_08.

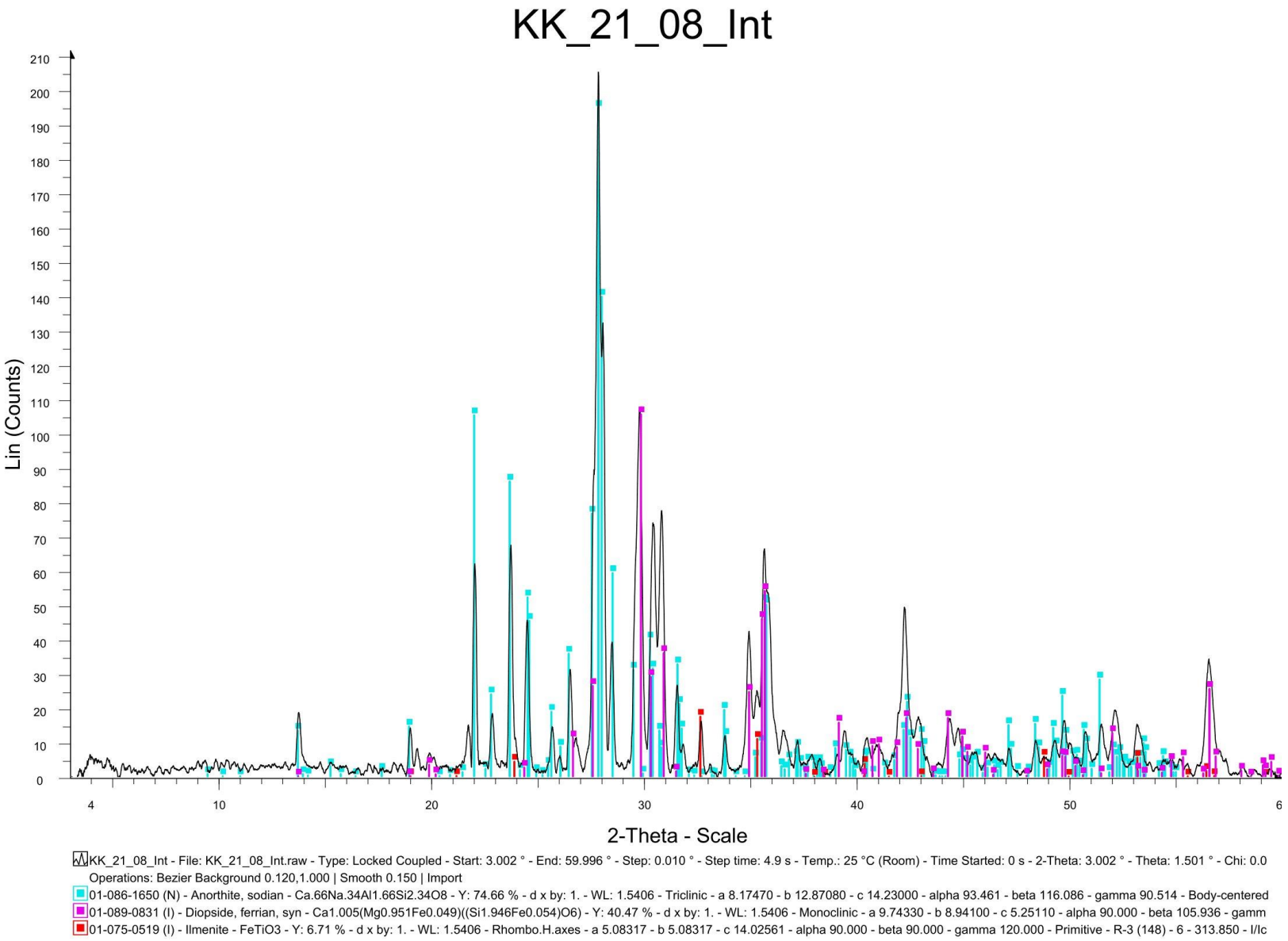

Figure 17 XRD plot for the interior of KK_21_08.

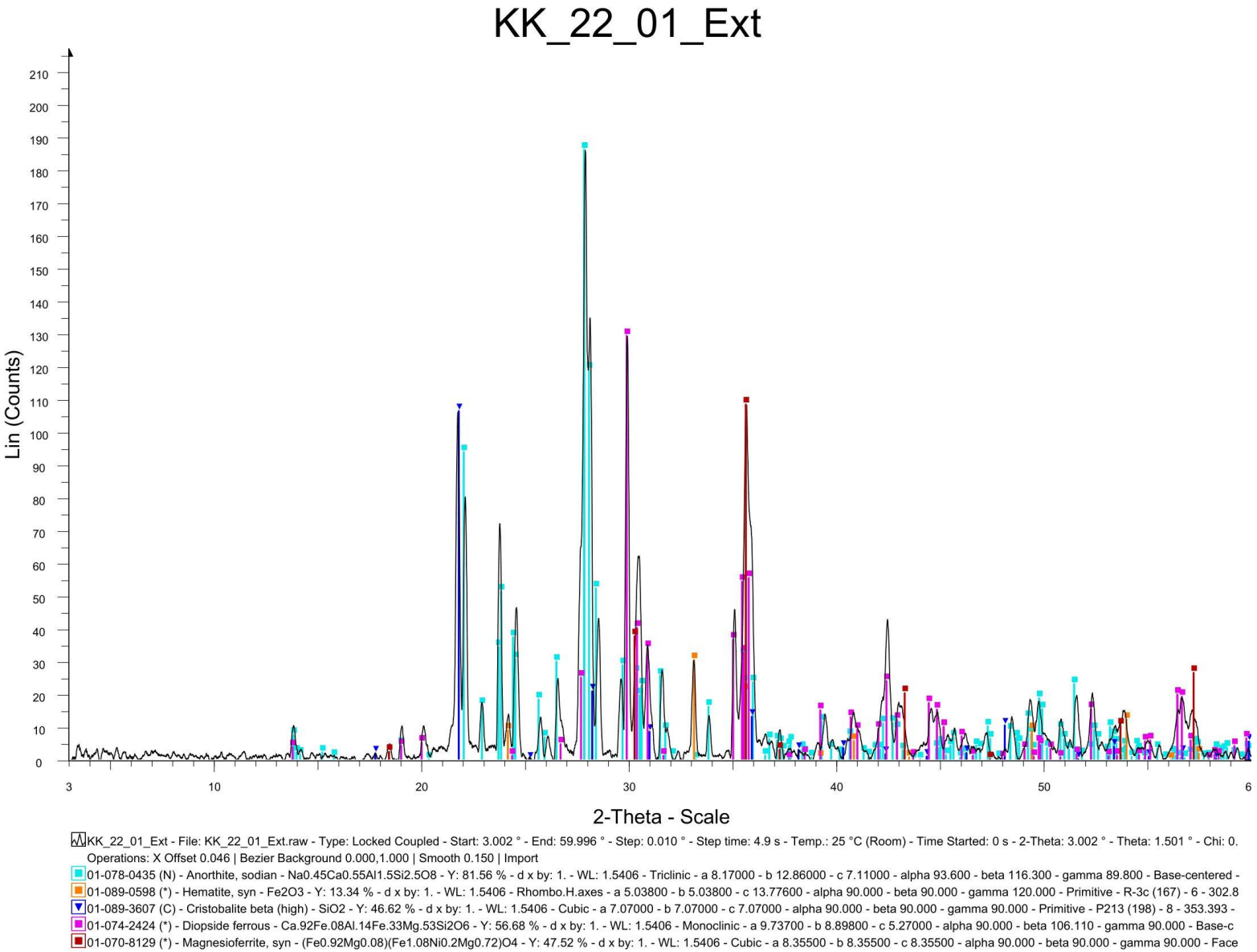

Figure 18 XRD plot for the exterior of KK_22_01.

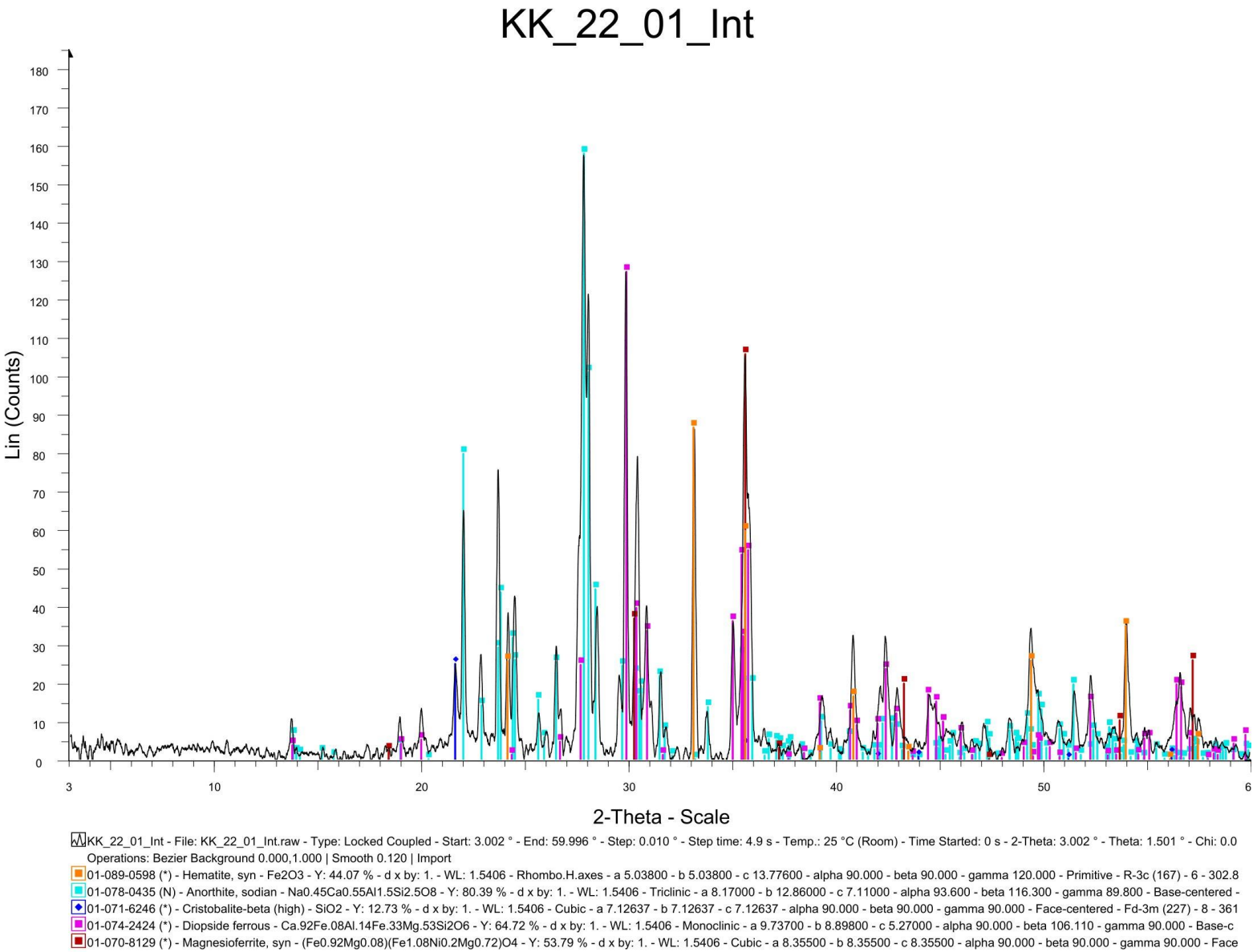

Figure 19 XRD plot for the interior of KK_22_01.

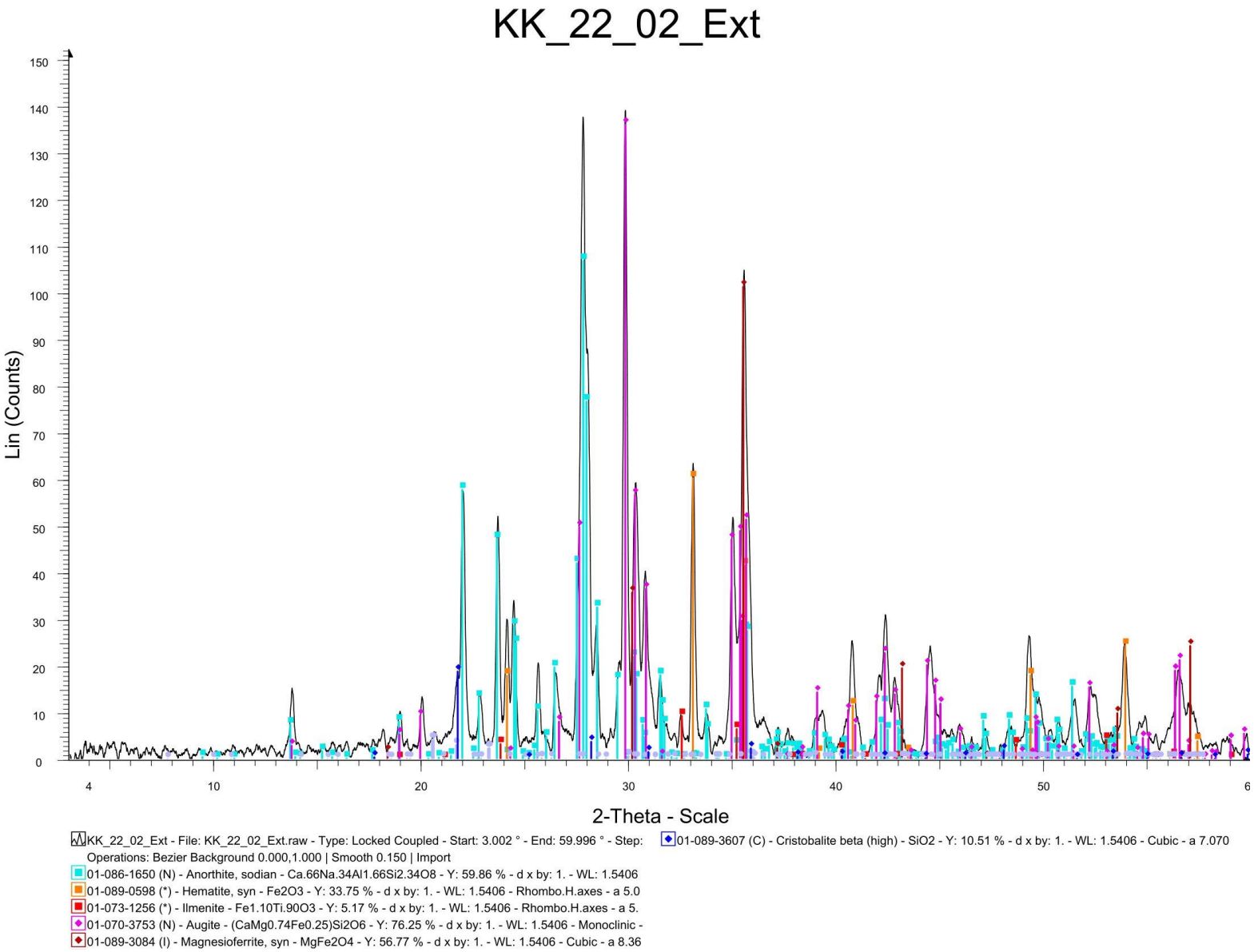

Figure 20 XRD plot for the exterior of KK_22_02.

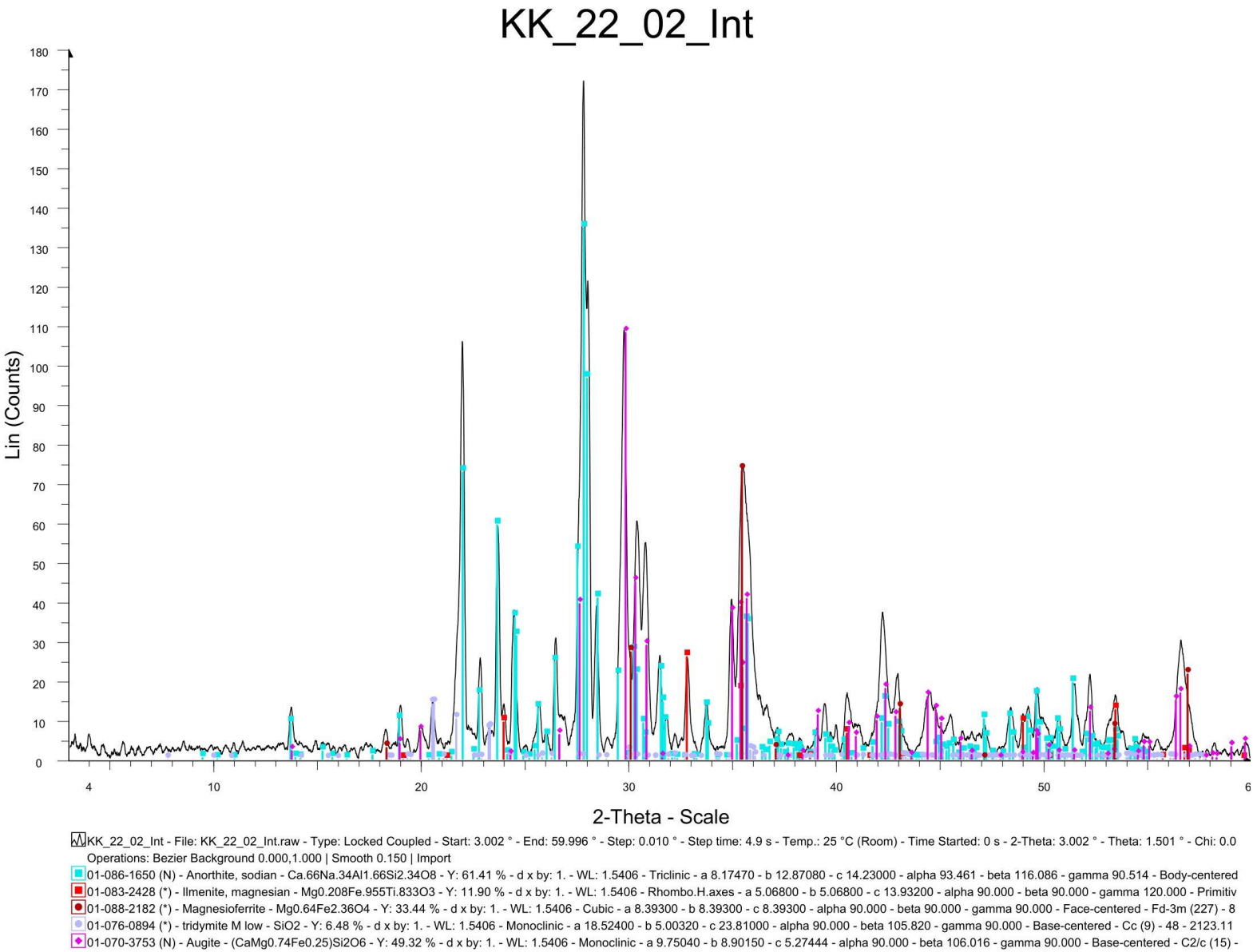

Figure 21 XRD plot for the interior of KK_22_02.

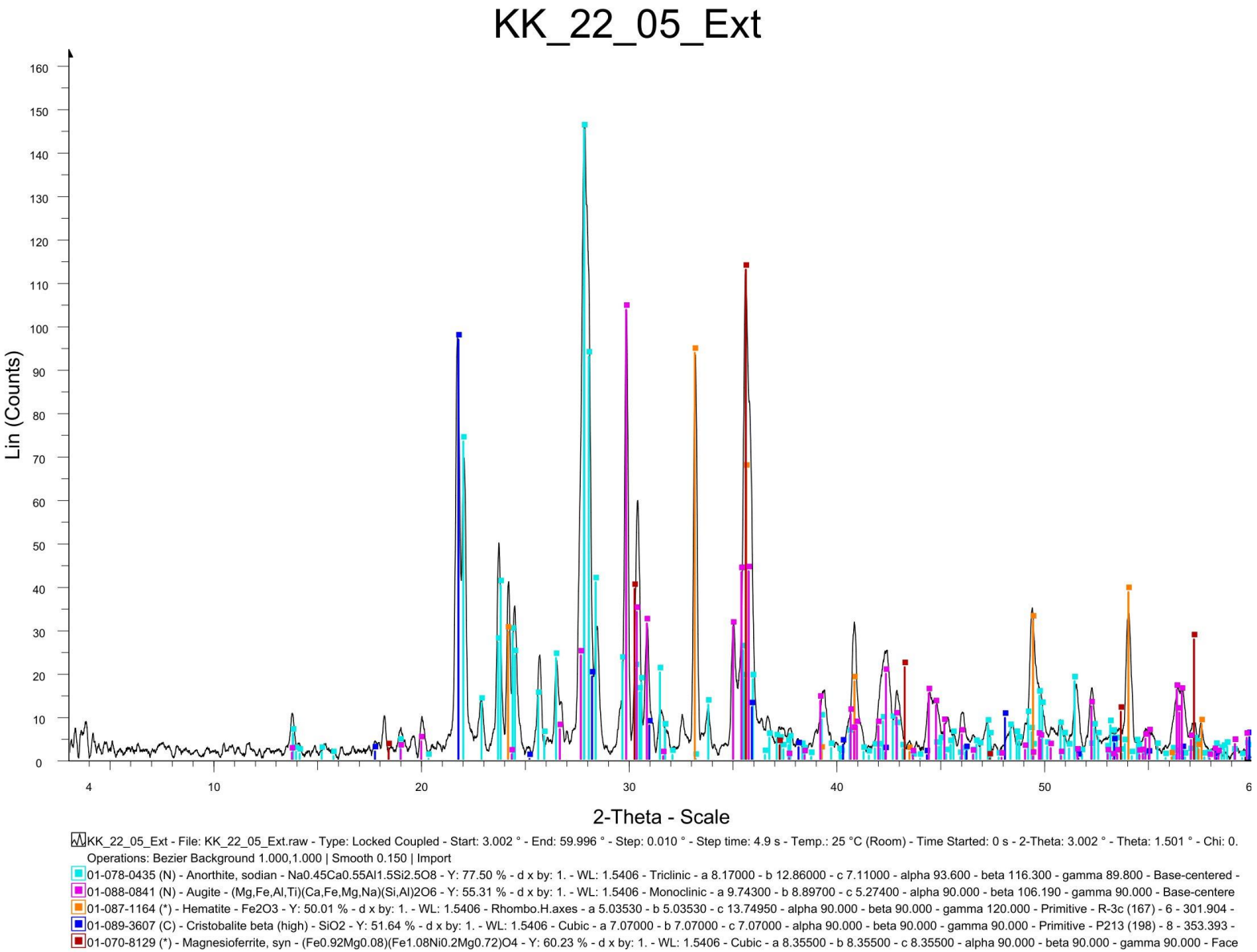

Figure 22 XRD plot for the exterior of KK_22_05.

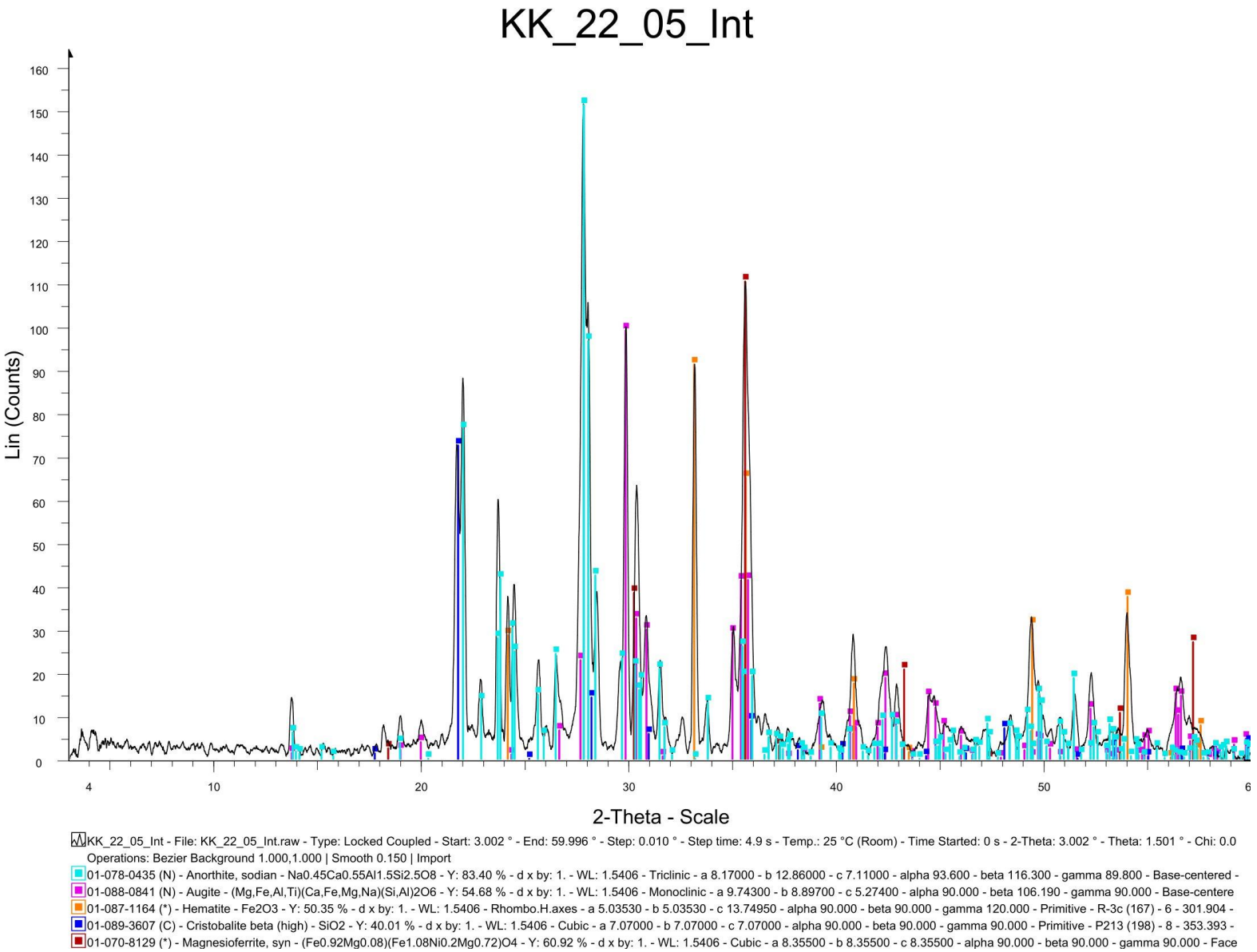

Figure 23 XRD plot for the interior of KK_22_05.

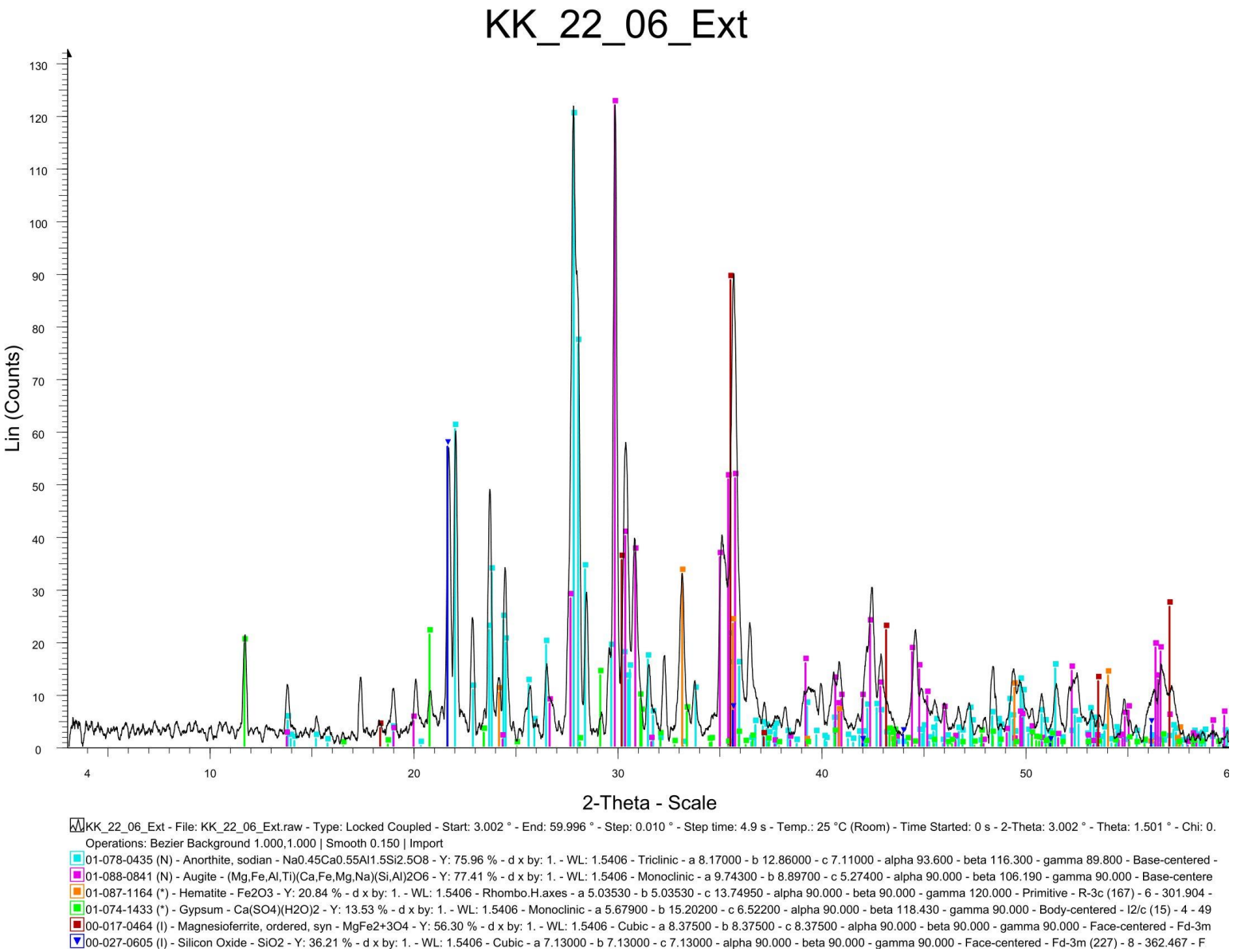

Figure 24 XRD plot for the exterior of KK_22_06.

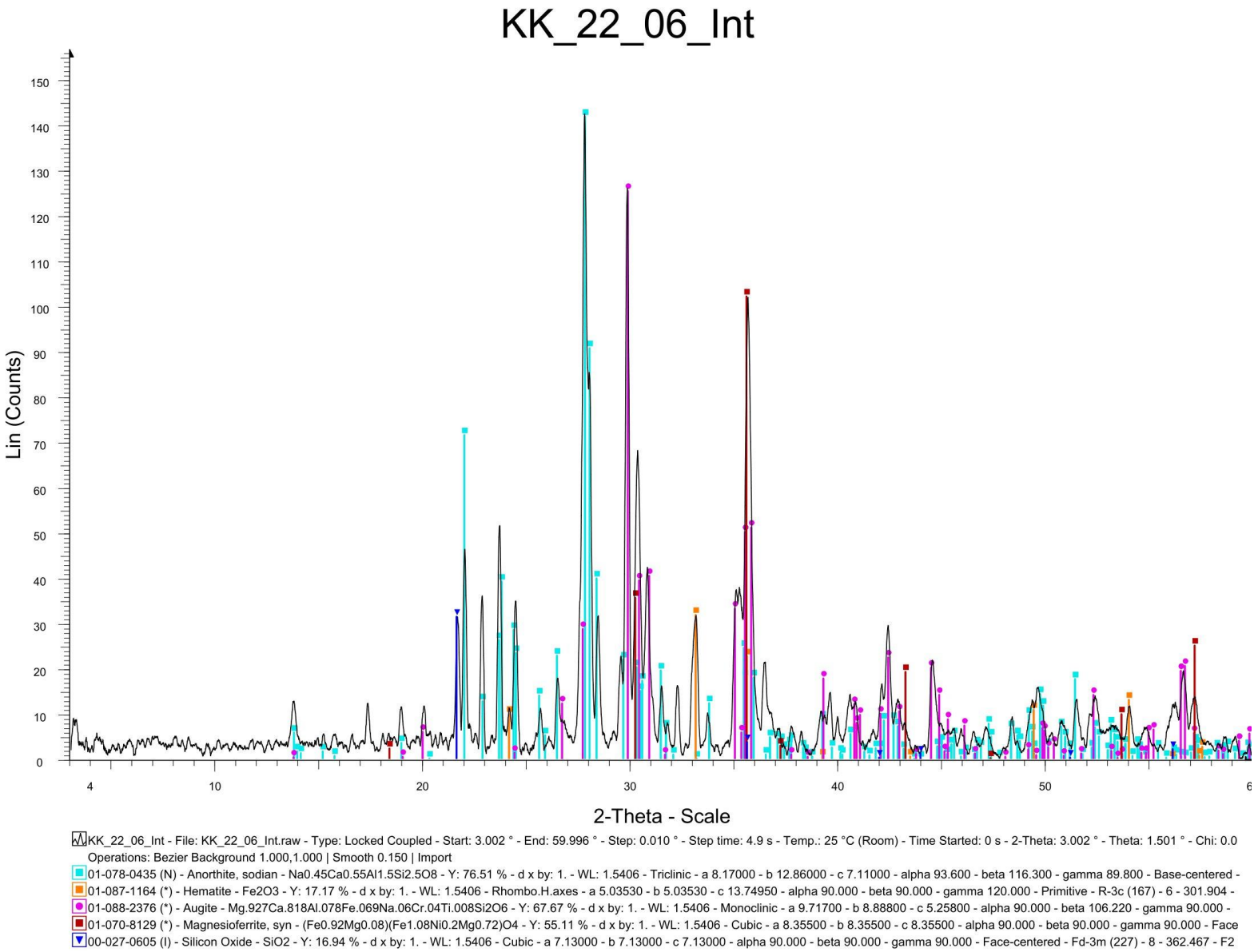

Figure 25 XRD plot for the interior of KK_22_06.

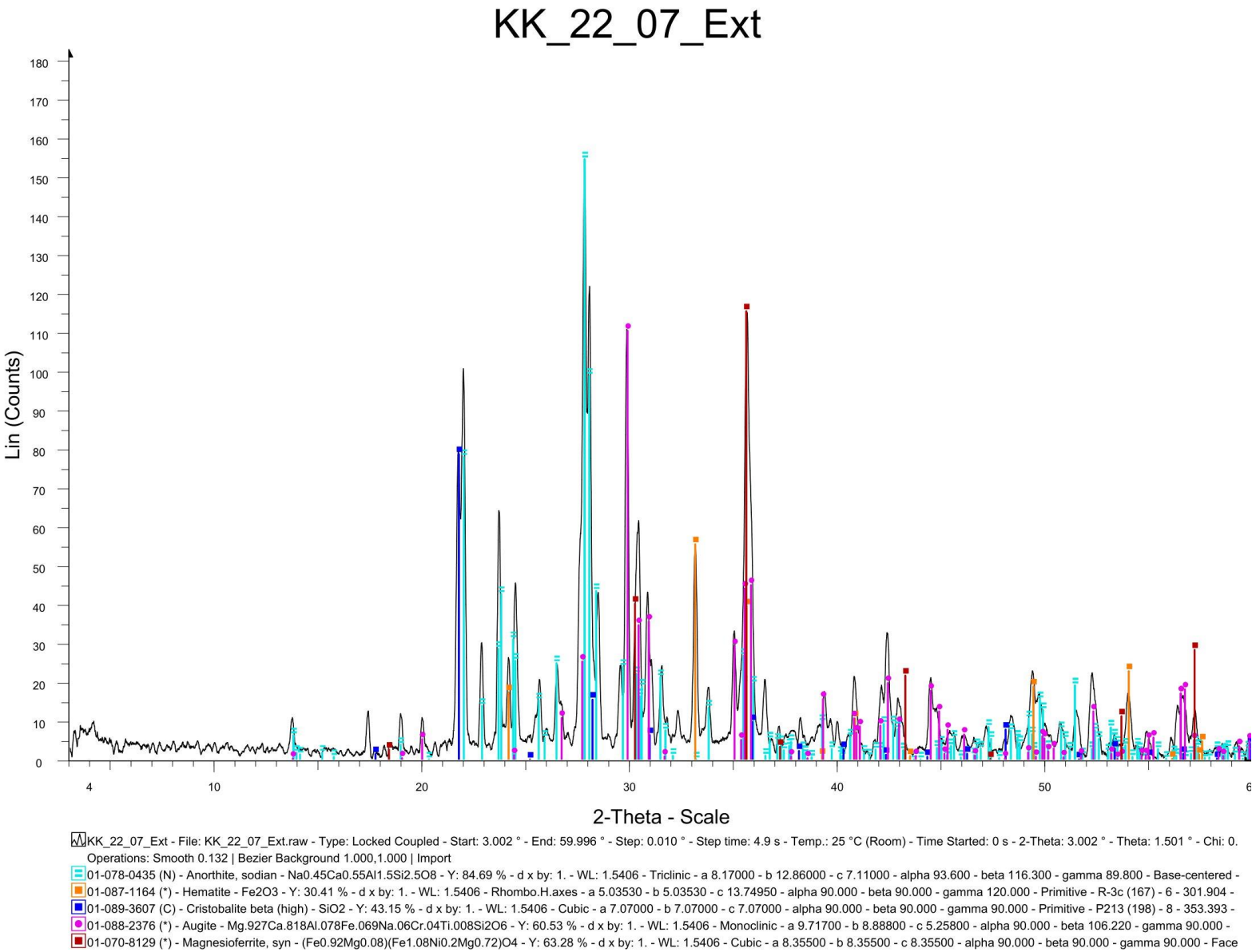

Figure 26 XRD plot for the exterior of KK_22_07.

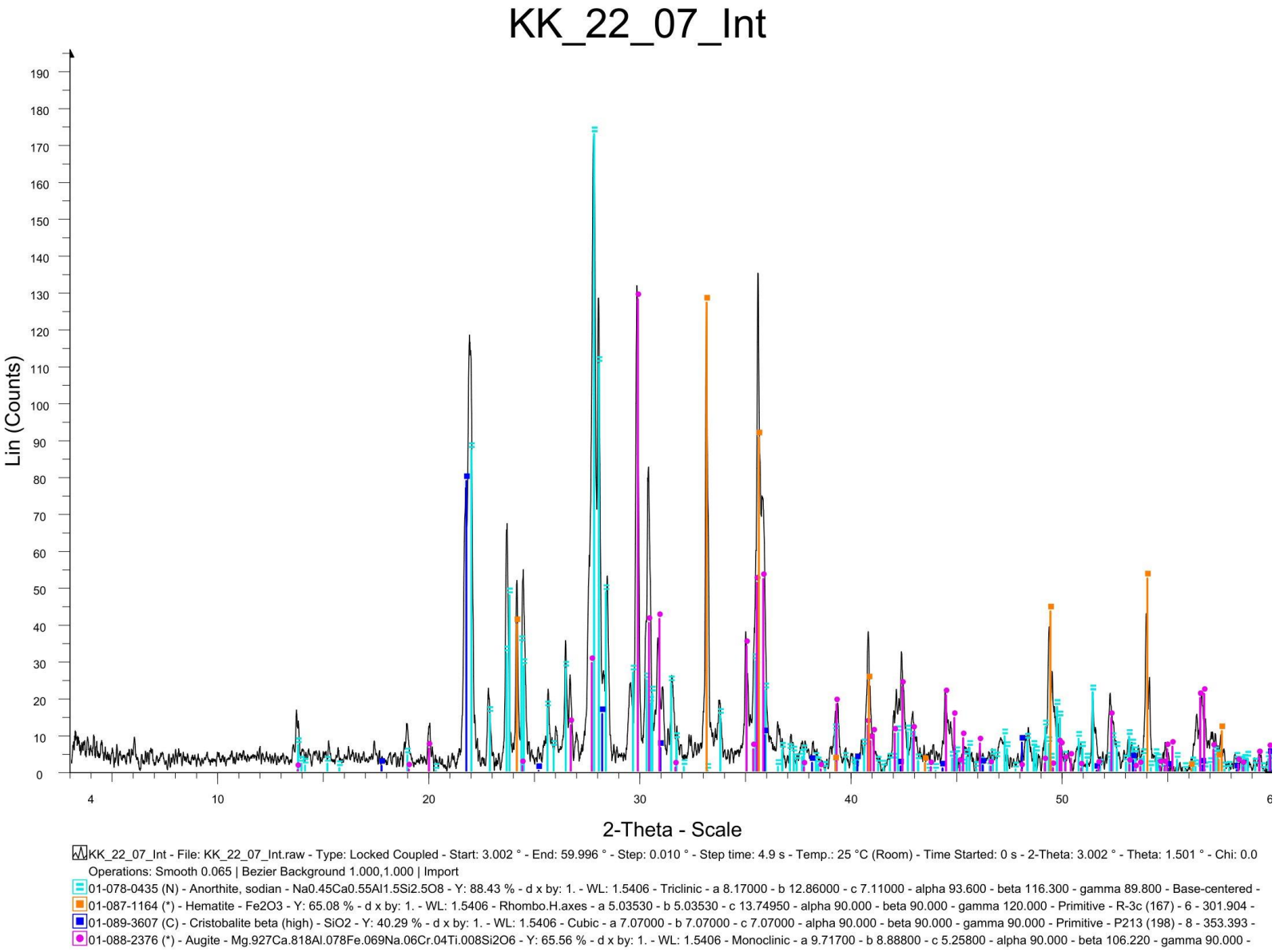

Figure 27 XRD plot for the interior of KK_22_07.

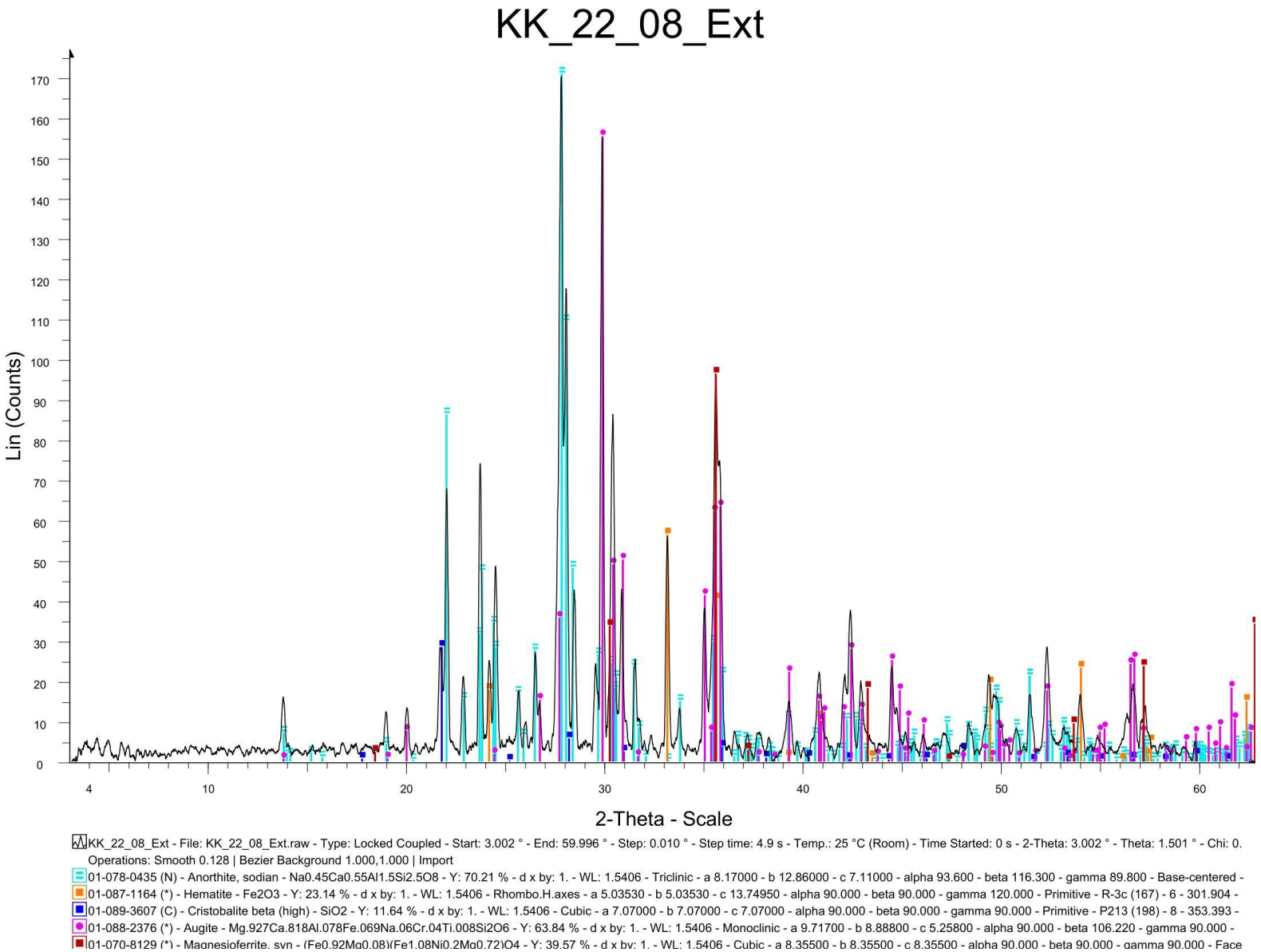

Figure 28 XRD plot for the exterior of KK_22_08.

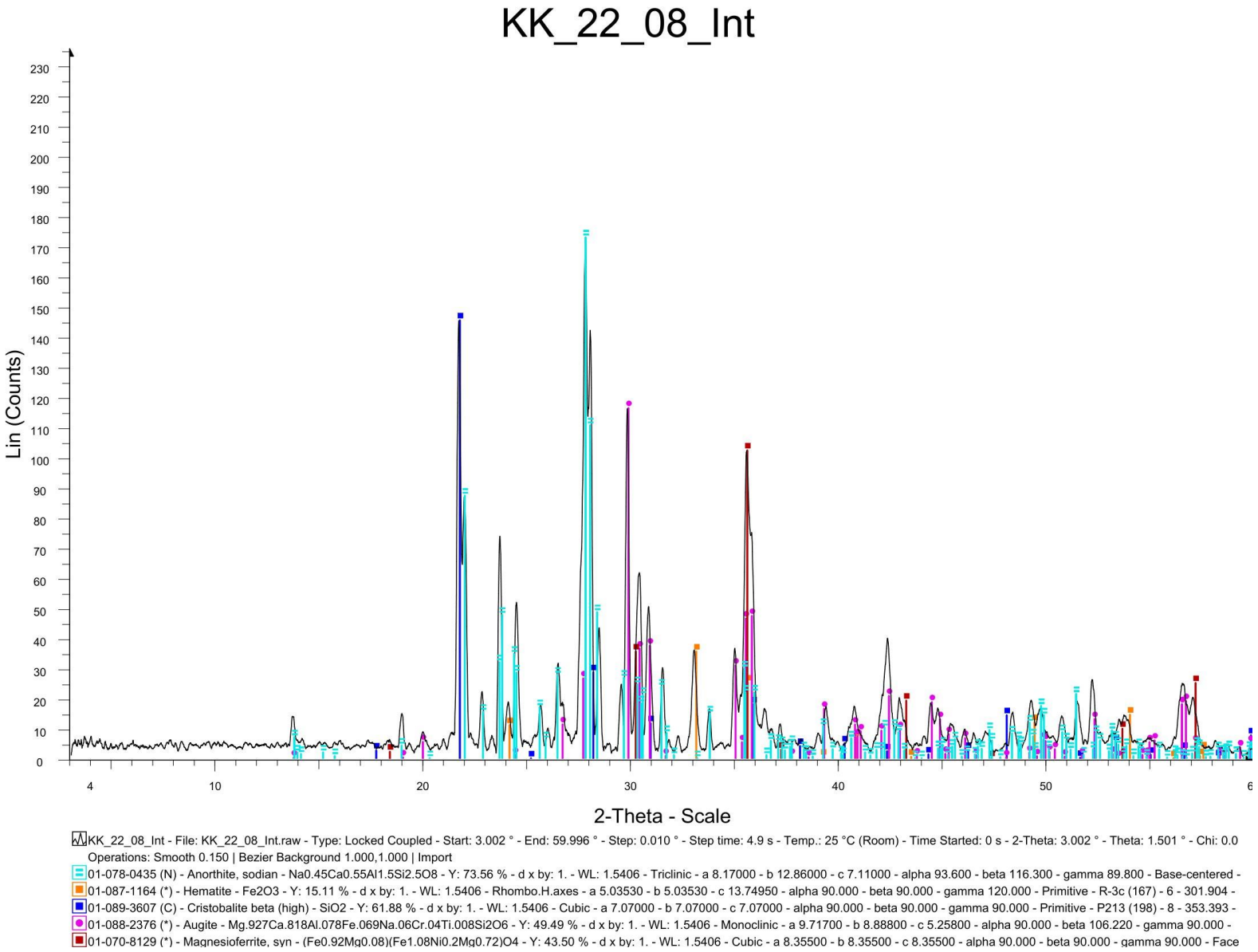

Figure 29 XRD plot for the interior of KK_22_08.

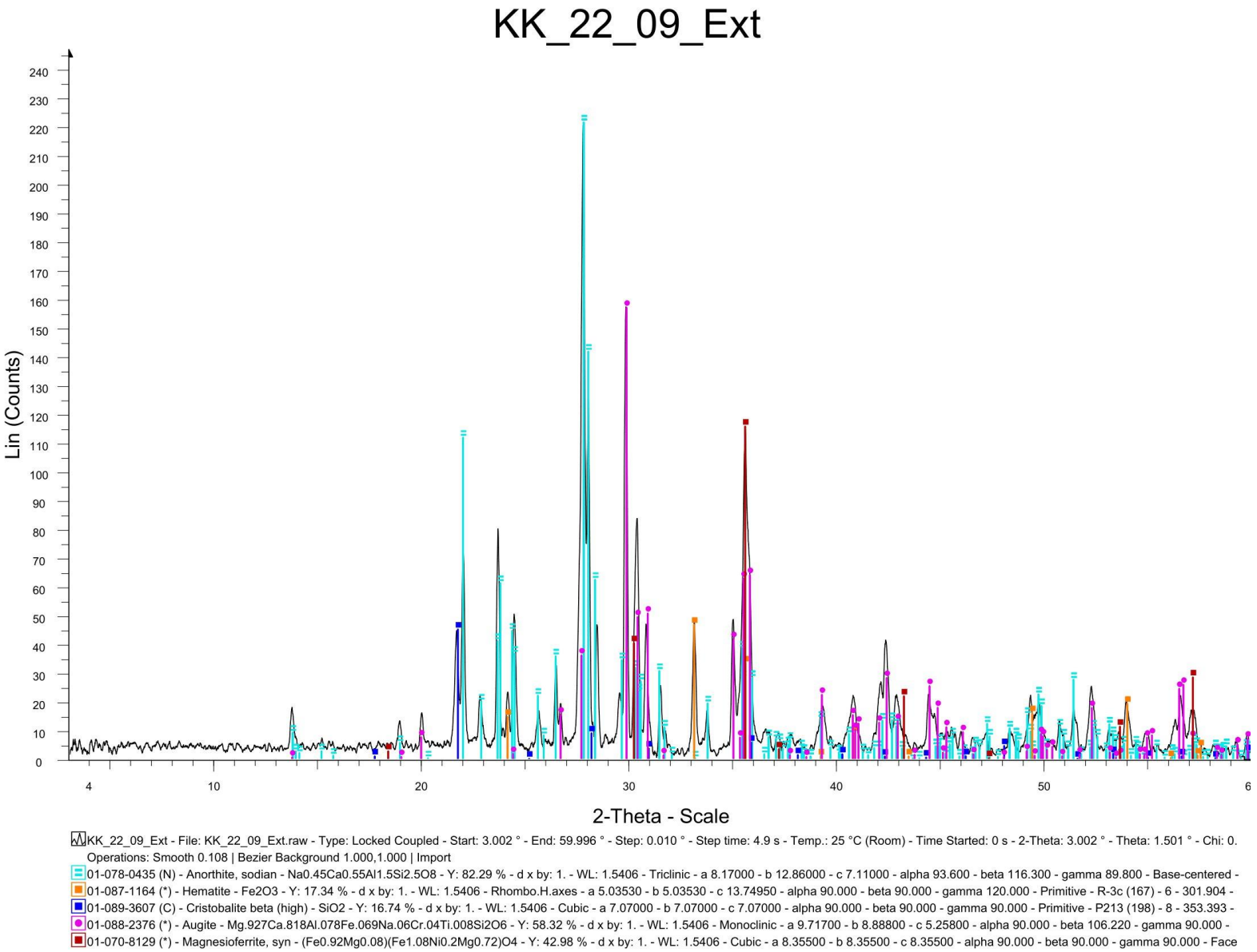

Figure 30 XRD plot for the exterior of KK_22_09.

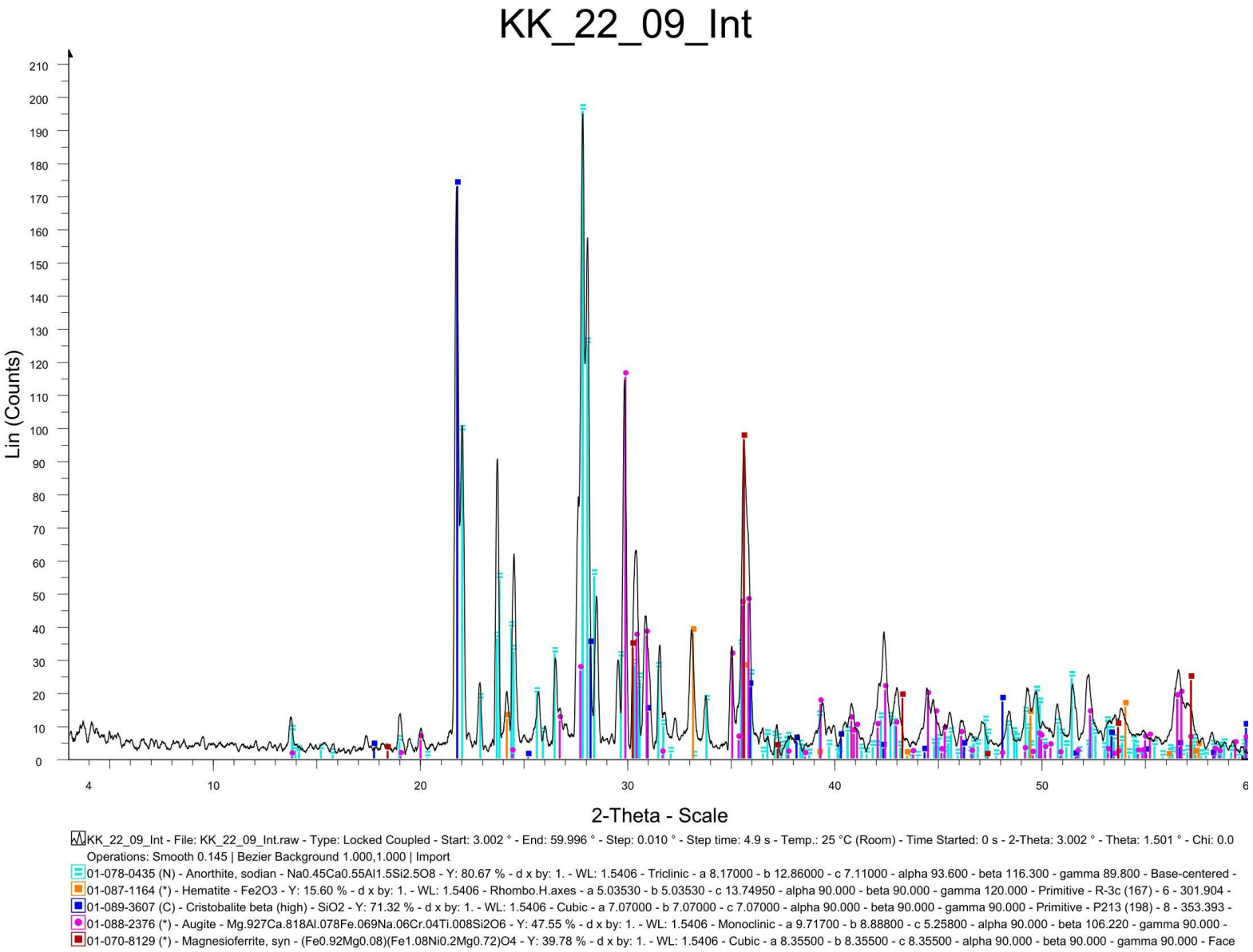

Figure 31 XRD plot for the interior of KK_22_09.

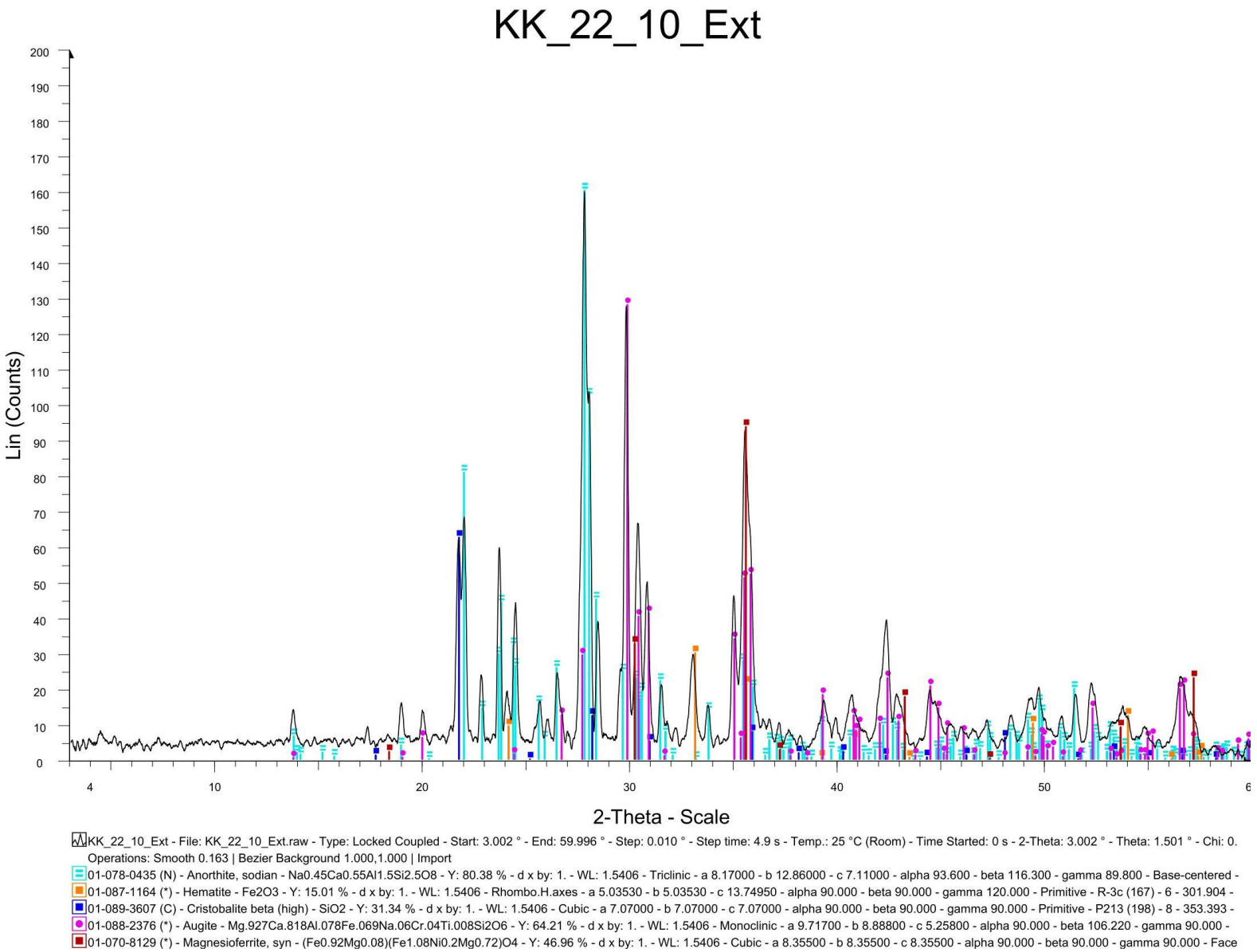

Figure 32 XRD plot for the exterior of KK_22_10.

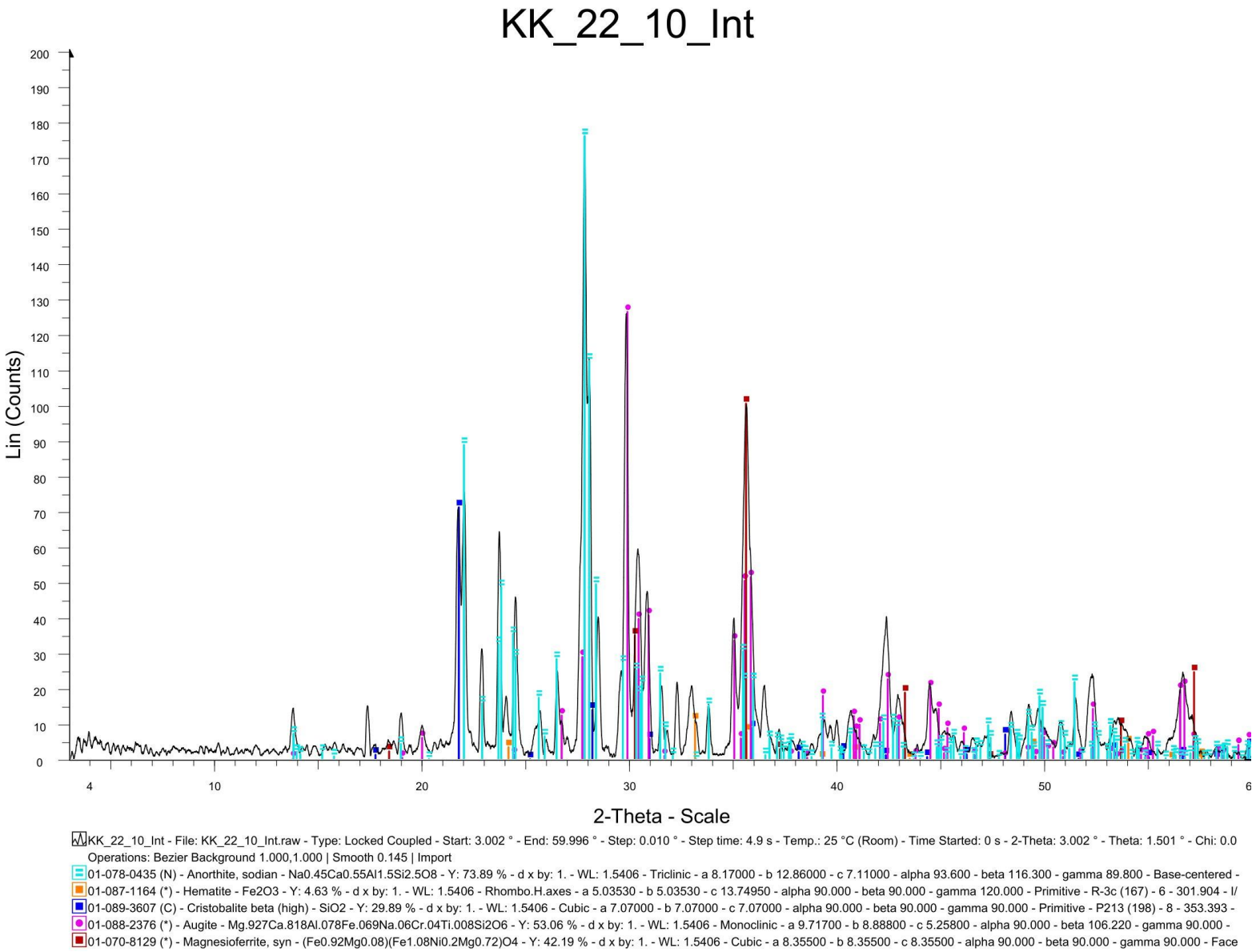

Figure 33 XRD plot for the interior of KK_22_10.

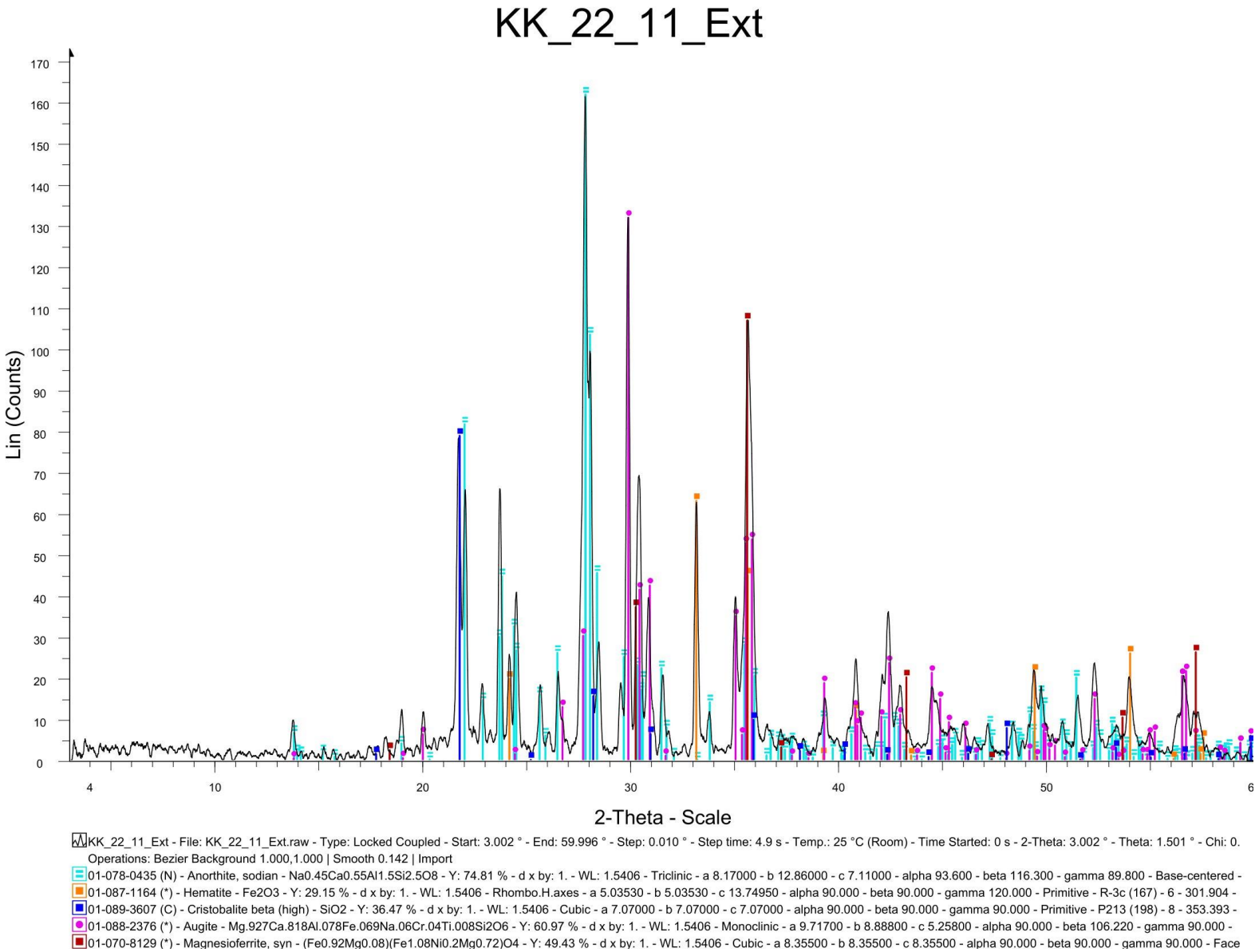

Figure 34 XRD plot for the exterior of KK_22_11.

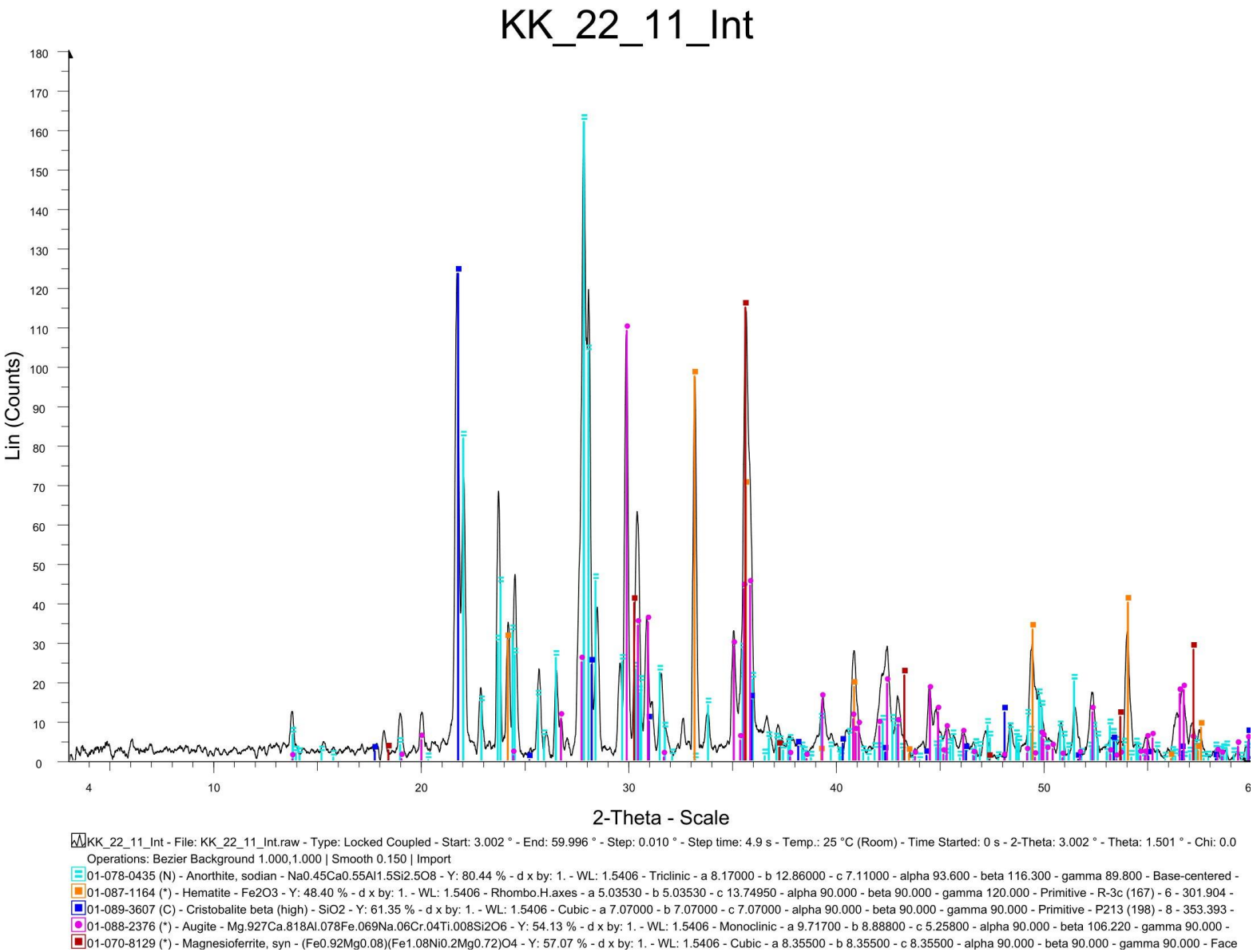

Figure 35 XRD plot for the interior of KK_22_11.

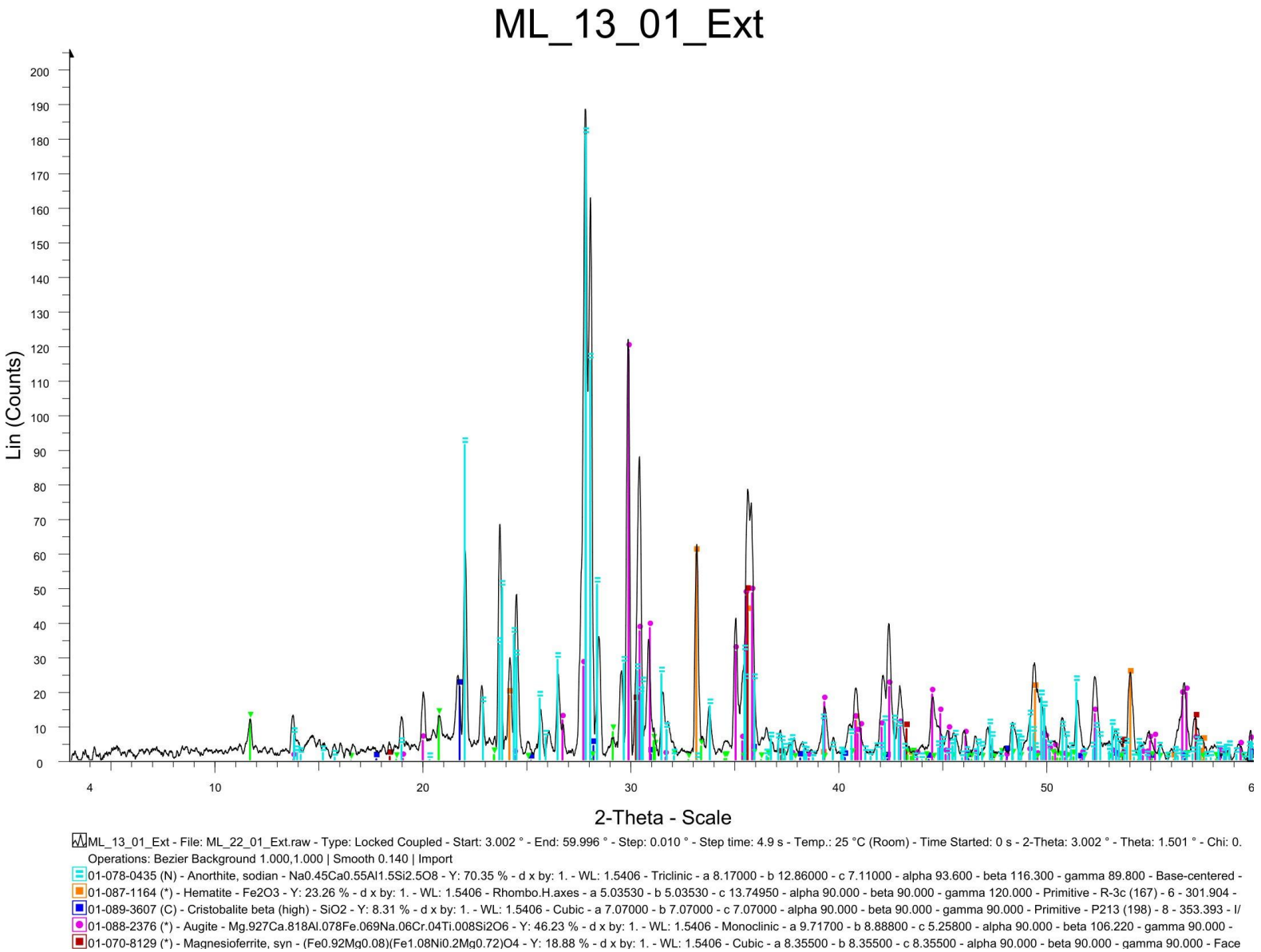

Figure 36 XRD plot for the exterior of ML_13_01.

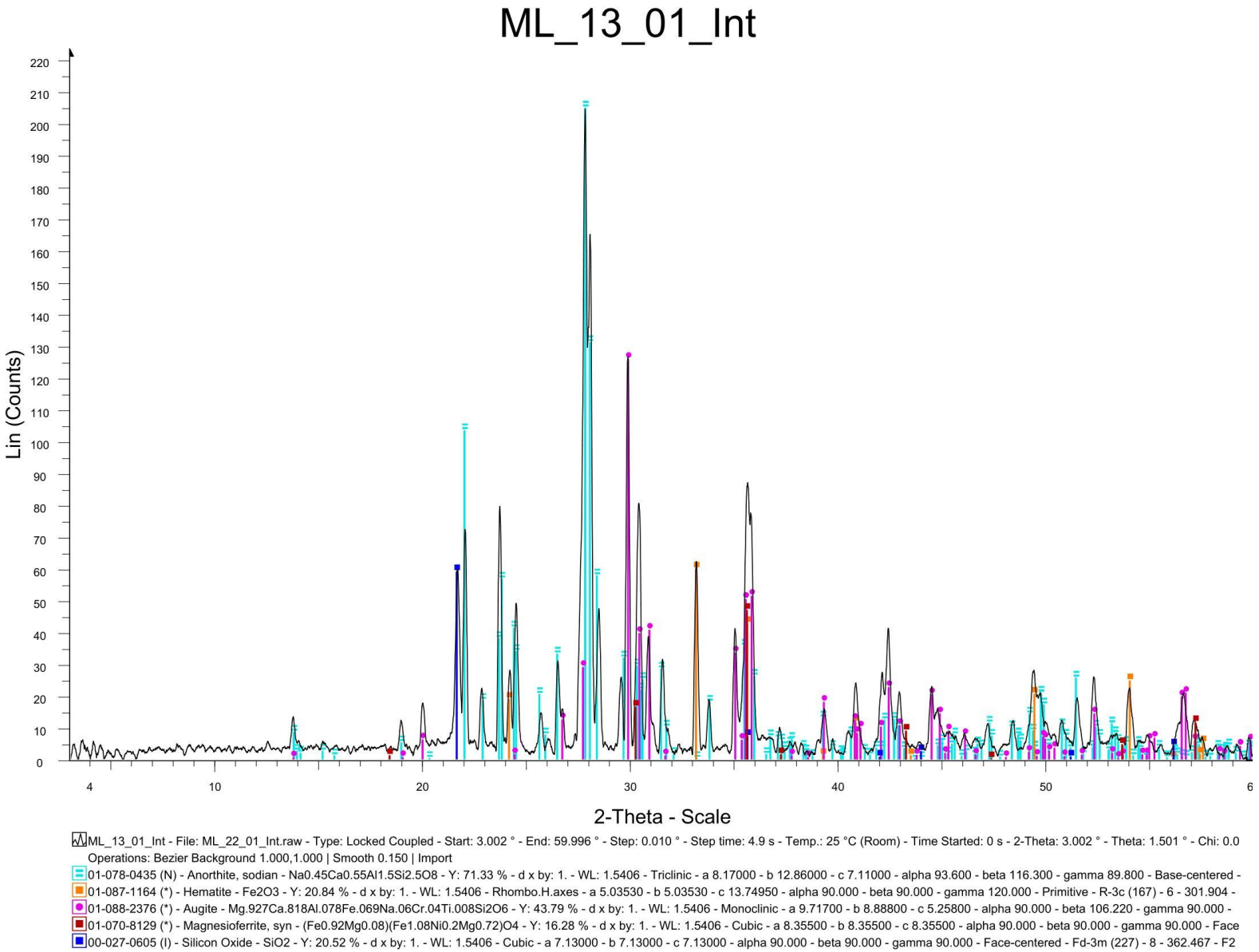

Figure 37 XRD plot for the interior of ML_13_01.

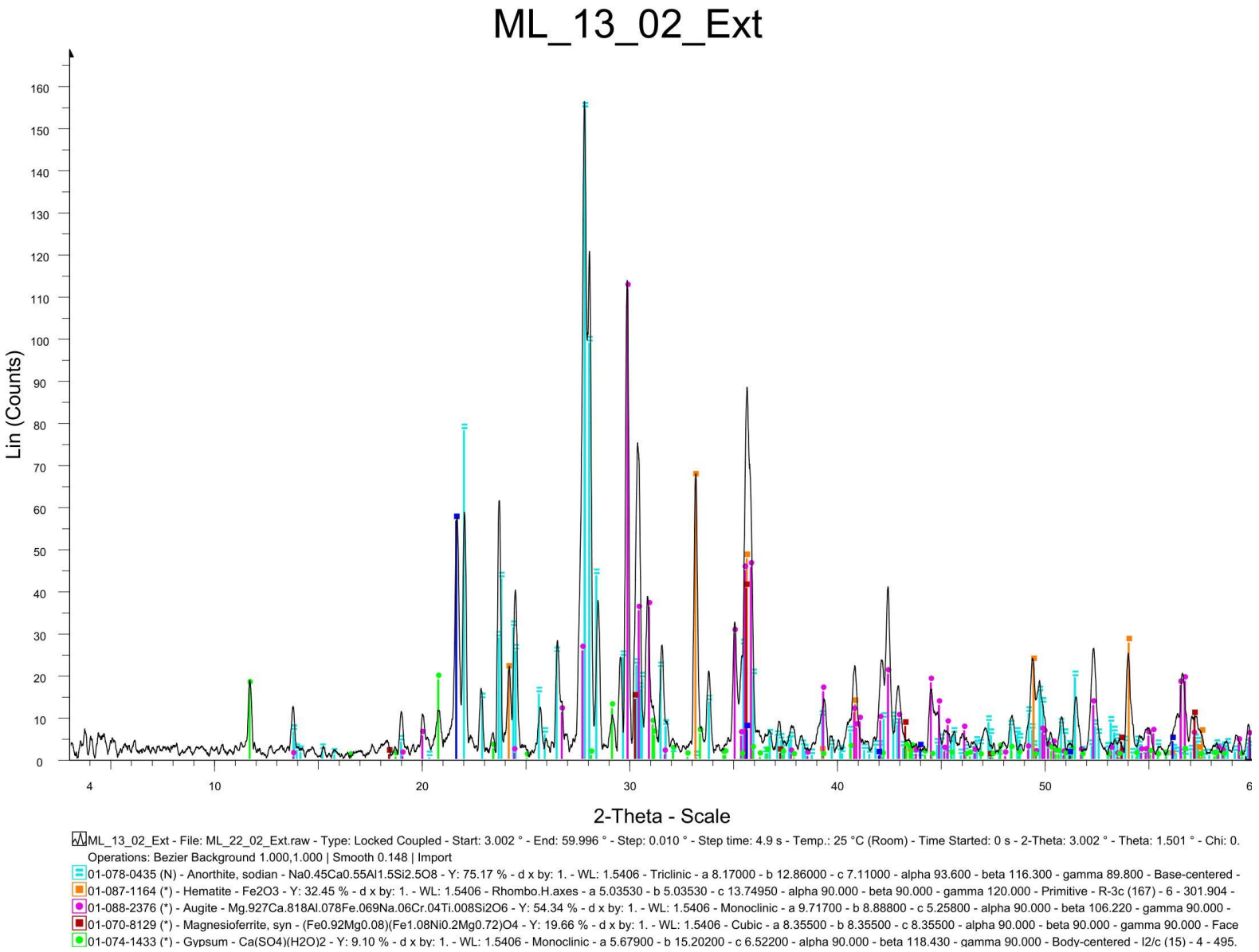

Figure 38 XRD plot for the exterior of ML_13_02.

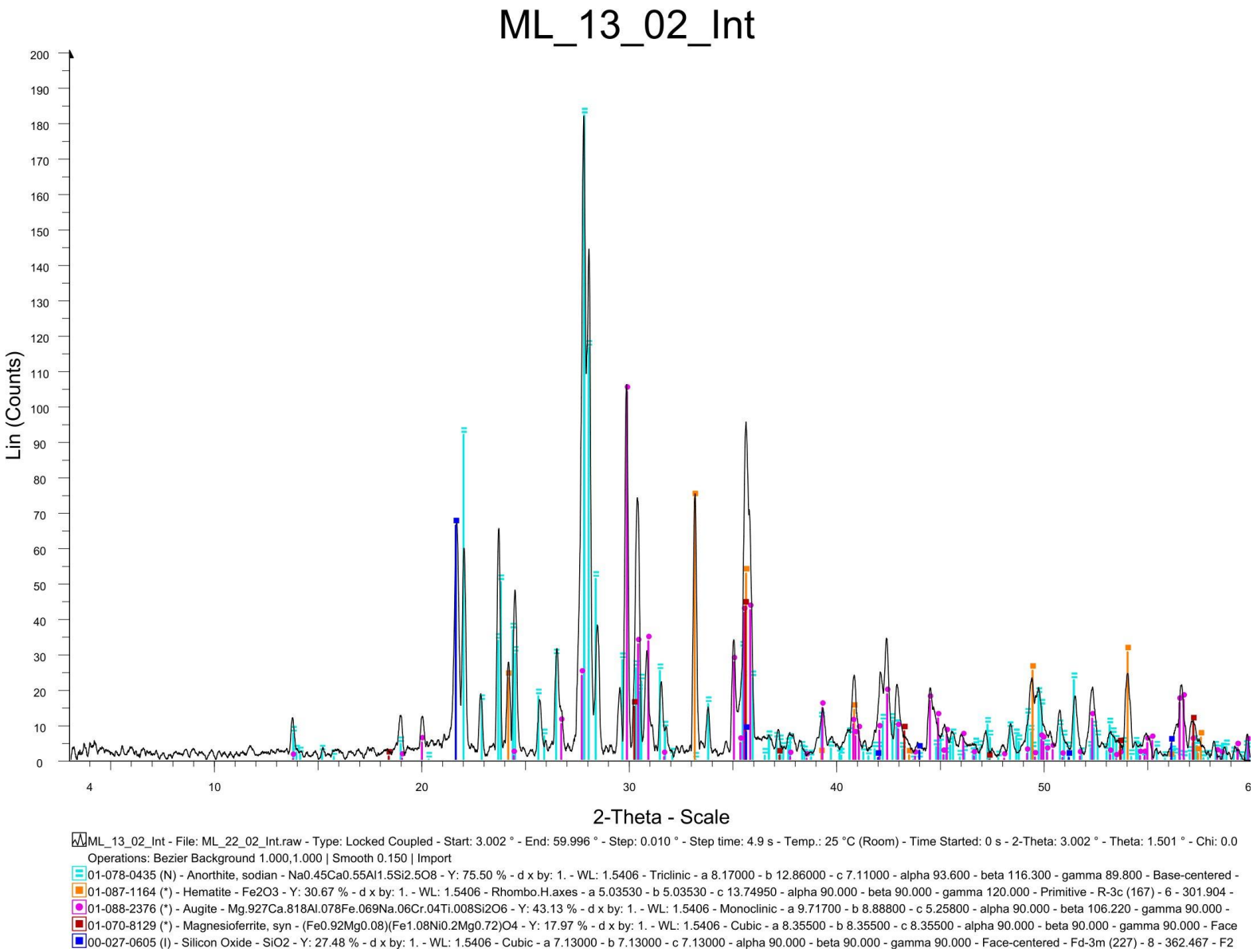

Figure 39 XRD plot for the interior of ML_13_02.

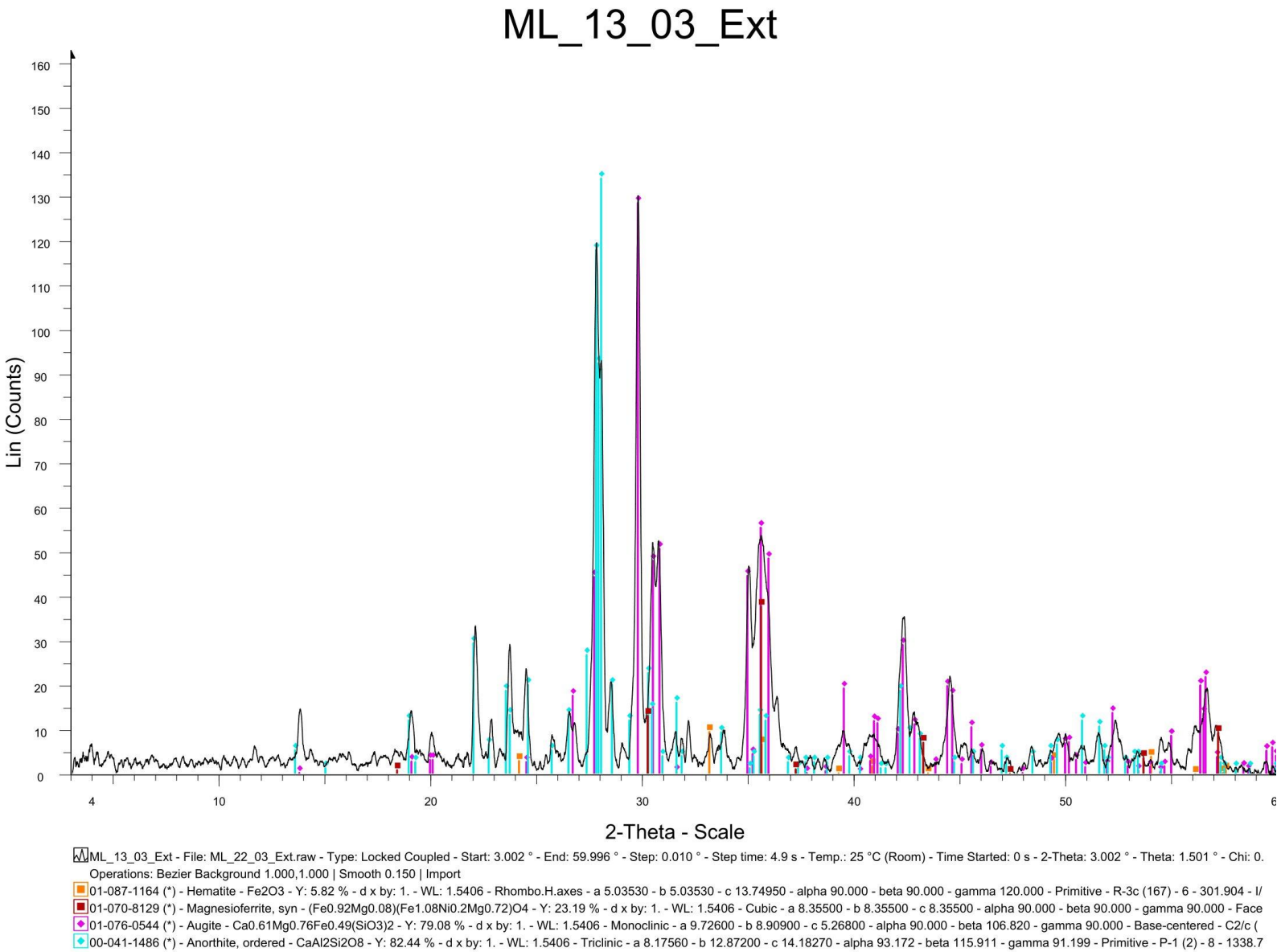

Figure 40 XRD plot for the exterior of ML_13_03.

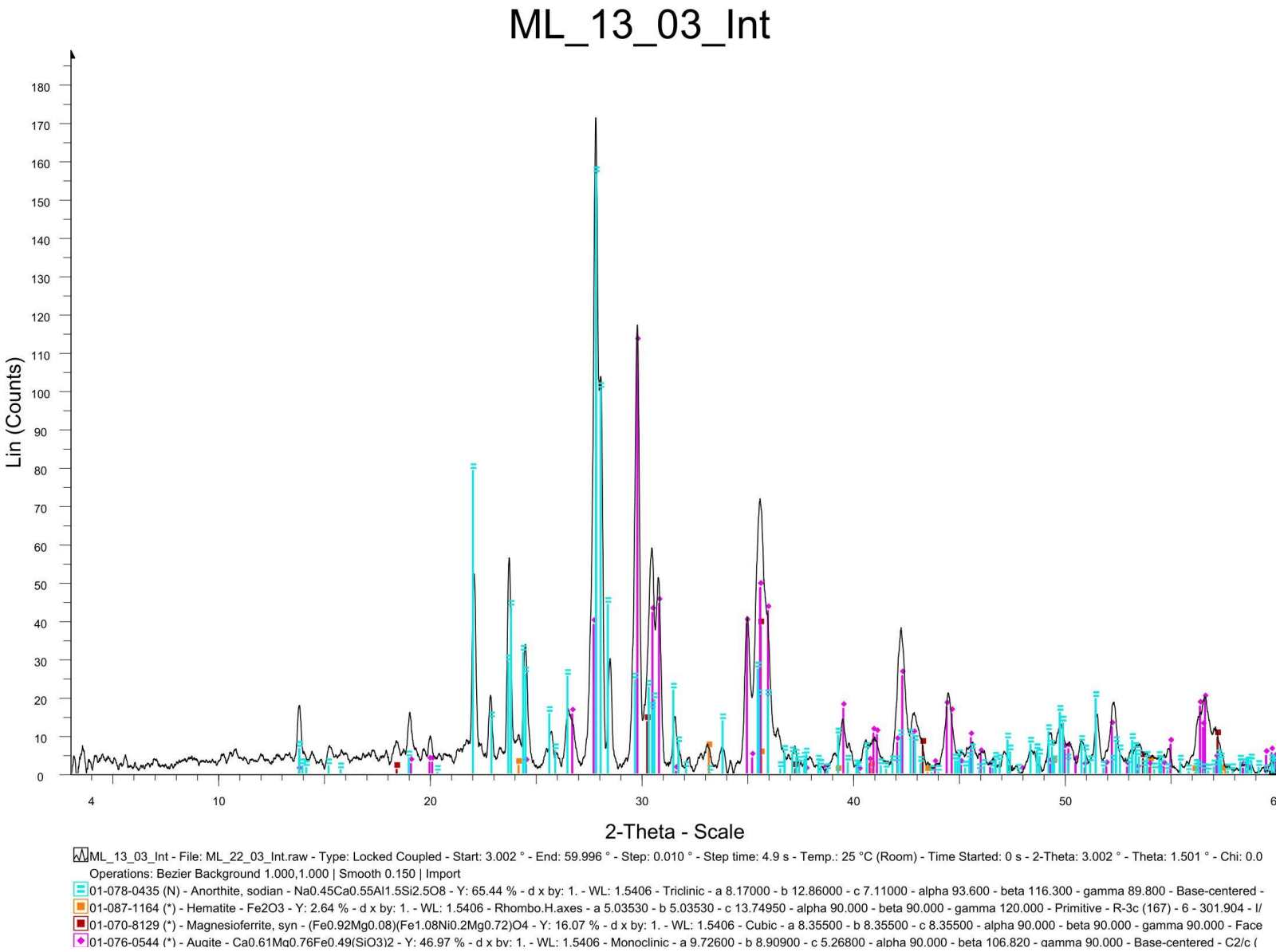

Figure 41 XRD plot for the interior of ML_13_03.

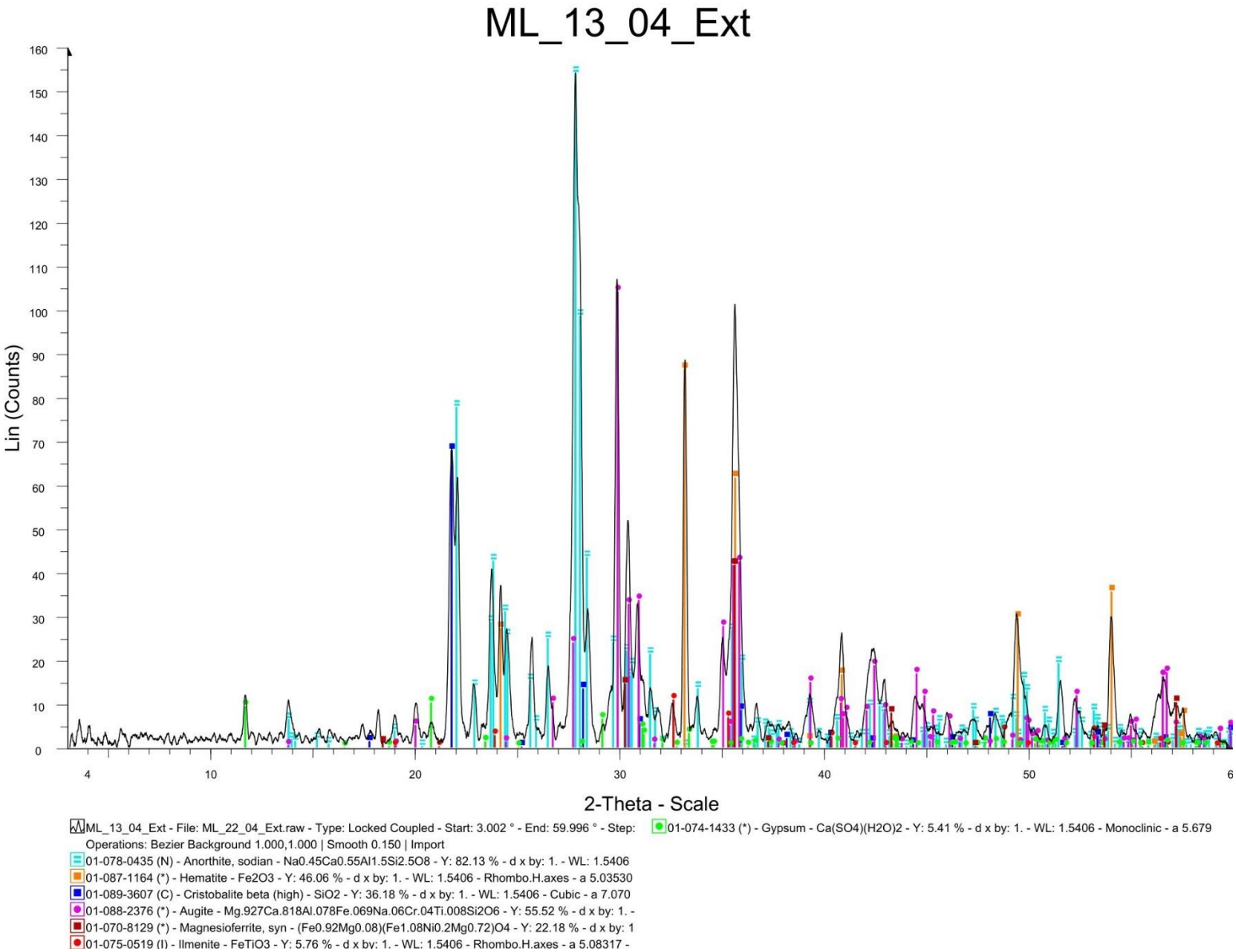

Figure 42 XRD plot for the exterior of ML_13_04.

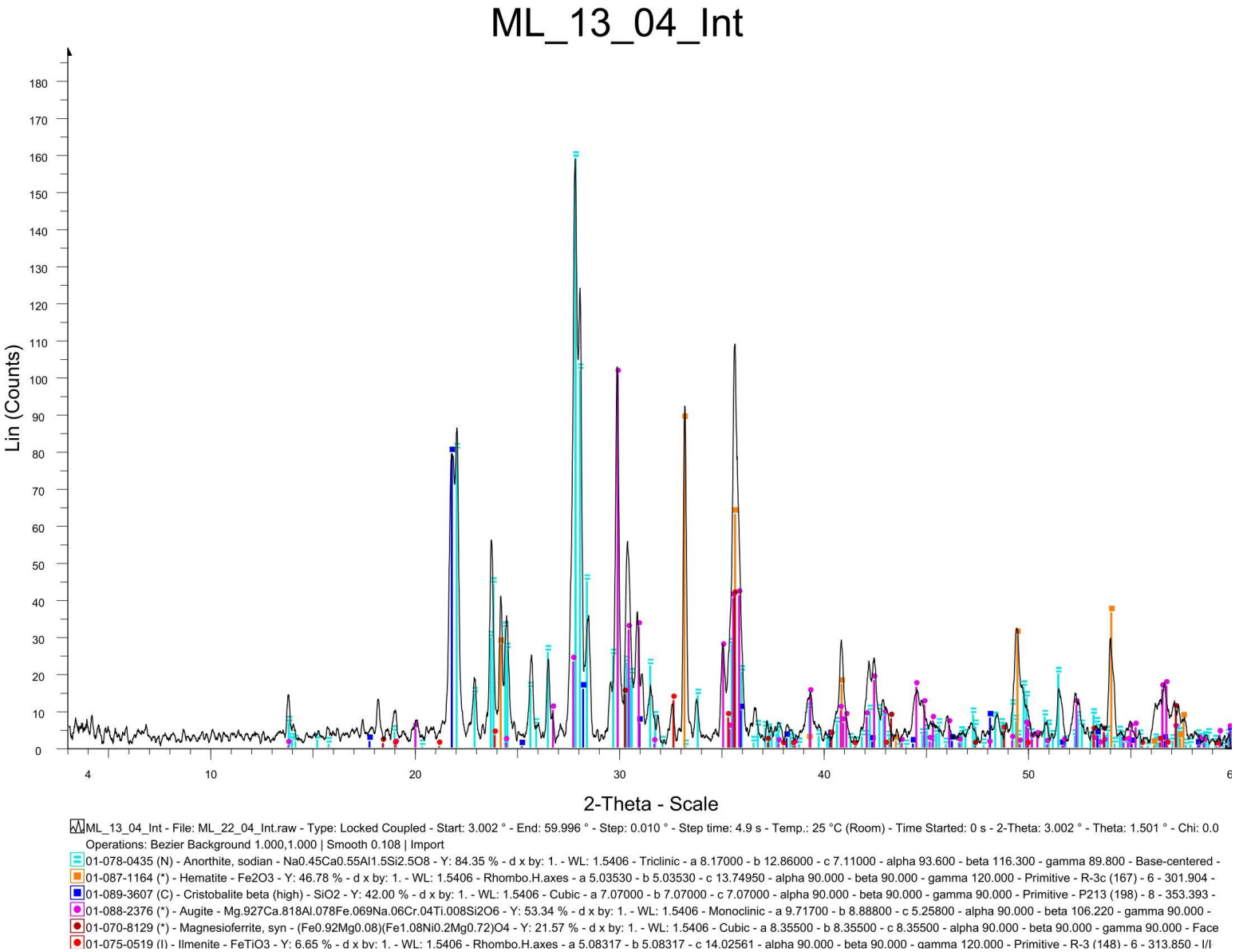

Figure 43 XRD plot for the interior of ML_13_04.

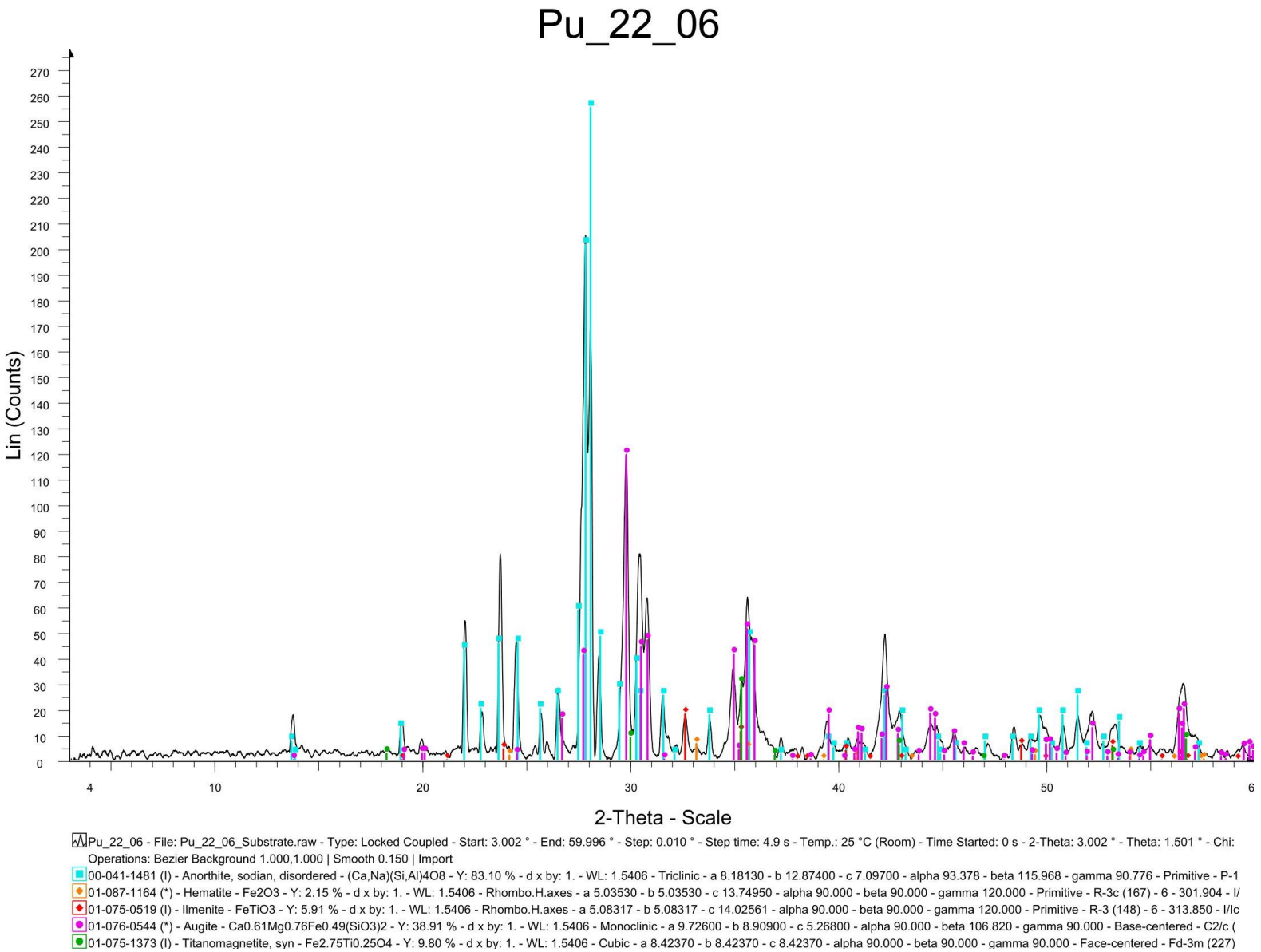

Figure 44 XRD plot for sample substrate PU_22_06.

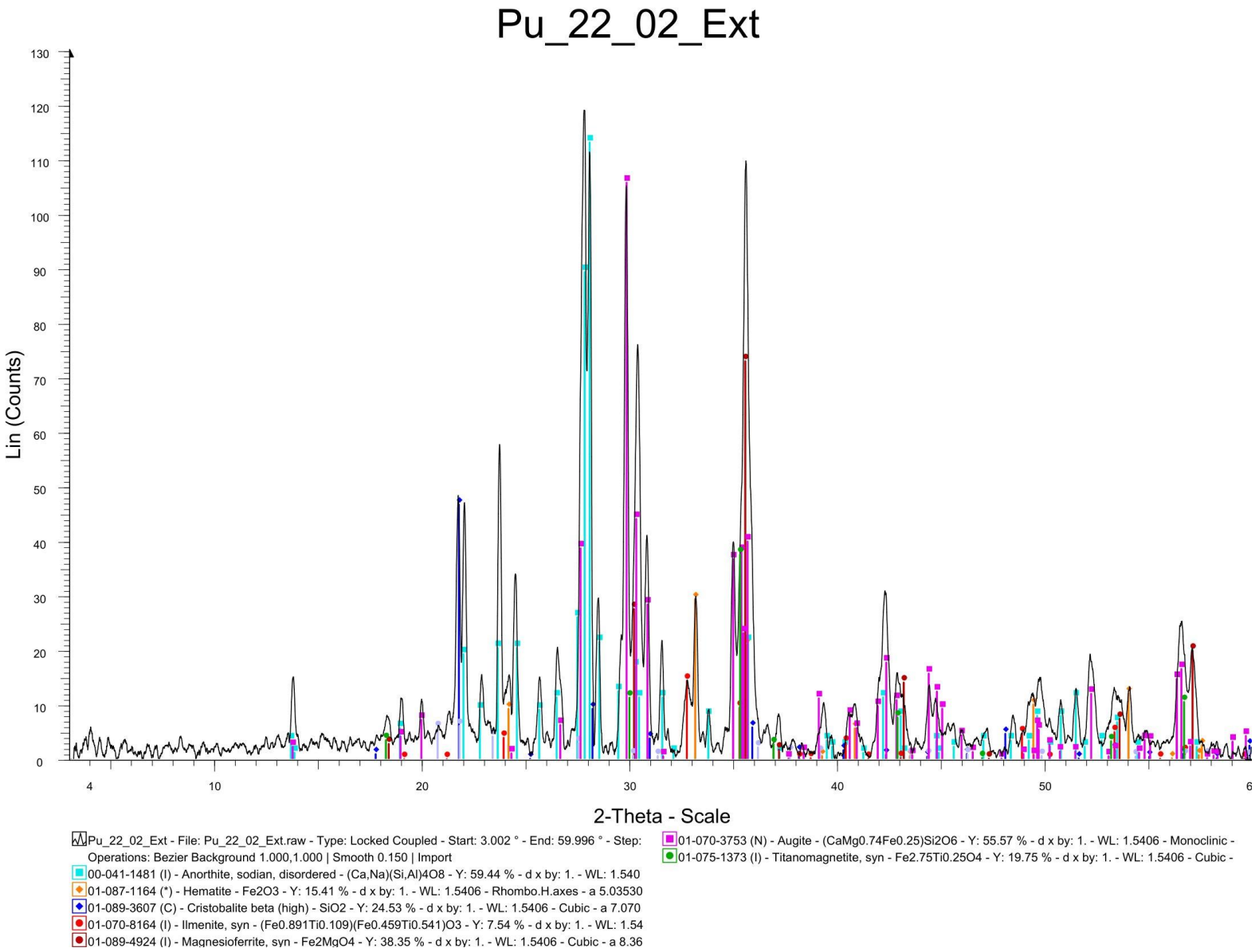

Figure 45 XRD plot for the exterior of PU_22_02.

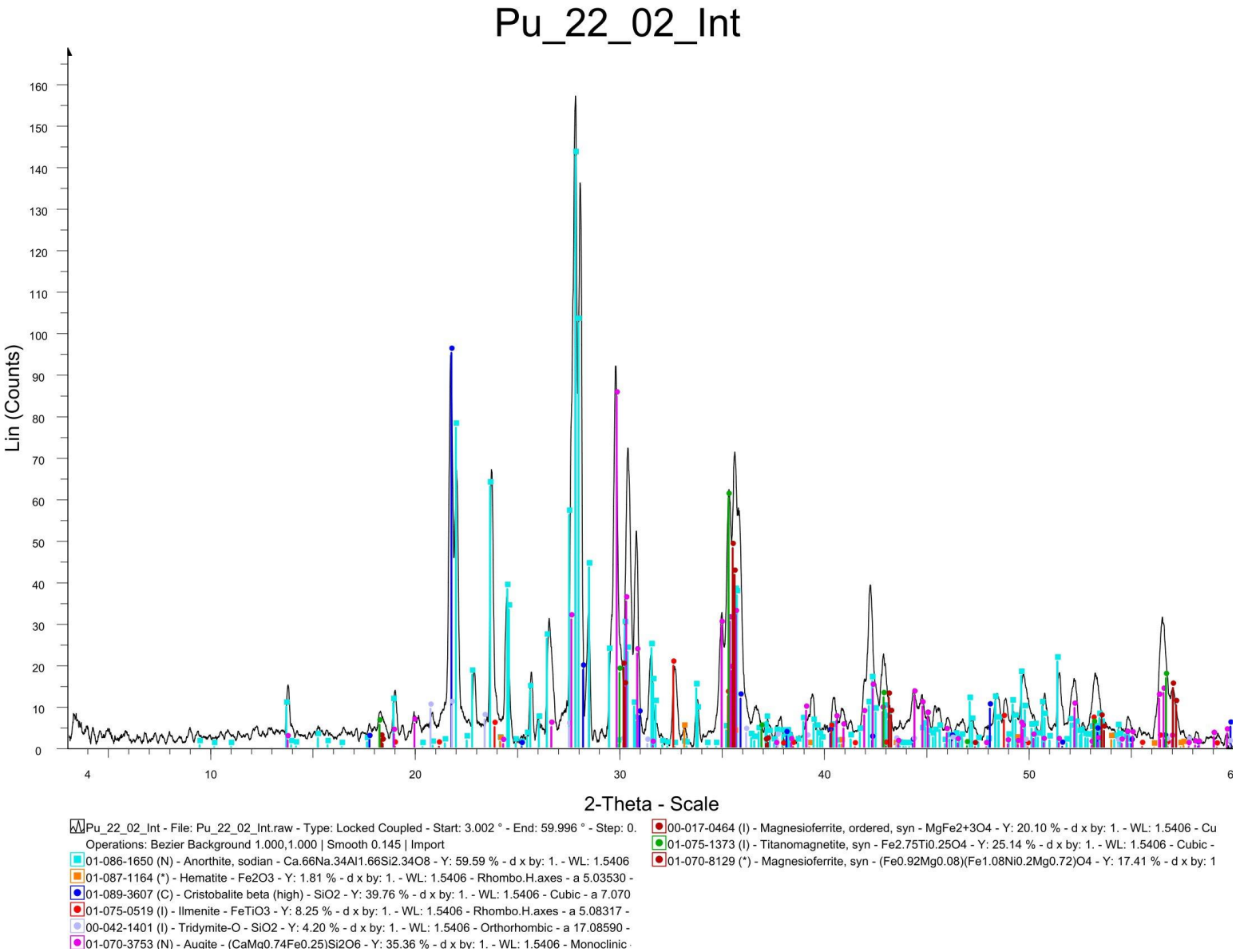

Figure 46 XRD plot for the interior of PU_22_02.

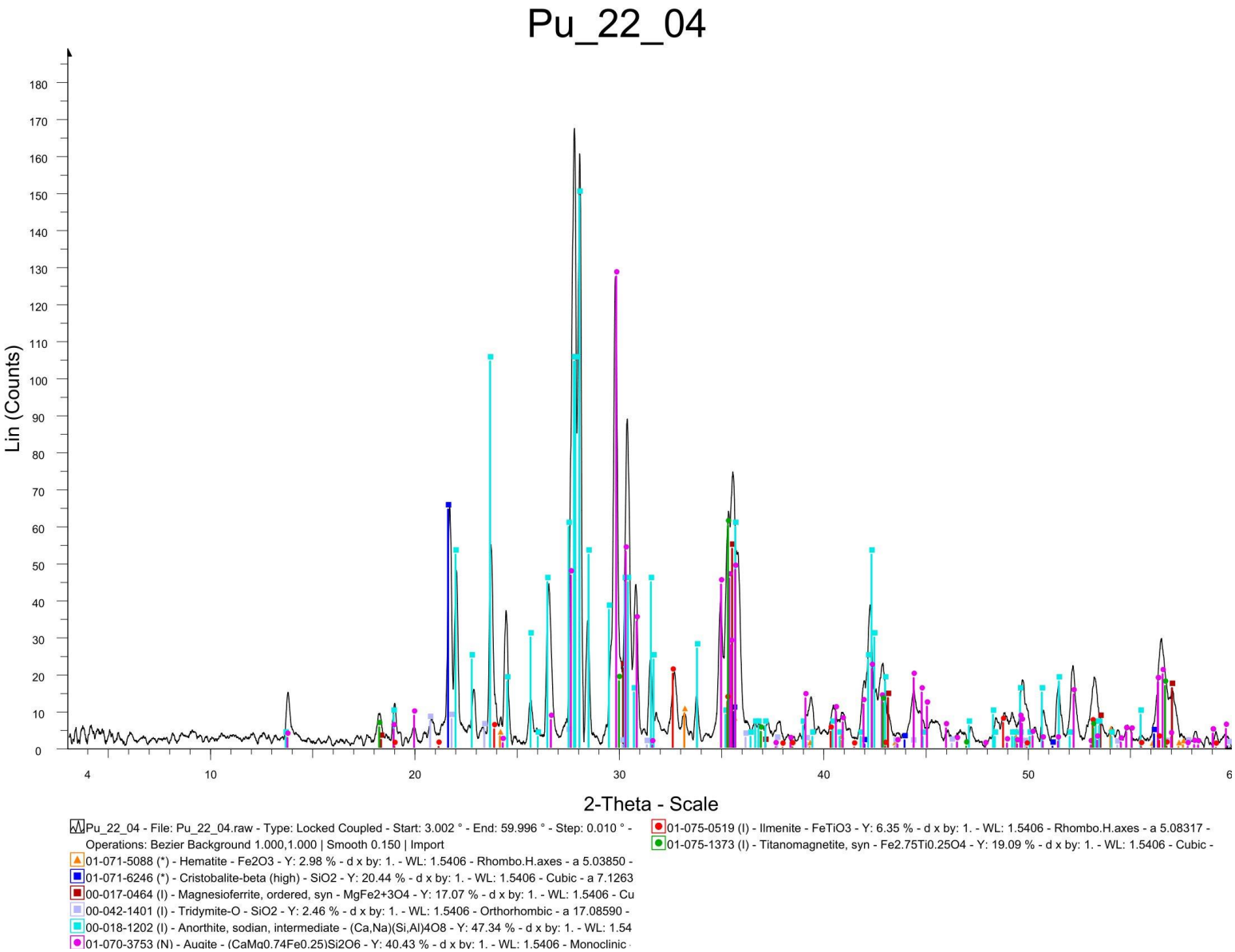

Figure 47 XRD plot for PU_22_04.

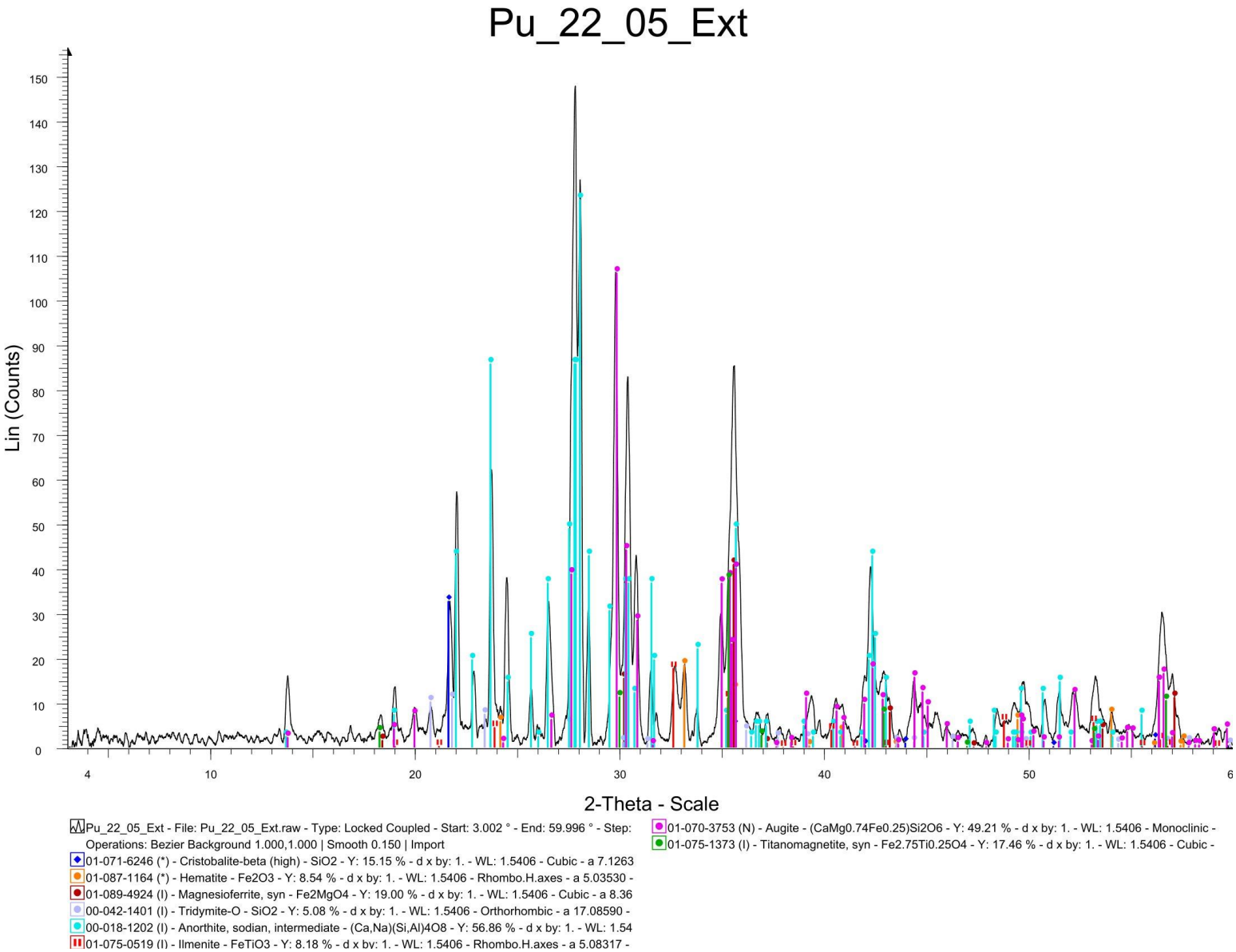

Figure 48 XRD plot for the exterior of PU_22_05.

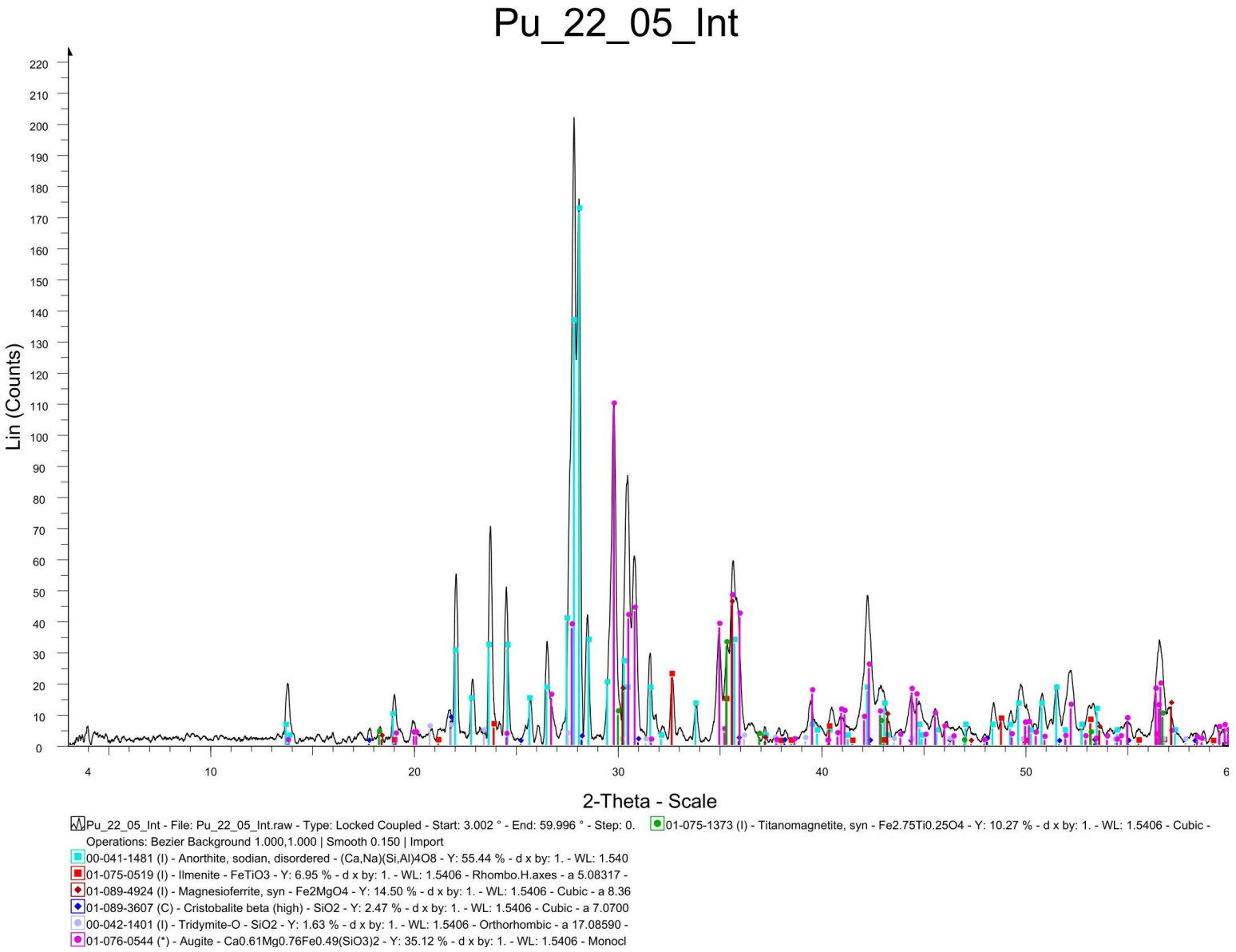

Figure 49 XRD plot for the interior of PU_22_05.

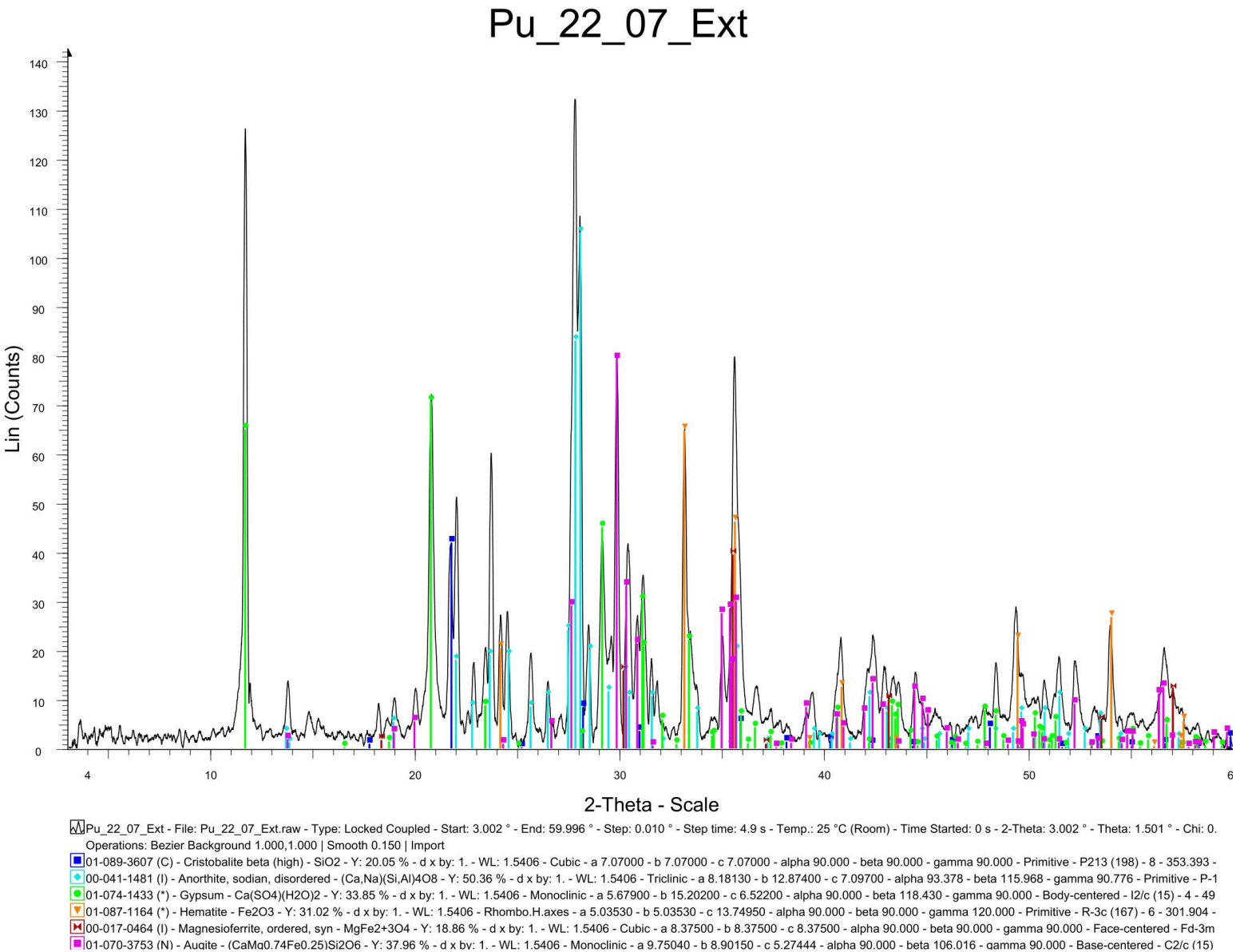

Figure 50 XRD plot for the exterior of PU_22_07.

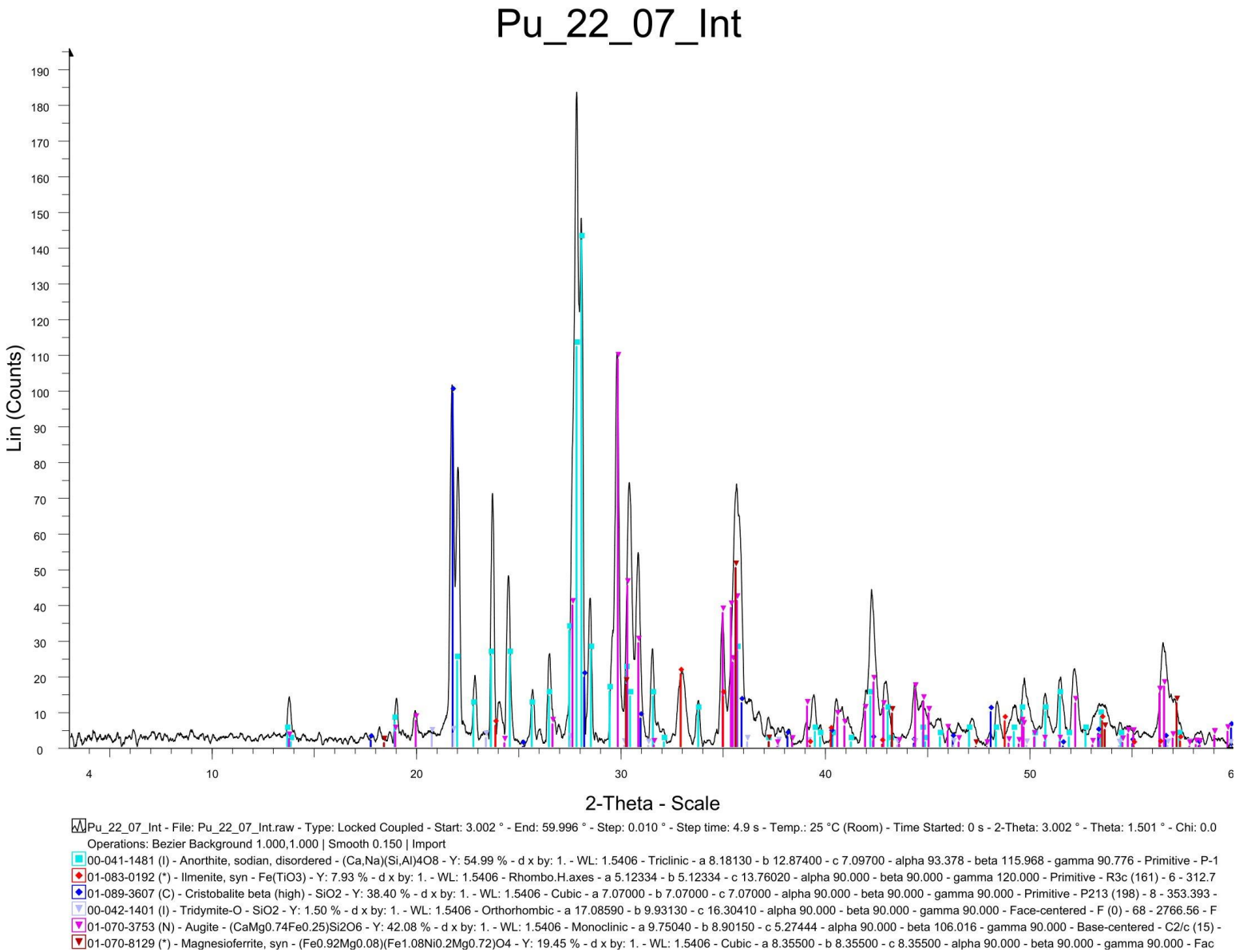

Figure 51 XRD plot for the interior of PU_22_07.

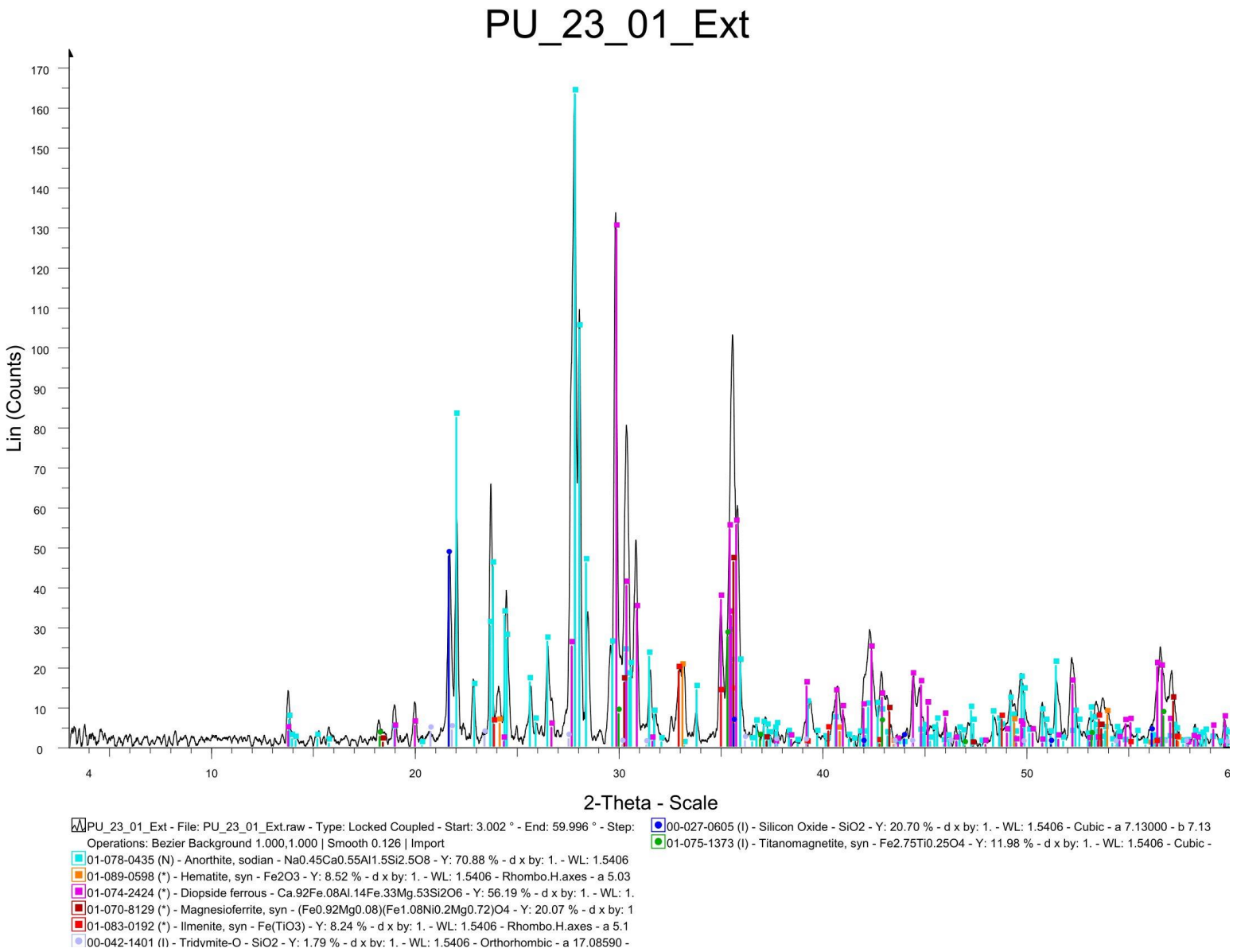

Figure 52 XRD plot for the exterior of PU_23_01.

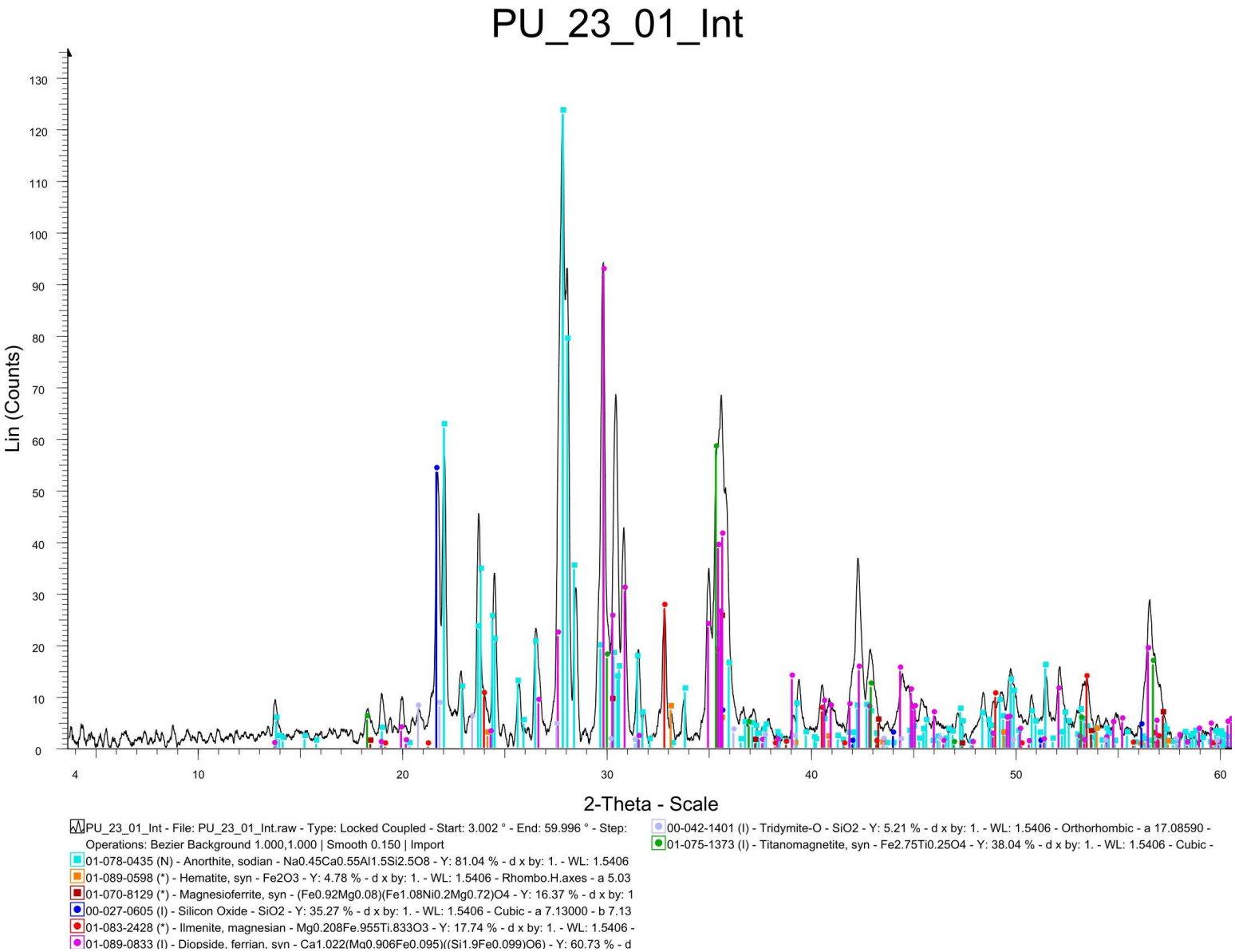

Figure 53 XRD plot for the interior of PU_23_01.

Appendix B: SEM and EDS Images

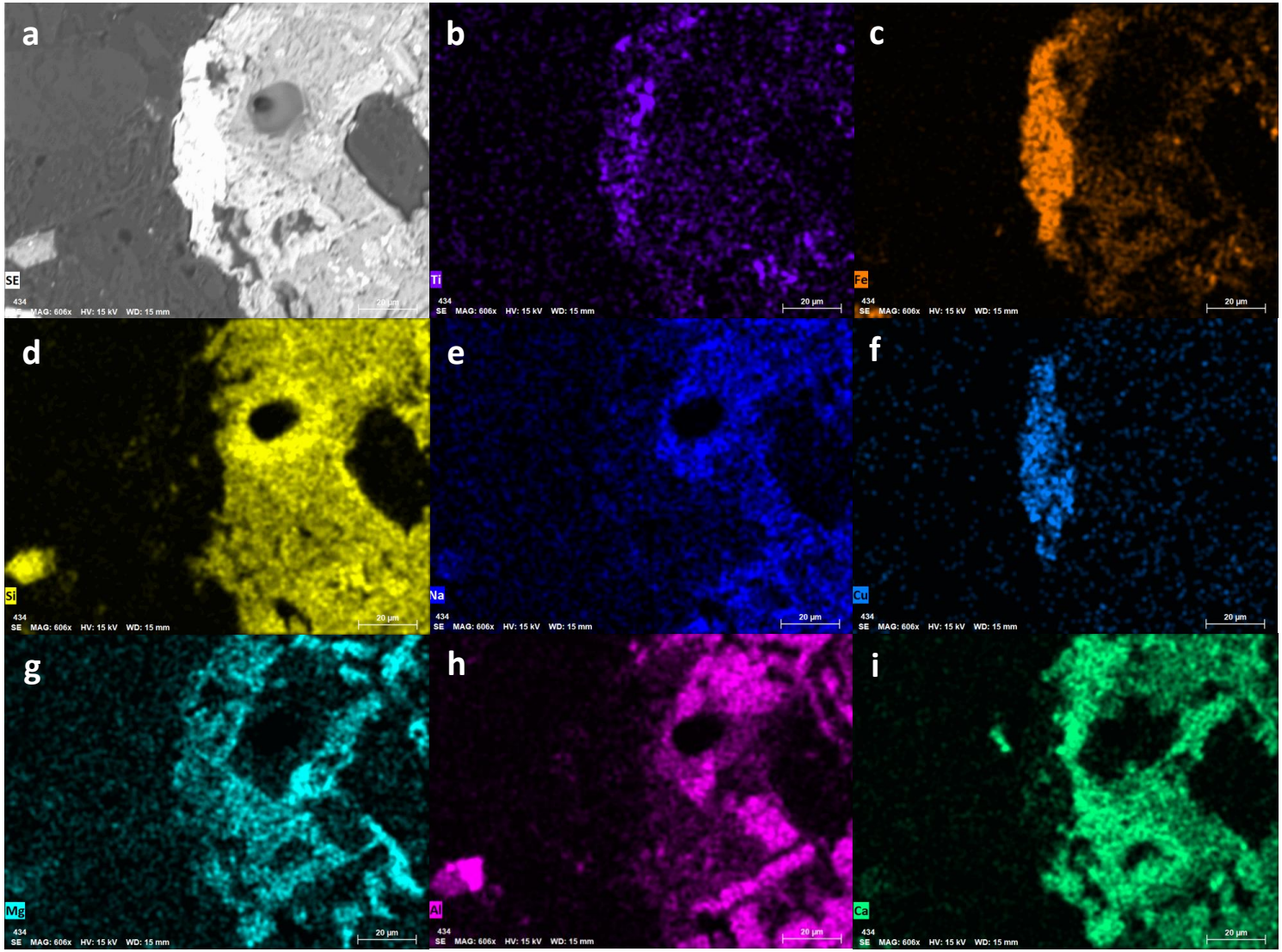

Figure 54 (a) BSE image of the cross-section of sample KK_22_02. **(b)** EDS map of titanium distribution **(c)** iron distribution, **(d)** silica distribution, **(e)** sodium distribution, **(f)** copper distribution, **(g)** magnesium distribution, **(h)** alluminum distribution, **(i)** calcium distribution.

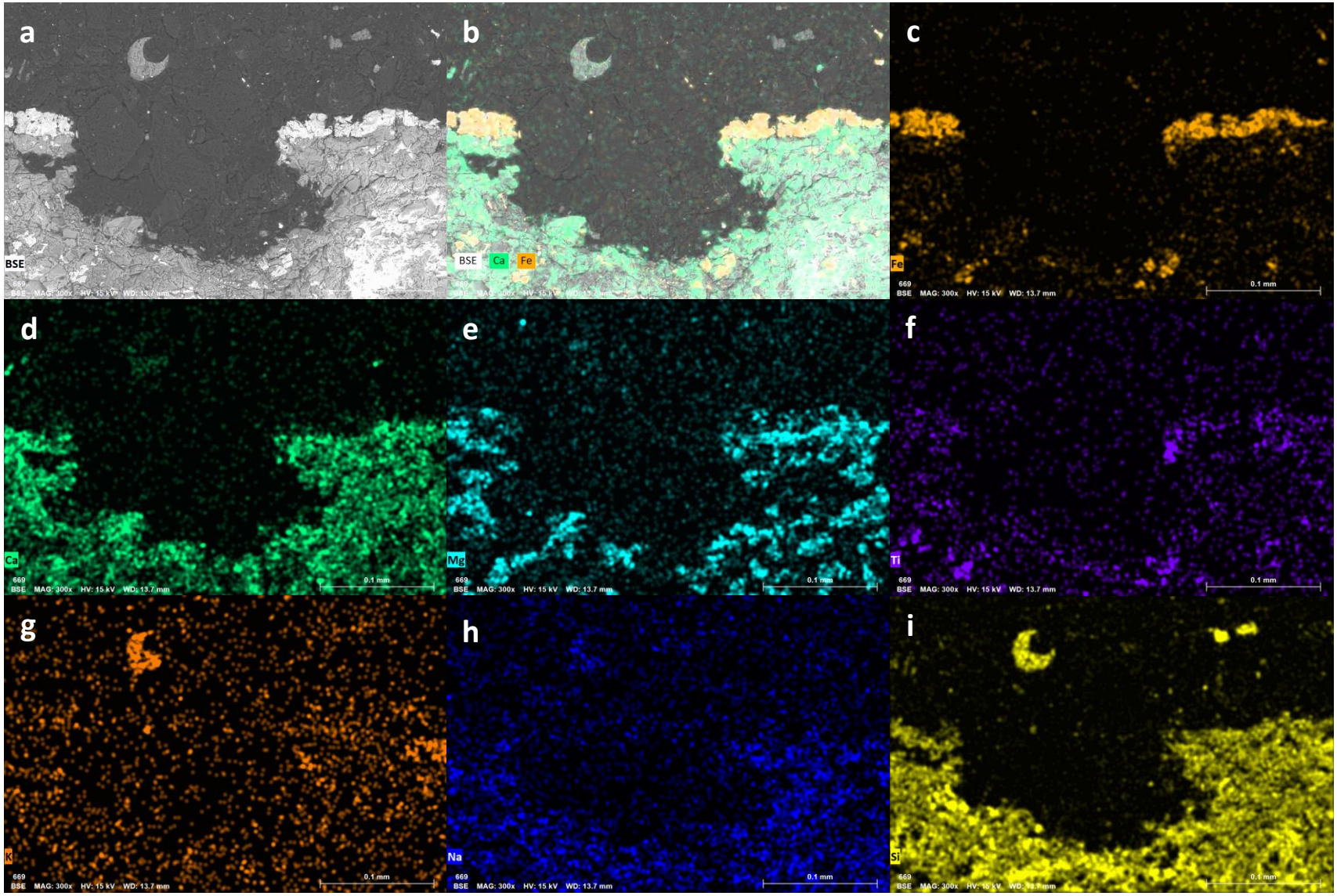

Figure 55 (a) BSE image of the cross-section of sample KK_22_02. **(b)** EDS map of calcium and iron distribution **(c)** iron distribution, **(d)** calcium distribution, **(e)** magnesium distribution, **(f)** titanium distribution, **(g)** potassium distribution, **(h)** sodium distribution, **(i)** silica distribution.

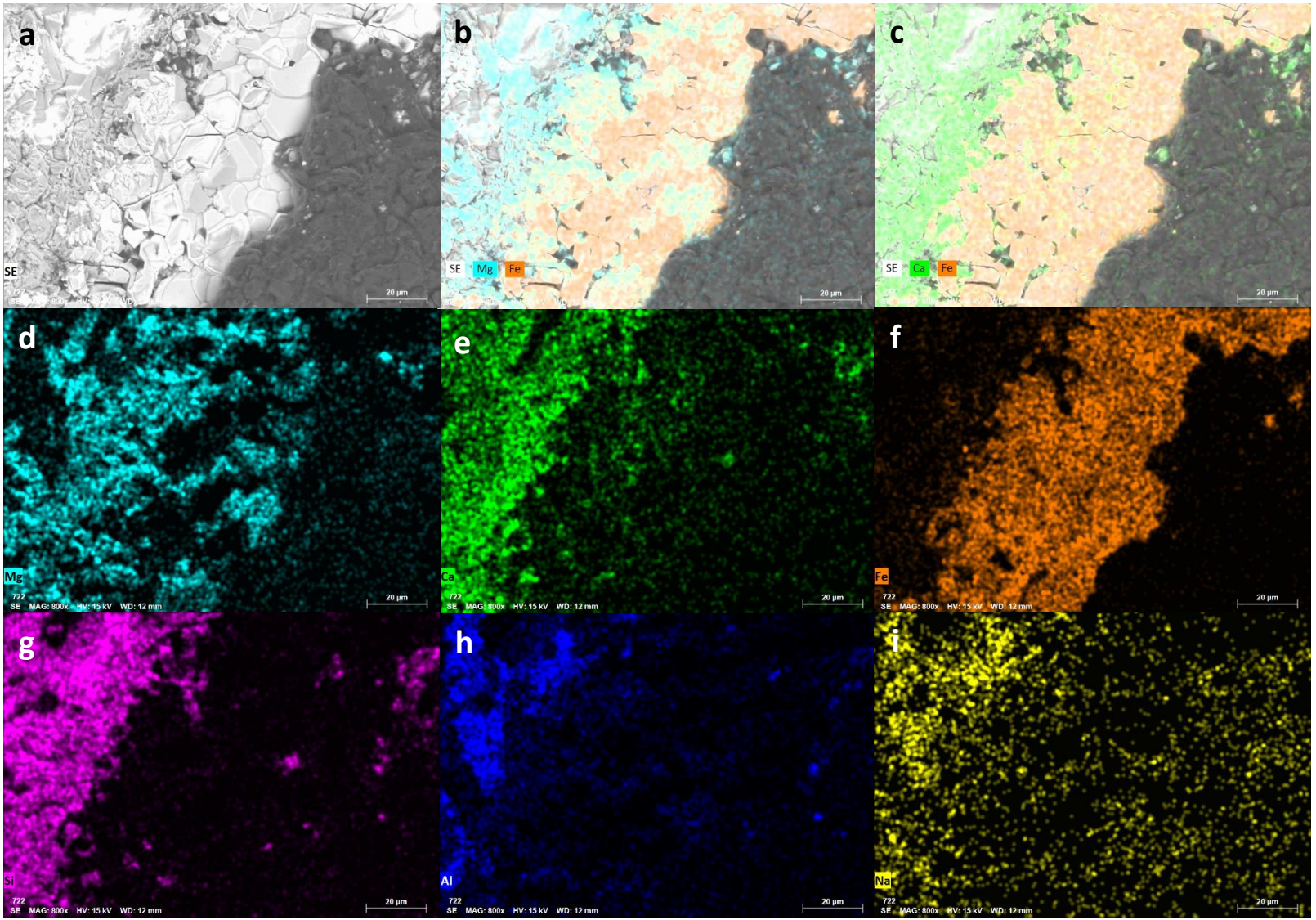

Figure 56 (a) BSE image of the cross-section of sample KK_22_08. **(b)** EDS map of magnesium and iron distribution **(c)** calcium and iron distribution, **(d)** magnesium distribution, **(e)** calcium distribution, **(f)** iron distribution, **(g)** silica distribution, **(h)** aluminum distribution, **(i)** silica distribution.

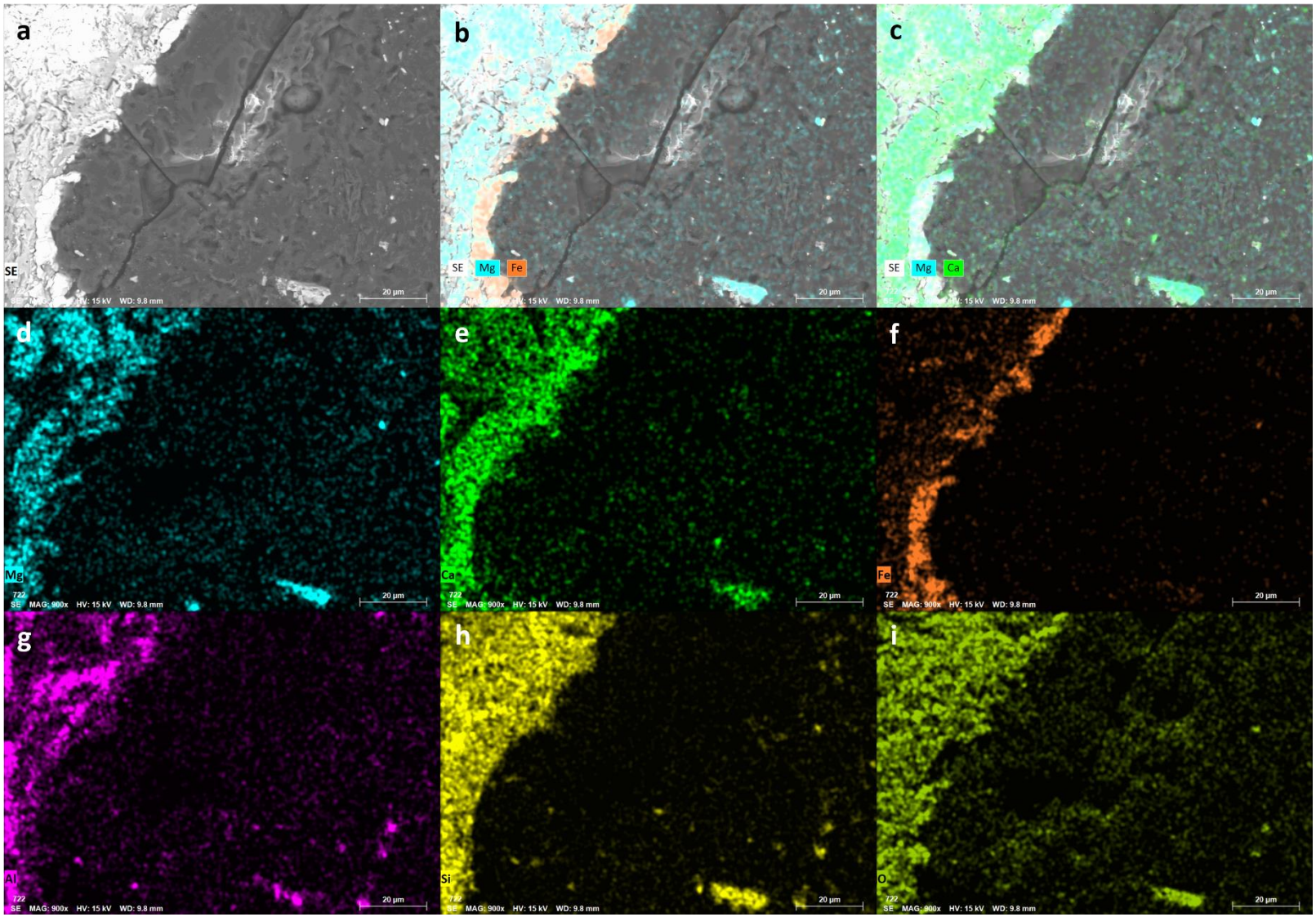

Figure 57 (a) BSE image of the cross-section of sample KK_22_10. **(b)** EDS map of magnesium and iron distribution **(c)** calcium and magnesium distribution, **(d)** magnesium distribution, **(e)** calcium distribution, **(f)** iron distribution, **(g)** aluminum distribution, **(h)** silica distribution, **(i)** oxygen distribution.

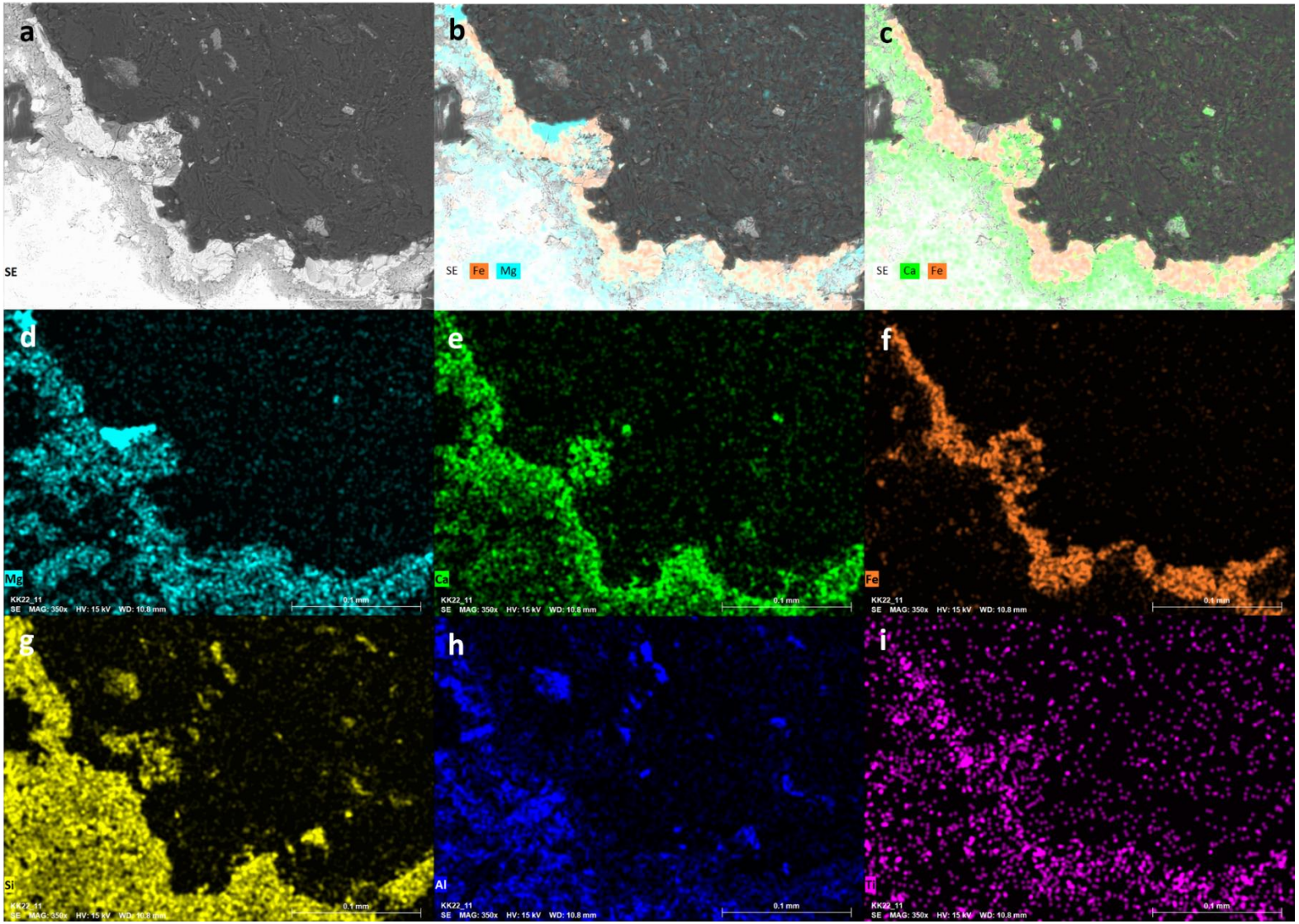

Figure 58 (a) BSE image of the cross-section of sample KK_22_11. **(b)** EDS map of magnesium and iron distribution **(c)** calcium and iron distribution, **(d)** magnesium distribution, **(e)** calcium distribution, **(f)** iron distribution, **(g)** silica distribution, **(h)** aluminum distribution, **(i)** titanium distribution.

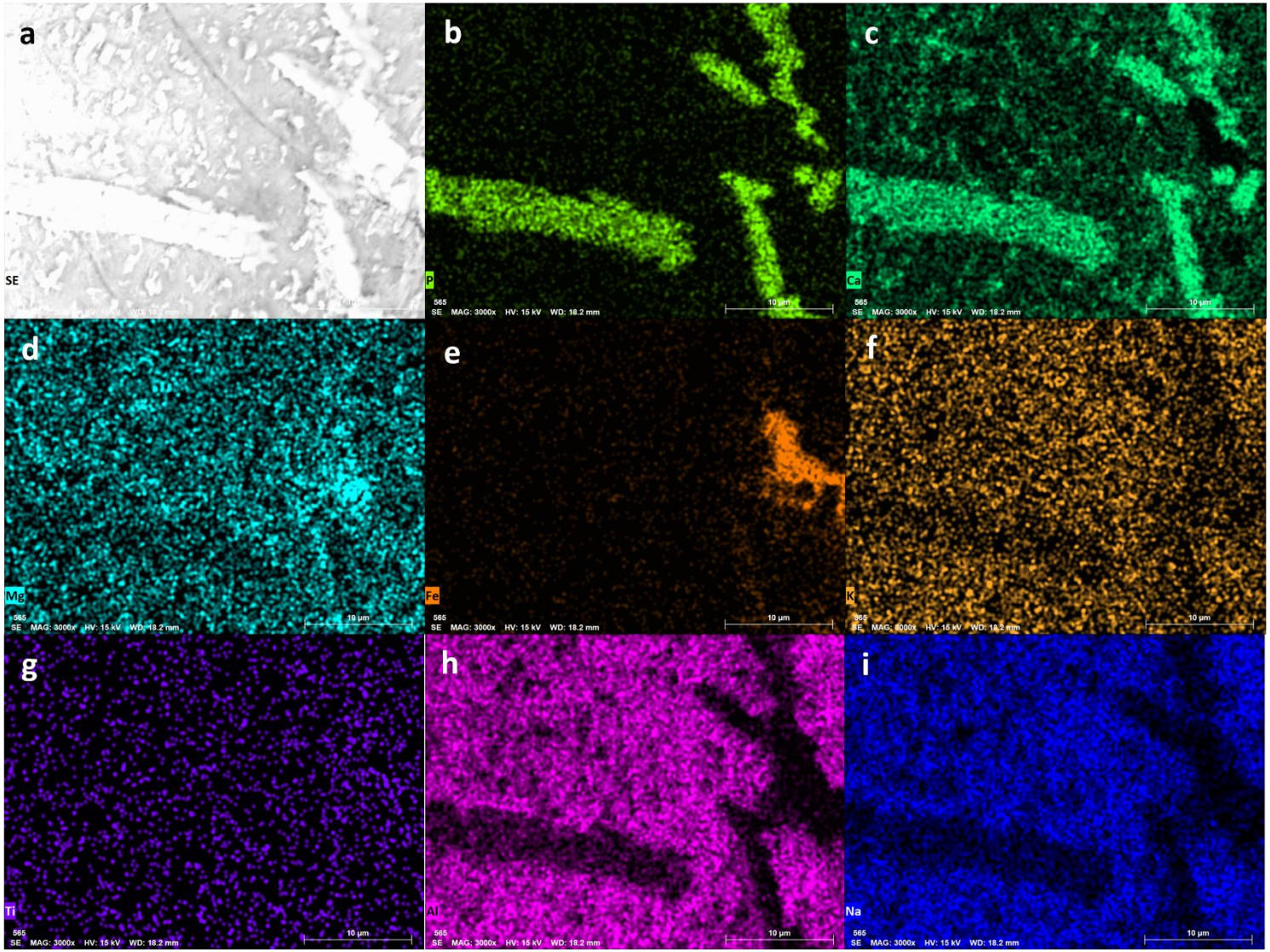

Figure 59 (a) BSE image of the cross-section of sample PU_22_02. **(b)** EDS map of phosphorus **(c)** calcium distribution, **(d)** magnesium distribution, **(e)** iron distribution, **(f)** potassium distribution, **(g)** titanium distribution, **(h)** aluminum distribution, **(i)** sodium distribution.

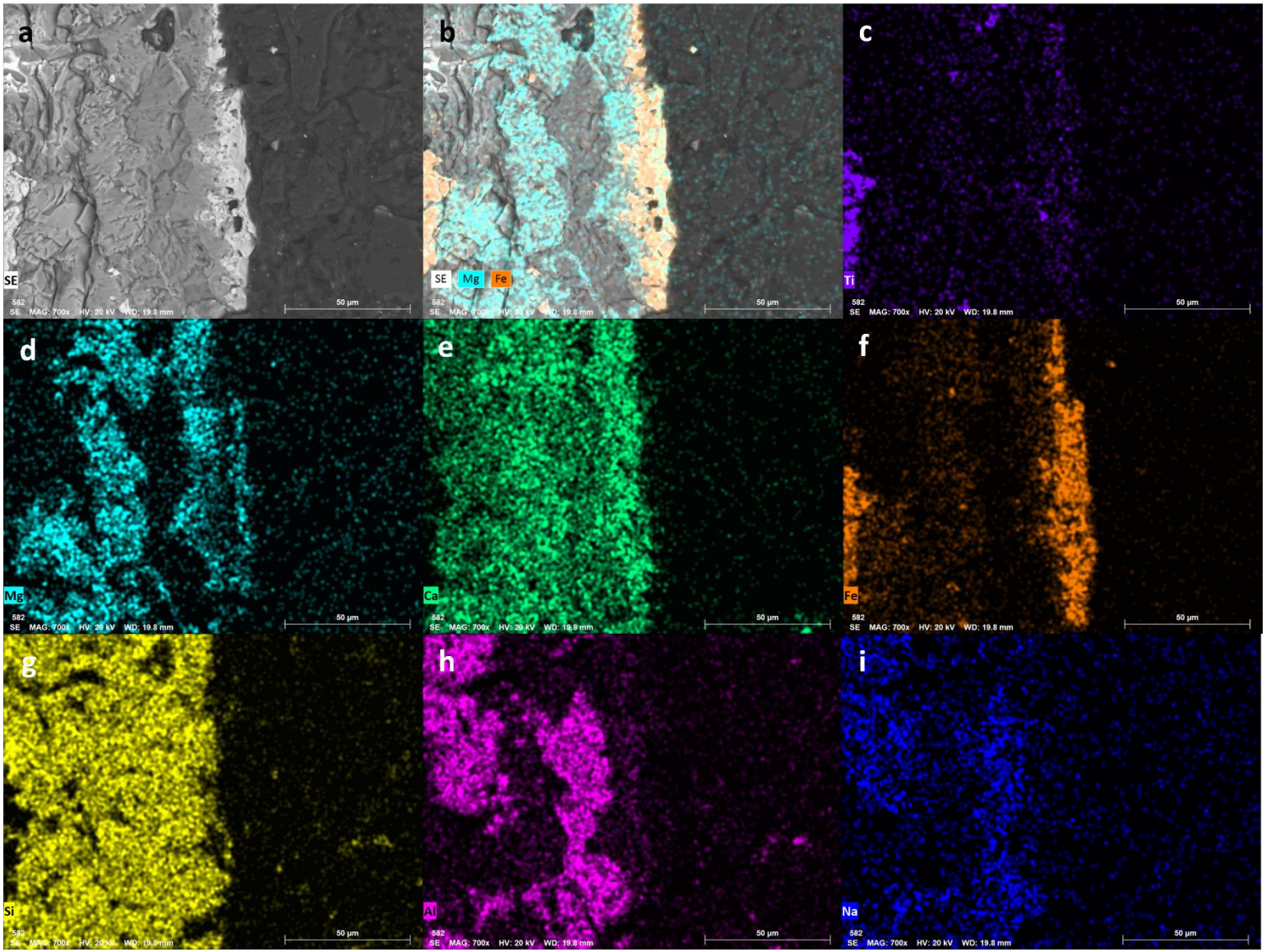

Figure 60 (a) BSE image of the cross-section of sample PU_22_05. **(b)** EDS map of magnesium and iron **(c)** titanium distribution, **(d)** magnesium distribution, **(e)** calcium distribution, **(f)** iron distribution, **(g)** silica distribution, **(h)** aluminum distribution, **(i)** sodium distribution.

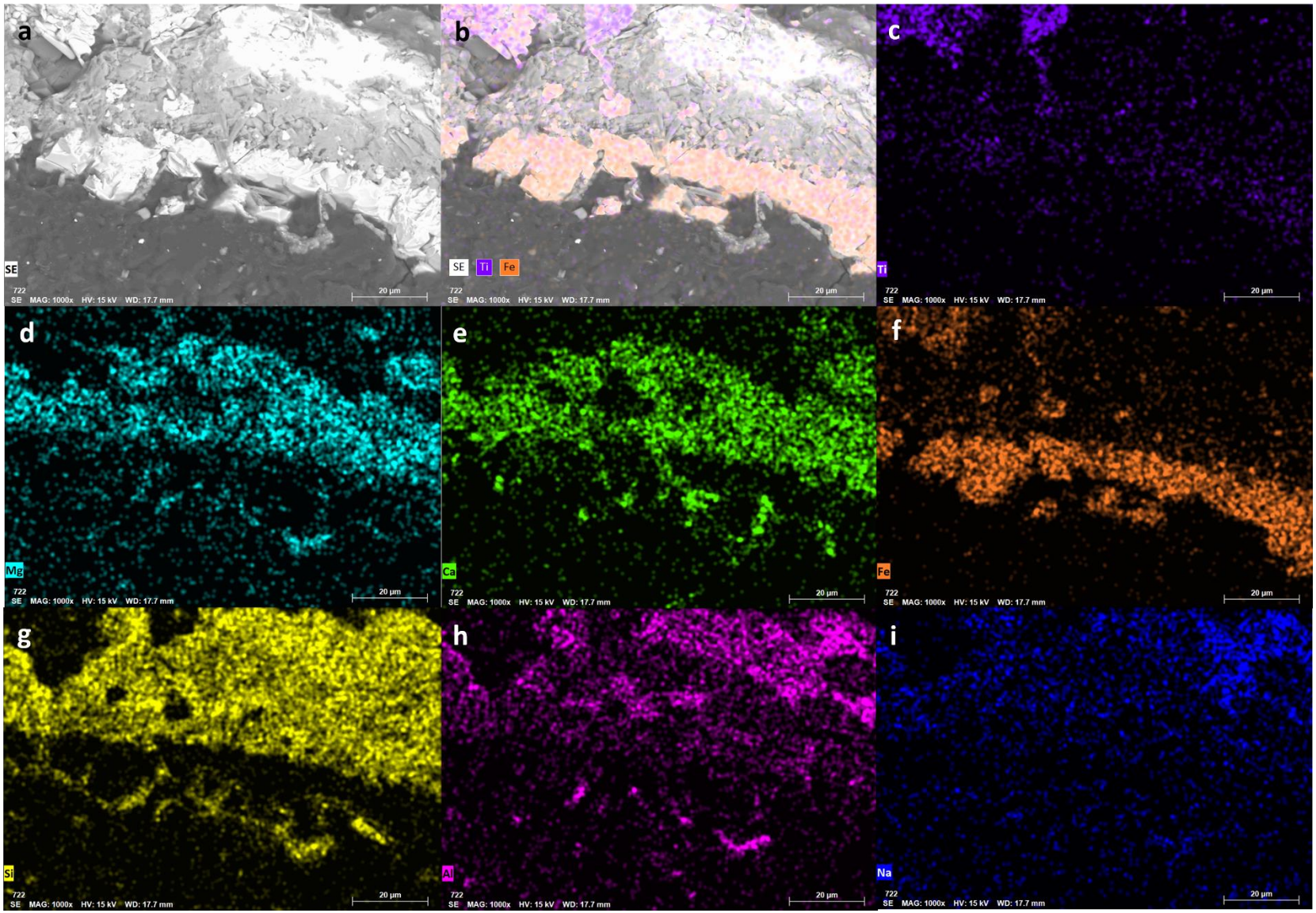

Figure 61 (a) BSE image of the cross-section of sample PU_22_05. **(b)** EDS map of titanium and iron **(c)** titanium distribution, **(d)** magnesium distribution, **(e)** calcium distribution, **(f)** iron distribution, **(g)** silica distribution, **(h)** aluminum distribution, **(i)** sodium distribution.

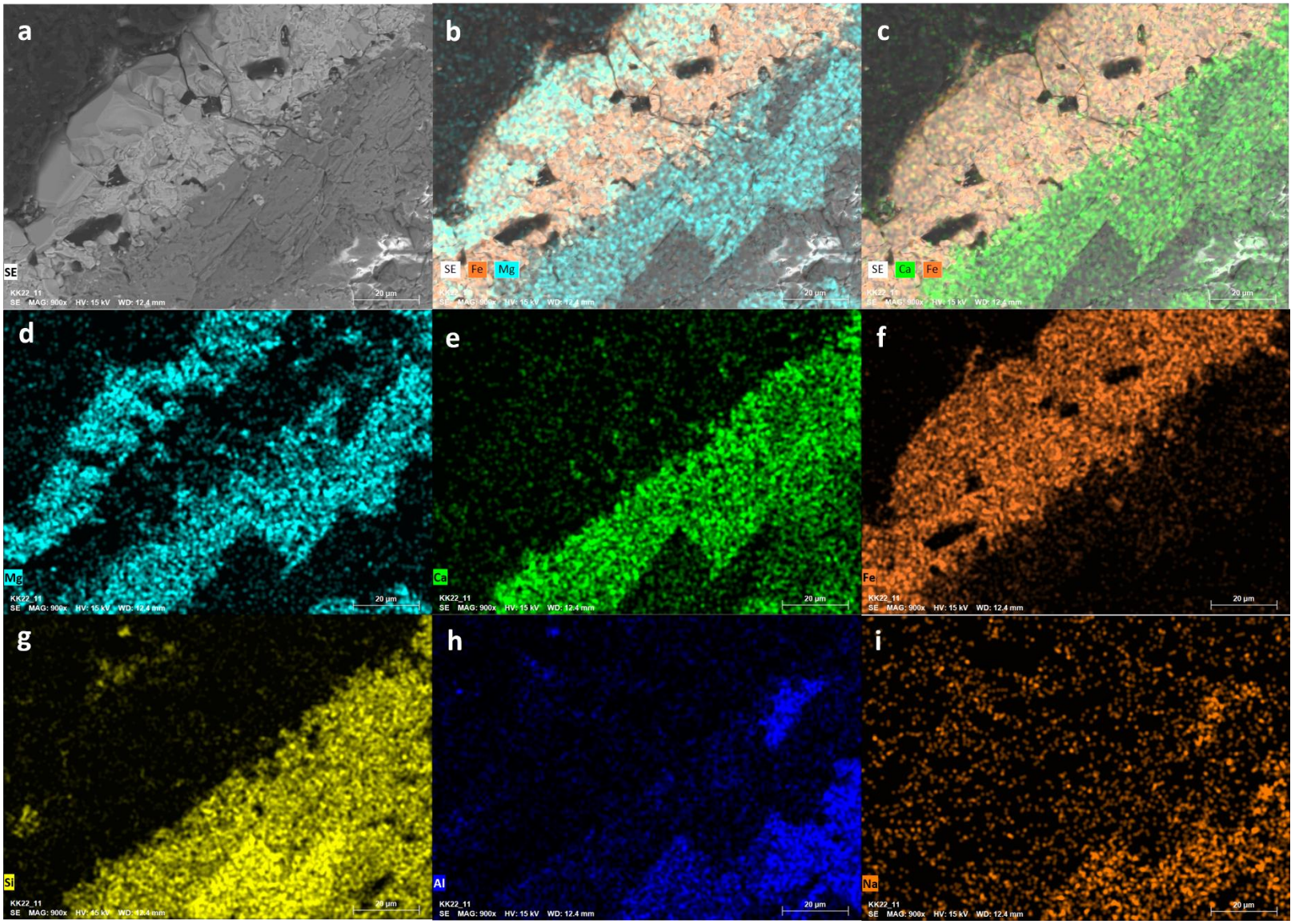

Figure 62 (a) BSE image of the cross-section of sample PU_23_01. **(b)** EDS map of magnesium and iron distribution **(c)** calcium and iron distribution, **(d)** magnesium distribution, **(e)** calcium distribution, **(f)** iron distribution, **(g)** silica distribution, **(h)** aluminum distribution, **(i)**

Appendix C: Field Photos

Figure 63 Photographs taken at different caves from the Kipuka Kanohina flow. **(a)** photo in Nā Nalu Cave, featuring Lindsay, **(b)** drip features and metallic coatings in Black Ball Cave, **(c)** entrance to an unnamed lava tube on private property, **(d)** drip features, **(e)** Lindsay and Dylan in Black Ball Cave, **(f)** Lindsay, Dylan, and Jorge at the main KK flow, **(g)** drip features. Photos courtesy of: Peter Bosted, Dylan Childs.

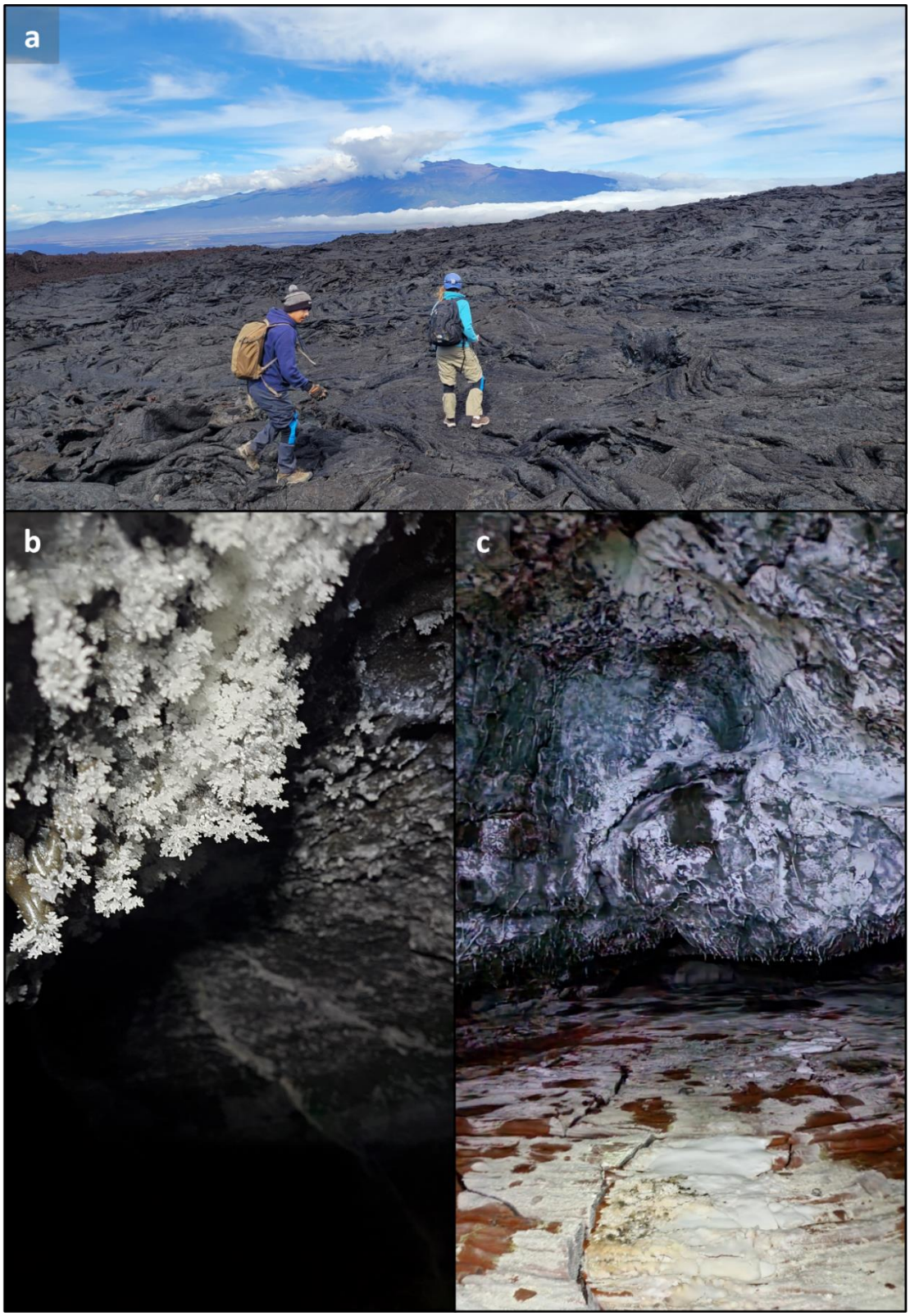

Figure 64 Photos taken at the 1843 Mauna Loa flow. **(a)** Image of Lindsay and Jorge hiking on the northern flank of Mauna Loa, overlooking Mauna Kea, **(b)** image of sulfate crystals in Crystal Cave, **(c)** image of Orange Apron cave

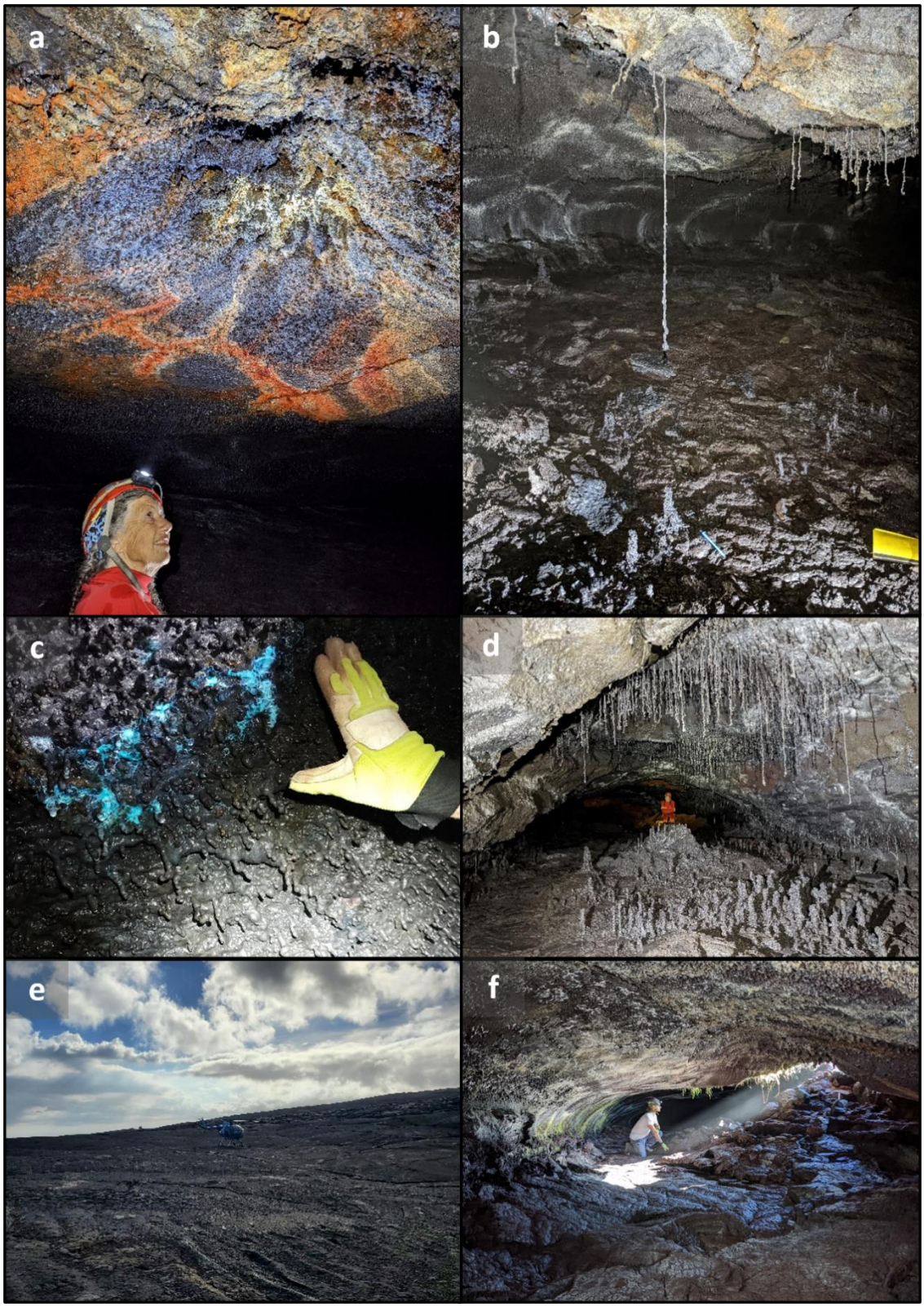

Figure 65 Photographs taken at Ana Polu Cave from the Puʻuʻōʻō flow. **(a)** Ann Bosted and ceiling of lava tube, **(b)** large, >1m long drip feature, "lavacicle", **(c)** blue aqueous solution permeating from ceiling, **(d)** Ann Bosted pictured in room featuring many lava stalactites and stalagmites, **(e)** landing site for our helicopter in the field of the lava flow near the cave, **(f)** Dylan Childs inside the cave entrance. Photo credit: Peter Bosted and Jorge Acosta.